

Development of Ultrafast Raman Lasers

By

Aravindan Madhava Warriar

A thesis submitted to Macquarie University

for the degree of

Doctor of Philosophy

Department of Physics & Astronomy

NOVEMBER 2015

Supervised by

Assoc. Prof. David J. Spence

Assoc. Prof. Helen M. Pask

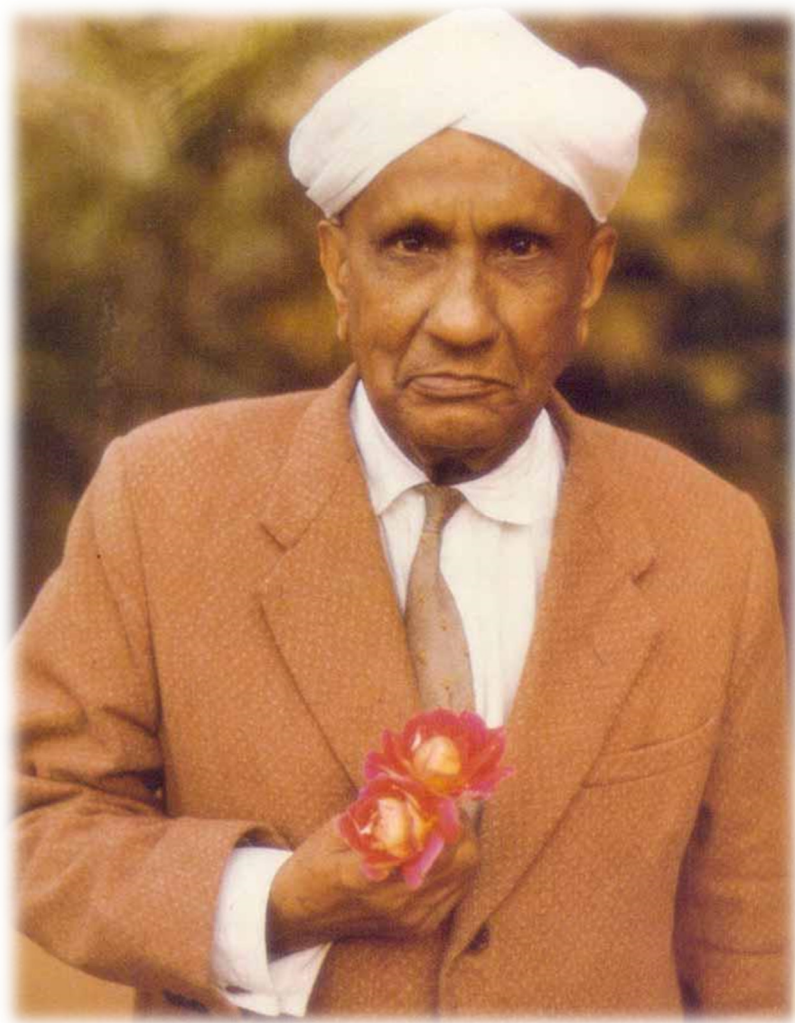


MACQUARIE
University

Declaration

This thesis is submitted in the fulfilment of the requirements of the degree of Doctor of Philosophy at Macquarie University and has not been submitted for a higher degree at any other university or institution. I certify that to the best of my knowledge, all sources used in the preparation of this thesis have been acknowledged in the customary manner.

Aravindan Madhava Warriar



Chandrasekhara Venkata Raman (1888-1970)

"I study science not because anything is going to happen to me but because I feel it is a kind of worship of this great Goddess, Nature of which we are a part. That has been my inspiration as a man of science."

Abstract

Ultrafast lasers have made a tremendous impact on our lives, impacting a spectrum of applications like communication, medicine, defence, material processing, and security. It took many years after the inception of the laser to reach the ultrafast domain of picoseconds and femtoseconds. The fact that different applications require different wavelengths resulted in the development of lasers with many different wavelengths along with tunable lasers. Dye lasers were one of the first to generate tunable radiation, but soon the Ti:sapphire laser emerged as an unrivalled laser source. Semiconductor technology has now resulted in the demonstration of tunable VECSEL laser systems that perhaps challenge Ti:sapphire in versatility.

Lasers in the visible region are most often built using nonlinear conversion techniques like second harmonic generation and sum frequency mixing with infrared lasers. With the increase of applications over time, there are many that are constrained by the spectral and temporal characteristics of available commercial lasers. For example the biophotonics area, with applications in two-photon microscopy and molecular uncaging faces challenges due to the lack of inexpensive laser sources in the visible range. This highlights the importance of developing new laser sources which can access different wavelengths and extend the wavelength reach of existing laser sources.

This thesis explores this possibility of wavelength extension and pulse compression by the use of Raman laser technology, by employing the synchronous pumping scheme using diamond and lithium niobate crystals. We report Raman lasers which extend the wavelength reach of a continuous-wave mode-locked picosecond laser. Diamond and lithium niobate have their own unique properties resulting in three different laser systems. The diamond makes an efficient first Stokes and Second Stokes laser with a simple cavity design and pulse compression. The lithium niobate crystal resulted in a multiwavelength ultrafast laser generating four wavelengths which were switchable and controllable. We also report a lithium niobate ultrafast Raman laser that generated terahertz waves, using Raman shifting to produce a cavity-enhanced Stokes field to drive THz output using polariton scattering.

Acknowledgement

First and foremost, I would like to express my deepest feelings of gratitude to my principal supervisor Associate Professor David J. Spence without whose support and encouragement this thesis would not have been a success. I really appreciate and acknowledge his expertise in explaining various intriguing concepts with clarity, throughout the PhD programme. He was always available for me with a smiling face and played the major role of guiding a novice like me in the field of Raman lasers. I find myself to be fortunate to be able to work with Dave. Thank you Dave.

Dr. Jipeng Lin, my co-supervisor, is yet another person who played an important role in my PhD programme and I owe a great deal my knowledge in the field of laser development to him. I greatly value the tutelage and constant support that Jipeng provided throughout. He was kind enough to teach me various nuances of laser engineering right from the beginning. For an expert, it is a great task to allow a beginner to work along with him at the same time maintaining a slow pace of work so that the beginner gets chance to understand what is being done. The patience that Jipeng displayed in in this regard, I should say, is unparalleled. The efficient guidance he provided in the beginning year of my PhD gave me enough confidence and equipped me to work myself towards the end of the programme. I cherish the time I spent with him in the lab which has made me eligible for this degree. I find no words to express gratitude to you, dear Jipeng.

I was fortunate enough to have Associate Professor Helen M. Pask as my associate supervisor. I would like to express my gratitude to Helen for her constant support. She displays a pleasing personality which had always inspired me. Meetings with her had always been extremely fruitful with newer ideas about carrying out the experiments and better ways of presenting the results. Thank you, Helen.

I was fortunate to get such supportive supervisors who were always with me, helping me to tread the path of research with ease. Other people who were associated with me at different points of time are Professor David J. Coutts, Assistant Professor Rich P. Mildren, Dr. Andrew J. Lee. With a pretty long experience, David had been a great support during regular meetings in the initial days. Rich, the diamond man, had always been a friendly person and helpful with the diamond Raman laser that we developed in the beginning. Andrew had been a great help while I was doing the lithium niobate and terahertz experiments. He was always available to clarify many the doubts and was easily accessible. I would like to take this opportunity to thank you all, Dave, Rich, Andrew.

While writing an acknowledgement, one cannot but mention the wonderful friends and colleagues who makes you feel welcomed and comfortable. I would like Suresh and Rajesh who helped me quite a lot in the begging days to settle in a new country and get acquainted with the way of life. Sandhya, Hadiya, Sowmya, Ali, Zak, Chris, Van, Barbara, Annemarie, Anna, Tiago, Yameng, Ran, to name a few, whom I would like to thank at this juncture.

I would take this opportunity to thank the administrative team of Department of Physics and Astronomy as well as the HDR in providing a comfortable platform for the researchers. I also register my gratitude to the university in providing the Scholarship for the PhD programme.

I think...this is a never-ending list.... Gratitude to all!

Statement of contribution

The entire work presented in this thesis as well as in the form of two peer reviewed publications and a patent application, is the work of the author of this thesis. The lasers reported in this thesis have been built and characterised by the author. Training on aspects of laser engineering along with advice on experimental techniques to be followed were provided by the postdoc and staff (whose names appear in the publications) at Department of Physics and Astronomy, Macquarie University. They also helped the author in analysing the observed data as well as in proper interpretation of the same. The author was helped in the formulation and structuring of the thesis by the principal supervisor.

Table of Contents

Declaration	iii
Abstract	vii
Acknowledgement	ix
Statement of contribution	xi
Table of contents	xiii
1. SOLID-STATE ULTRAFast RAMAN LASERS.....	1
1.1 Background and overview	1
1.2 Wavelength versatile ultrafast laser sources	2
1.3 Introduction to Raman lasers	6
1.4 Transient and steady-state SRS regimes	10
1.4.1 Theory of transient SRS	11
1.5 Raman Laser design considerations	14
1.5.1 Raman laser crystals	14
1.5.2 Raman laser cavity designs.....	16
1.6 Synchronously pumped Raman laser approach to ultrashort pulses	19
1.7 Chapter Summary	22
1.8 References for Chapter 1	24
2. SYNCHRONOUSLY PUMPED PICOSECOND DIAMOND RAMAN LASER.....	31
2.1 Structure of diamond and accessing maximum Raman gain	31

2.2	Diamond Raman lasers	33
2.3	Mode-locked picosecond diamond Raman laser	34
2.3.1	Experimental setup	35
2.3.2	The ring cavity design	37
2.3.3	Efficient 1240 nm Stokes generation from diamond	37
2.3.4	Pulse compression mechanism in synchronously pumped Raman lasers	42
2.3.5	Second-Stokes generation by parametric coupling of SRS components	46
2.3.6	Backwards generation of first-Stokes (1240 nm)	55
2.3.7	Isolating forward and backward generated Stokes fields	58
2.4	Chapter Summary	68
2.5	References for Chapter 2	69
3.	MULTIWAVELENGTH ULTRAFAST LiNbO₃ RAMAN LASER	71
3.1	Lithium niobate crystal and tunability of Raman medium	71
3.2	Tunable wavelength generation from lithium niobate	78
3.3	Experimental setup	82
3.4	Multiwavelength accessibility of our system	83
3.5	Spectrally controlled laser based on a single vibrational mode	88
3.5.1	Controlled cascaded multiple wavelength generation	96
3.6	Chapter Summary	98

3.7	References for Chapter 3	100
4.	TERAHERTZ WAVE GENERATION FROM AN ULTRAFAST RAMAN LASER	103
4.1	Terahertz waves	103
4.2	Parametric scattering of terahertz waves by polaritons	106
4.3	Theory of Terahertz Parametric Generation (TPG)	109
4.4	Terahertz Parametric Oscillators and extraction of terahertz waves	111
4.5	Terahertz generation by optical rectification	114
4.6	Terahertz generation from quasi-phase matched crystals	115
4.7	Terahertz wave generation in enhancement cavities	116
4.8	Terahertz wave generation from ultrafast LiNbO ₃ Raman laser	119
4.9	Measuring the generated terahertz waves	123
4.10	Laser control: Single terahertz frequency generation	129
4.11	Chapter Summary	132
4.12	References for Chapter 4	133
5	CONCLUSION AND FUTURE WORK	139
	References for Chapter 5	145
PUBLICATIONS	147
	Publication 1	149
	Publication 2	159
LIST OF FIGURES	165

1

Solid-state ultrafast Raman lasers

1.1 Background and overview

Ultrashort light pulses produced by man form the smallest light sparks in the universe. Lasers have come a long way since the field of ultrafast physics had its inception soon after the invention of lasers in 1960 with the first picosecond laser pulse generation from a neodymium doped glass laser in 1963 [1]. Since then the arena of ultrafast phenomenon has exploded with research possibilities. Our perception of the universe and its numerous phenomena is limited by the temporal resolution of the instruments available to us. The need and importance of ultrafast lasers comes into play in such a context. The fastest electronics can only measure into the picosecond regime. The ever increasing applications to understand Nature in Her minutest details have led to the development of ultrafast laser sources which

brought down the temporal resolution of measurements further into the sub-femtosecond regime, where we can begin to observe even molecular vibrations.

Different applications require different wavelength lasers, driving the development and innovation of ultrafast laser sources. The short time duration of ultrafast lasers has led to fast temporal characterization of a variety of physical and chemical phenomena. Generation of stabilized attosecond pulses has become a topic of great interest in recent years. One attosecond forms 10^{-18} of a second, and attosecond pulses have been successfully applied in photoelectron and photo-ion spectroscopy and attosecond transient absorption spectroscopy to study electron dynamics in matter [2].

Ultrashort pulses also have enhanced peak power, which finds application in a variety of fields such as material processing, accurate radar pulse measurements, particle accelerators and nuclear fusion experiments. Fabrication of nanostructures with micrometer resolution on solid materials utilises this high peak power (petawatts) [3]. Other areas of hot topics in research are high harmonic generation [4, 5] and creation of plasmas (gigawatts) [6] leading to realisation soft-X-ray lasers from plasma emissions (megawatts) [7]. The high peak power also allows nonlinear conversion which brings accessibility to a range of new wavelengths.

Ultrafast lasers have made their way into the medical field along with many others. Lasers have been used in eye surgery or corneal sculpting where the laser is employed to reshape the surface of the eye [8]. A scan of all the varied applications and developments that rely on ultrafast laser sources would lead us to a conclusion that one of the key areas of research and development in the field of ultrafast lasers is to enable the existing lasers to access new wavelengths and obtain shorter or compressed pulses. This forms the motivation for the research work presented in this thesis.

1.2 Wavelength versatile ultrafast laser sources

Ultrafast lasers have been finding application in a wide range of fields as diverse as communications, high energy physics, nuclear fission reactors, defence and

biophotonics etc. Some of these applications are constrained by the poor availability or high cost of necessary laser sources with required characteristics. Two-photon microscopy [9], that studies diseases at molecular and cellular level, and molecular uncaging [10], which has the potential to activate highly-specific disease-fighting drugs with high localisation, are applications in the area of biophotonics where the science is limited by the constraints of available ultrashort technology. This is due to the high cost of achieving the required wavelengths. Different applications have different wavelength requirements and it is impractical to have individual lasers sources for each application. This highlights the importance of wavelength versatile lasers whose output wavelength are either multiwavelength or tunable over a wide range about the central frequency.

A variety of spectroscopic applications like remote sensing, coherent laser radar systems etc. require narrowband continuously tunable radiation. Johnson *et. al.* developed the first tunable laser based on Ni:MgF₂ laser in 1963 at the Bell laboratories [11]. Titanium sapphire lasers are one of the most flexible tunable lasers developed and form part of most optics laboratories. The first laser developed by Maiman, used synthetically grown ruby or sapphire doped with small amount of chromium. The same ruby or sapphire crystal was used with a different impurity doping of titanium by P.F Moulton [12] when he created the first widely tunable laser. Ti:Sapphire lasers were mode-locked to under 100 fs in 1991 by Spence *et. al.* [13] and due to their bandwidth spanning from 650 nm to 1100 nm, can support pulses as short as 5.5 fs [14]. Sapphire being transparent from the ultraviolet to the infrared, forms an ideal laser host. It has advantageous properties like being nonhygroscopic and a hardness comparable to diamond (it reads 9 on the Mohs scale compared to 10 of diamond) which again makes it a durable material for laser development. Excellent properties like high thermal conductivity, mechanical stability and high optical quality have propelled Ti:Sapphire to be the leading tunable laser sources being used in laboratories today.

Another common family of tunable lasers are the organic dye lasers which are use some organic dye (eg. Rhodamine 6G) dissolved in a liquid solvent host [15]. Rhodamine 6G lasers have a tunability range from 570 nm to 610 nm with many other dye lasers with spectral coverage spanning from the infrared to the ultraviolet. However these liquid based lasers are inconvenient and out of fashion.

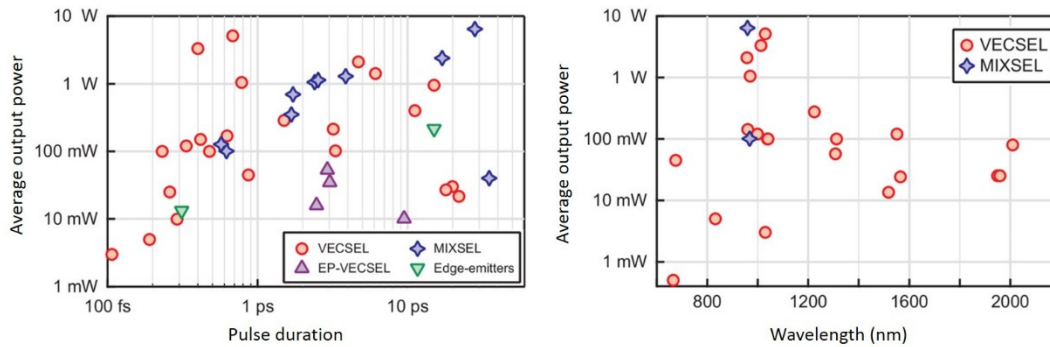


Fig 1.1 Left: Review of data of average output powers versus pulse duration of optically pumped semiconductor lasers including VECSELs. Right: Reported average output power versus wavelength for mode-locked semiconductor disk lasers, taken from [17]. EP-VECSEL: Electrically pumped VECSEL. MIXSEL: mode-locked integrated external-cavity surface-emitting laser.

The semiconductor medium provides a flexible choice of wavelength via bandgap engineering. Efficient generation of picosecond and femtosecond pulses with high repetition rate across the visible and infrared regions were obtained by the optically pumped VECSEL (Vertical External Cavity surface Emitting Laser) technology. VECSELs are semiconductor lasers which have a surface-emitting semiconductor lasing medium which is vertically pumped in contrast to edge-emitting semiconductor lasers. A VECSEL laser basically consists of a gain chip with the gain region, made of quantum well or quantum dot layers, sandwiched between a monolithically integrated highly reflective semiconductor DBR (distributed Bragg reflector) and an antireflection surface. Several continuous-wave and mode-locked lasers have been reported based on VECSEL technology. Pulse durations as small as 110 fs [16] and kW range peak power levels have been reported from the wavelength flexible VECSEL laser systems. Figure 1.1 gives a wide spectrum of average output powers and pulse duration reported for different wavelengths by different type of VECSELs [17]. VECSELs are generally tunable due to the flexibility of bandgap engineering in

semiconductors, with tuning ranges in 10's of nm. VECSELs are hard to make in the visible region due to losses induced by free carrier absorption and for wavelengths greater than 1100 nm, they have relatively low power (microwatt range).

There are many other bulk or fibre materials for generating laser output. Common host materials include crystals or fibres like silicate, phosphate and fluoride glasses doped by rare-earth laser active ions like neodymium (946 nm, 1064 nm, 1319 nm), ytterbium (970-1150 nm), erbium ($\sim 1.55 \mu\text{m}$) and holmium ($\sim 2.1 \mu\text{m}$) [18-20]. Neodymium doped lasers are the most studied, and lasers around 1064 nm are widely accessible in application laboratories.

Nonlinear conversion is often employed to generate visible laser sources, the simplest of which is second harmonic generation (SHG) or sum frequency mixing (SFG) to extend the wavelengths of existing lasers. Optical parametric oscillators (OPO) [21, 22] form another class of lasers that generate multiple frequencies by tunable down-conversion of pump photons. It is interesting to note that the first optical parametric oscillator was developed by Giordmaine and Miller in 1965 [23] in lithium niobate. We demonstrate a Raman laser based on the same lithium niobate in this thesis. OPOs in combination with Ti:Sapphire lasers and frequency conversion can access almost any desired wavelength. However, commercial systems are extremely expensive and have a reputation for unreliability. Despite the capability of OPOs, there is still the need for reliable and inexpensive access to wavelengths away from the laboratory standards of Ti:Sapphire and neodymium lasers.

Raman lasers are yet another class of lasers which have been employed successfully for extending the wavelength reach of existing laser systems as well as to attain pulse compression. Raman lasers utilise the phenomenon of Raman scattering to generate different frequencies from the pump frequency, shifted down in energy equal to the vibrational energy levels of the medium. Raman lasers usually form an add-on to existing lasers, thereby making it possible to reach new wavelengths from existing infrastructure. Raman lasers have developed into an efficient practical class of lasers with their unique characteristics like beam clean-up [24], pulse compression [25] and

beam combination [26]. This thesis deals with the development of ultrafast Raman lasers in diamond and lithium niobate crystals.

1.3 Introduction to Raman lasers

Raman lasers use an amplifier medium based on Stimulated Raman Scattering (SRS), different from the conventional lasers which use stimulated emission from excited atoms. SRS is the nonlinear counterpart of the Raman Effect discovered by Chandrasekhara Venkata Raman (1888–1970) and his student Kariamanikam Srinivasa Krishnan [27, 28] in the late 1920s. G. S. Landsberg and L. I. Mandelshtam observed the similar phenomenon in crystals [29]. The American physicist Robert Williams Wood stated: *“It appears to me that this very beautiful discovery, which resulted from Raman’s long and patient study of phenomena of light scattering, is one of the most convincing proofs of the quantum theory of light which we have at the present time.”*[30]

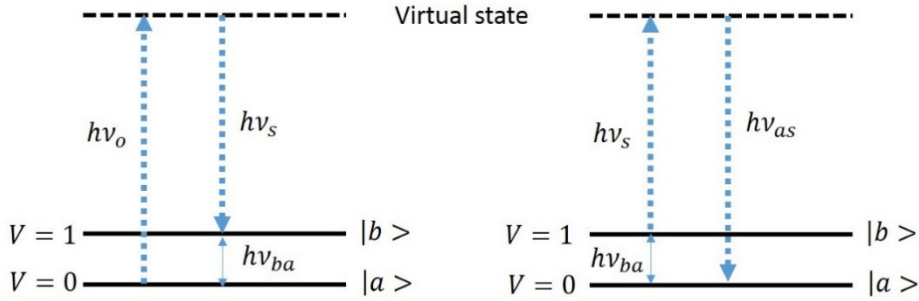


Fig. 1.2 (Left) Stokes generation (Right) Anti-Stokes generation.

The basic Raman process is an inelastic light-scattering process in which an incident quantum $h\nu_o$ gets scattered into a quantum $h\nu_s$, (ν_s is the Stokes frequency, smaller than the incident frequency) while the difference in energy $h(\nu_o - \nu_s) = h\nu_{ba}$ is absorbed by the material scattering center, driving a vibration in the Raman medium. Raman scattering can be associated with vibrational or rotational excitation of a molecule, or a lattice vibration (phonon) in solid-state Raman materials. If the system is in an excited state to begin with, it may make a transition to a lower energy state

while the light is scattered. In that case the scattered light contains the anti-Stokes frequency, $\nu_{as} = \nu_s + \nu_{ba}$, (figure 1.2).

With the first demonstration of lasers in 1960 by Theodore Maiman, highly coherent intense light sources became available and Raman spectroscopy witnessed a milestone with the observation of stimulated Raman scattering [31] while studying Q-switching of a ruby laser with a nitrobenzene Kerr cell. In the stimulated Raman process, a light wave at frequency ν_s is incident on the material system simultaneously with a light wave at ν_0 . A quantum $h\nu_s$ is added to the wave at ν_s , which consequently gets amplified, while the incident light beam loses a quantum $h\nu_0$ and the material is excited by a quantum $h(\nu_0 - \nu_s)$ (Figure 1.3-Right). Thus the stimulated process of the Stokes and the pump beams driving coherent excitation of phonons in the medium cause exponential gain for the Stokes beams until the pump beam gets depleted. SRS is a nonlinear phenomenon that can be described by a $\chi^{(3)}$ coefficient describing the cubic response of the material polarization to the incident fields.

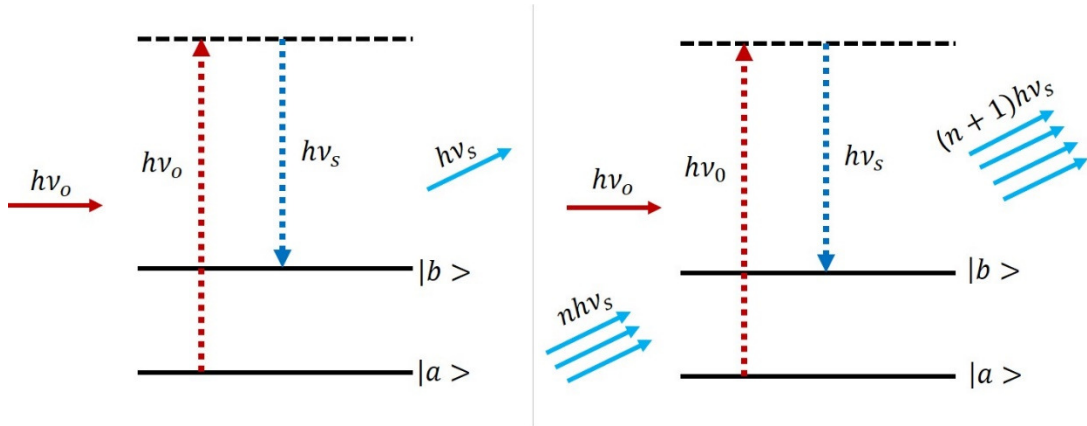


Fig. 1.3 (Left) Spontaneous and (Right) Stimulated Raman scattering.

SRS is typically driven by an incident laser beam, and grows from an initial incident Stokes beam or spontaneous Stokes noise. In contrast to spontaneous Raman scattering where the generation of incoherent Stokes light merely depends on the intensity of incident pump light, the generation of the coherent Stokes field in SRS relies on the intensity of both incident pump and generated Stokes beams.

One of the advantages of the stimulated Raman process is that it requires no phase matching conditions to be satisfied. This is due to the driven phonons automatically taking the phase required to couple power from the pump to the Stokes fields. This is viewed as an advantage of Raman lasers over other frequency conversion lasers like optical parametric oscillators where the phase matching condition necessitates very precise control of the nonlinear medium orientation and temperature. Raman lasers are very less sensitive to temperature and angle of the crystal. The gain of a Raman laser depends on the intensity of the pump laser unlike conventional lasers which depend on the magnitude of the population inversion. Raman laser sources do have similar properties to that of standard solid-state lasers sources like narrow line-width, low divergence, high coherence, and exponential small-signal gain.

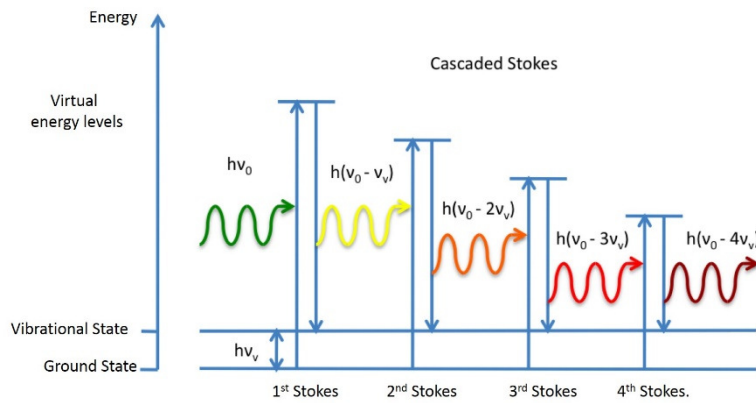


Fig. 1.4 Cascaded SRS process generating higher orders of Stokes.

Raman lasers can be robust practical and efficient devices to substantially extend the spectral coverage of solid-state lasers. Raman lasers can efficiently generate a number of wavelengths from the existing lasers common in laboratories. Extensive reviews on the solid-state Raman lasers by Helen Pask *et. al.* can be found in [32, 33], by P. Cerny *et. al.* in [34], Zverev *et. al.* in [35], to name a few. A complete list of Raman active crystals is given by Basiev *et. al.* in [36] and Alexander Kaminski in [37]. The frequency shift caused depends upon the crystal medium chosen [32]. The Stokes wavelength generated can be further shifted to longer wavelengths by the

process of cascading, providing the possibility of multiple frequency generation as shown in figure 1.4.

There are many robust and stable Raman crystal materials. The yttrium vanadate crystal, which has developed into a widely used standard commercial laser material, is one of the best Raman crystals [38-40], making Raman laser technology robust for commercialisation with no degradation of the crystal over time. Since the Raman process works over a wide range of frequencies, wavelength extendibility can be achieved for the infrared, visible and even to the ultraviolet pump lasers. Figure 1.5 demonstrates the versatility of Raman lasers which can reach a number of wavelengths, with greater flexibility obtained by using standard frequency doubling (SHG) and sum frequency generation (SFG) [33].

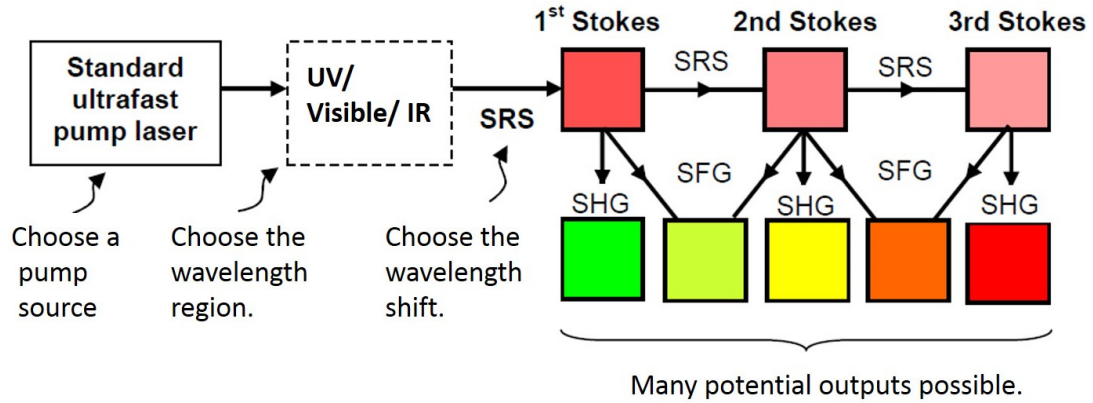


Fig. 1.5 Versatility of Raman lasers with multiple frequency generation.

SRS also has an advantageous property of “Raman beam cleanup” and has been extensively used for cleaning-up highly aberrated laser beams [24, 41-44] where the stimulated scattering process improves the beam quality factor (M^2) of the scattered beam. The beam quality factor (M^2) determines the quality of laser beam and is defined as the ratio of the beam parameter product (BPP) of the given beam to that of a diffraction-limited Gaussian beam of same wavelength, (λ/π) . The BPP is the product of beam radius (measured at the beam waist) and the beam divergence half-angle (measured in the far field), and we can write

$$M^2 = \frac{\theta \pi \omega_o}{\lambda} \quad (1.1)$$

where θ is the half-angle beam divergence, ω_o is the beam radius at the beam waist and λ is the wavelength.

1.4 Transient and Steady state SRS regimes

A Raman media experiences induced vibrations owing to the pump and Stokes fields and it takes a finite time for these lattice vibrations to reach steady-state, resulting in two basic time domains for SRS. Depending upon the pulse duration (τ_p) of the pump laser used and the dephasing time (T_2) of the Raman media, SRS can be classified into steady-state and transient regimes. The dephasing time (T_2) can be defined as the time it takes the phase of the vibrations in a Raman medium to be randomized by processes like phonon-phonon scattering.

The steady-state regime occurs when the pump pulse duration (τ_p) is much longer than the dephasing time of the medium. When the pump pulse duration (τ_p) becomes comparable or less than the pump pulse duration, we have the transient regime. In the steady-state regime, the Raman gain achieves its maximum value at steady state of the process, while in the transient regime, we obtain reduced gain for a given intensity. The Stokes intensity growth in steady-state and strongly transient regimes are given by equations (1.2) and (1.3) respectively [45].

$$I_s(z) = I_s(0)e^{g_R I_p z} \quad (1.2)$$

$$I_s(z) = I_s(0)e^{\sqrt{\frac{8g_R F_p z}{T_2}}} \quad (1.3)$$

where $I_s(0)$ is the intensity of either the incident Stokes field or more usually the spontaneous Stokes noise, I_p is the pump intensity, g_R is the steady state Raman gain coefficient and F_p is the pulse fluence which is proportional to pulse energy.

For crystals the dephasing time is usually of the order of picoseconds. The pump laser that we use in the Raman lasers in this thesis is a continuous-wave mode-locked Nd:YVO₄ laser with pulse duration of 15 picoseconds. Thus the ultrafast Raman lasers fall in the transient regime of SRS.

The transient regime of SRS involves different dynamics when compared to nanosecond or continuous wave Raman lasers which fall in the steady-state regime. The steady-state regime has Raman gain linearly proportional to pump intensity I_p , interaction length z , and the SRS gain coefficient. Decreasing τ_p for a fixed pulse energy thus increases I_p and increases gain. In contrast, the highly transient regime has Raman gain proportional to \sqrt{z} and $\sqrt{F_p}$ [46]. So gain depends only on pulse energy and not on pulse duration. Increasing I_p by decreasing τ_p in this regime thus has no effect.

1.4.1 Theory of Transient SRS

A detailed theory of Raman interactions have been provided by Penzkofer *et. al.* [45] as well as Kaiser *et. al.* [47] in 1972. The semi-classical approach involves classical treatment of the light fields by using Maxwell's equations, while the physical system is treated quantum mechanically. The interaction of pump and Stokes fields are considered only in forward and backward cases of interactions on geometrical considerations. Energy and momentum is conserved when:

$$\omega_L = \omega_S + \omega_r \quad (1.4)$$

$$k_L = k_S + k_r \quad (1.5)$$

where ω and k are the frequency and the wave vectors of the pump photon, Stokes photon and vibrational phonon with subscripts L, s and r respectively. We model forward scattering by looking for plane wave solutions for the vibrational wave ($\langle q \rangle$), Stokes and pump fields (E) and the induced polarization (P^{NL}) given by:

$$\langle q \rangle = \frac{1}{2} (Q e^{ik_r x - i\omega_r t} + c.c) \quad (1.6)$$

$$E = \frac{1}{2} (E_L e^{ik_L x - i\omega_L t} + E_S e^{ik_S x - i\omega_S t} + c.c) \quad (1.7)$$

$$P^{NL} = \frac{1}{2} (P_L^{NL} e^{ik_L x - i\omega_L t} + P_S^{NL} e^{ik_S x - i\omega_S t} + c.c) \quad (1.8)$$

where Q is the amplitude of material excitation and sub-indices S and L represent Stokes and pump laser fields respectively. A vibrational wave $\langle q \rangle$ at resonant

frequency ω_r is generated by the pump and Stokes fields which results in a time-varying polarizability. The induced polarization can be given as [45]:

$$P^{NL} = N \left(\frac{\partial \alpha}{\partial q} \right) \langle q \rangle E + P_{NR} \quad (1.9)$$

where N is the number density of lattice bonds and $\partial \alpha / \partial q$ is the first derivative of polarizability with respect to intermolecular distance q [48]. P_{NR} is the non-Raman polarization.

The nonlinear polarization for the pump and Stokes fields depending upon the material excitation Q can be obtained by substituting equations (1.6) and (1.7) into (1.9).

$$P_S^{NL} = \frac{1}{2} N \left(\frac{\partial \alpha}{\partial q} \right) Q^* E_L + \chi_{NR}^{(3)} |E_L|^2 E_S \quad (1.10)$$

$$P_L^{NL} = \frac{1}{2} N \left(\frac{\partial \alpha}{\partial q} \right) Q E_S + \chi_{NR}^{(3)} |E_S|^2 E_L \quad (1.11)$$

The propagation of the above fields is governed by the Maxwell's equation [48]:

$$\nabla^2 E - \left(\frac{\mu}{c} \right)^2 \frac{\partial^2}{\partial t^2} E - \frac{\gamma \mu}{c} \frac{\partial}{\partial t} E = \frac{4\pi}{c^2} \frac{\partial^2}{\partial t^2} P^{NL} \quad (1.12)$$

In which γ is the absorption coefficient with the third term representing linear losses and μ is the refractive index. The left hand side of equation (1.12) is just linear propagation while the right hand side with P^{NL} represents the nonlinear contribution which in fact is responsible for gain or loss. Equations (1.10) and (1.11) can be substituted into the Maxwell's equation. Terms with equal frequency and wave-vectors can be equated to get a new set of differential equations to describe the interaction. Some approximations like $1/\omega_i \partial/\partial t \ll 1$, $1/\omega_i^2 \partial^2/\partial t^2 \ll 1$, $1/T_2 \ll \omega_r$ (i stands for r , S and L), can be made for pulses with slowly varying envelopes compared with the carrier wave. We find,

$$\frac{\partial E_S}{\partial x} + \frac{\mu_S}{c} \frac{\partial E_S}{\partial t} + \frac{\gamma_S}{2} E_S = i \frac{2\pi\omega_S}{c\mu_S} \left[\frac{1}{2} N \left(\frac{\partial \alpha}{\partial q} \right) Q^* E_L + \chi_{NR}^{(3)} |E_L|^2 E_S \right] \quad (1.13)$$

$$\frac{\partial E_L}{\partial x} + \frac{\mu_L}{c} \frac{\partial E_L}{\partial t} + \frac{\gamma_L}{2} E_L = i \frac{2\pi\omega_L}{c\mu_L} \left[\frac{1}{2} N \left(\frac{\partial \alpha}{\partial q} \right) Q E_S + \chi_{NR}^{(3)} |E_S|^2 E_L \right] \quad (1.14)$$

The differential equations are related to excitation amplitude Q :

$$\frac{\partial Q}{\partial x} + \frac{i}{2\omega_r} \left(\omega_0^2 - \omega_r^2 - i \frac{2\omega_r}{T_2} \right) Q = \frac{i}{4m\omega_r} \left(\frac{\partial \alpha}{\partial q} \right) E_L E_S^* \quad (1.15)$$

By applying the condition of resonance, $\omega_r = \omega_0$, and neglecting linear losses and group velocity dispersion to the general equations of (1.13) to (1.15), we obtain:

$$\frac{\partial E_S(x, t)}{\partial x} + \frac{1}{v_s} \frac{\partial E_S}{\partial t} = i \frac{\pi \omega_S}{c \mu_S} \left(\frac{\partial \alpha}{\partial q} \right) N E_L Q^* \quad (1.16)$$

$$\frac{\partial E_L(x, t)}{\partial x} + \frac{1}{v_L} \frac{\partial E_L}{\partial t} = i \frac{\pi \omega_L}{c \mu_L} \left(\frac{\partial \alpha}{\partial q} \right) N E_S Q \quad (1.17)$$

$$\frac{\partial Q(x, t)}{\partial T} + \frac{1}{T_2} Q = \frac{i}{4m\omega_0} \left(\frac{\partial \alpha}{\partial q} \right) E_L E_S^* \quad (1.18)$$

Finally, the variable Q is changed to Q' as:

$$Q' = \frac{mc\mu_S\mu_L\omega_0}{4\pi\omega_S \left(\frac{\partial \alpha}{\partial q} \right) T_2} Q \quad (1.19)$$

and the equations are cast in a frame moving at the Stokes group velocity according to $x' = x - v_s t$ and $t' = t$ and the coupled differential equations are transformed into:

$$\frac{1}{v_s} \frac{\partial E_S}{\partial t'} = i g_S \frac{\omega_S}{\mu_S} E_L Q'^* \quad (1.20)$$

$$\left(1 - \frac{v_s}{v_L} \right) \frac{\partial E_L}{\partial x'} + \frac{1}{v_L} \frac{\partial E_L}{\partial t'} = i g_S \frac{\omega_L}{\mu_L} E_S Q' \quad (1.21)$$

$$\frac{\partial Q'}{\partial t'} - v_s \frac{\partial Q'}{\partial x'} + \frac{1}{T_2} Q' = i \frac{c\mu_S\mu_L}{16\pi\omega_S T_2} E_L E_S^* \quad (1.22)$$

with the Raman gain given by:

$$g_S = N \left(\frac{\partial \alpha}{\partial q} \right)^2 \frac{4\pi^2 \omega_S}{\mu_S \mu_L c^2 m \omega_0} \frac{1}{T_2} \quad (1.23)$$

Equation (1.21) clearly describes a scattering process, with the pump photons scattering of the phonon field to drive the Stokes field. Equation (1.22) shows the phonon field driven by the pump and the Stokes fields, and decaying at the rate of $(1/T_2)$. These coupled differential equations have been used for modelling Raman lasers in transient regime [25] and are used to explain the pulse compression in

synchronous Raman lasers. Note that in steady-state, we have $Q' \propto E_L E_S^*$ and so $\frac{\partial E_S}{\partial t} \propto E_S |E_L|^2 g_R$ which describes exponential gain for I_S as $I_S(0) = I_S(z) e^{g_R L z}$.

1.5 Raman laser design considerations

The important considerations while building a Raman laser are choosing the right crystal and deciding the cavity design. These considerations rely upon the nature of available pump sources as well as the required Stokes wavelengths. As mentioned in the previous section, there are plenty of laser crystals available on the market and for each of these we can also consider what new wavelengths can be reached using Raman lasers. While designing the cavity, one must consider the different wavelengths generated in the system, as the Raman process can generate multiple wavelengths by cascading, which would need careful selection of the mirror coatings to allow maximum efficiency for required wavelengths.

1.5.1 Raman laser crystals

The choice of Raman crystal rests upon several factors like the targeted wavelength, Raman gain coefficient, optical damage threshold, thermal properties and possibilities of other parasitic nonlinear processes that would hinder the Raman conversion efficiency. There are hundreds of crystals studied for Raman activity; key crystals are listed in table with their SRS spectral properties from [32, 34, 36, 40, 49-52].

Raman gain determines laser threshold and so affects overall efficiency. Covalently bonded crystals are usually found to have higher Raman gain compared to ionic crystals. Diamond is found to have the highest gain of ~ 20 cm/GW at 1064 nm with superior thermal properties. Advances in the field of crystalline Raman lasers have been possible due to the availability of high quality crystals and identifying Raman conversion possibility in crystals that are already in use for other standard applications like tungstates, vanadates and diamond. There is numerous literature on Raman activity in tungstates [37] which are broadly classified as double-metal tungstates and tetragonal tungstates. They are widely used in wavelength shifting of

visible light due to high gain and narrow linewidth. Some high gain crystals have other drawbacks like durability, low damage threshold. Barium nitrate which has high Raman gain but deteriorates when used at moderate powers and is hygroscopic.

Table 1.1 Important optical properties of some of typical Raman crystals [34, 40, 50-53].

Crystal	Raman Shift (cm ⁻¹)	Raman Linewidth (cm ⁻¹)	Integra. Cross-section (A.U.)	Raman Gain (cm/GW)	T_2 (ps)
Diamond	1332	2.7	100	~20	6.2
KGd(WO ₄) ₂	901	5.4	54	5.2	3.1
KGW	768	6.4	59	5.7	2.6
LiNbO ₃	628	27	166	11.5	0.6
	248	28	100	12	0.6
YVO ₄	892	3.0	92	> 4.5	5.6
BaWO ₄ (BW)	926	1.6	52	8.5	10.4

Some of the vanadate crystals like GdVO₄, YVO₄ which can host laser ions have been used in “self-Raman” laser systems which have the pump generation and the Raman activity happening in the same crystal [53-56]. This design can lead to very simple Raman lasers that can be just as robust as their conventional counterparts.

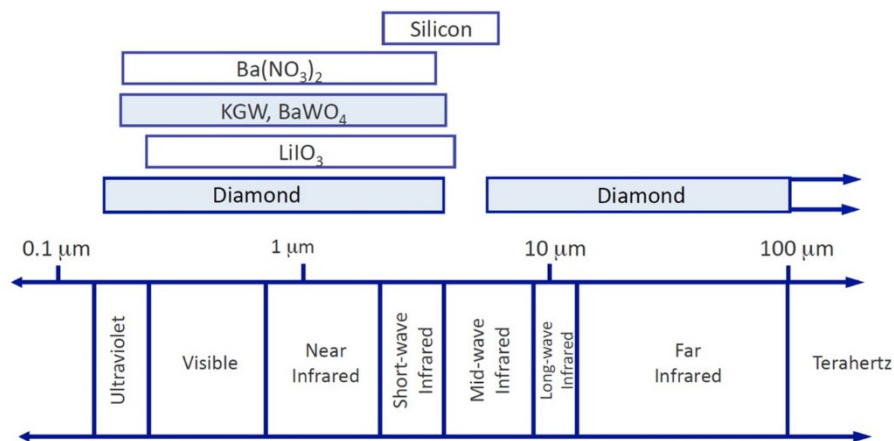


Fig. 1.6 Transparency range of some of the typical Raman crystals [57].

While considering crystals for Raman lasers, transparency of the crystal is to be taken into account as those Stokes wavelengths which do not fall in the transparency

window cannot be generated. Diamond is found to have a transparency over a wide range of wavelengths. Figure 1.6 compares the transparency window of many crystals, showing diamond's unique capabilities [57].

Thermal properties of the crystal is yet another matter for consideration. With the Raman process being inelastic, the induced vibration is dissipated as heat deposited in the crystal. At high average powers, the induced heat can cause other processes like thermal lensing which would affect the performance of the laser. It has been found that high thermal conductivity and low thermo-optic coefficients are key properties for selection of Raman crystals for high power laser operation. The high thermal conductivity of diamond forms another advantageous factor for power scaling.

1.5.2 Raman laser cavity designs

There exist numerous cavity designs for lasers that employ SRS for wavelength generation. The commonly used cavities can be broadly divided into three configurations as shown in figure 1.7. The first of the three is a simple *Raman generator*. It is the simplest of the designs with only a pump beam, focused into the Raman crystal to generate a Stokes beam by SRS in a single pass. This arrangement is used for picosecond or femtosecond Raman generation with low repetition rate amplified pump lasers owing to the very high intensity required in the range of GW/cm^2 . A gain of the order of e^{25} is required to generate Stokes output amplified from spontaneous Raman scattering. Very high conversion efficiency have been obtained by this design. For instance, a conversion efficiency as high as 92 % was obtained in single pass generation using second harmonic of a Nd:YAG mode-locked laser system with 35 ps pulse duration and energy up to 1 mJ in [58] with simultaneous generation of multiple Stokes wavelengths. These generators do have the disadvantage of not having the possibility to control the Stokes beam quality or cascading. Raman generators were recently demonstrated by Fairnello *et. al.* [59] where the authors developed and compared Raman generators based on SrWO_4

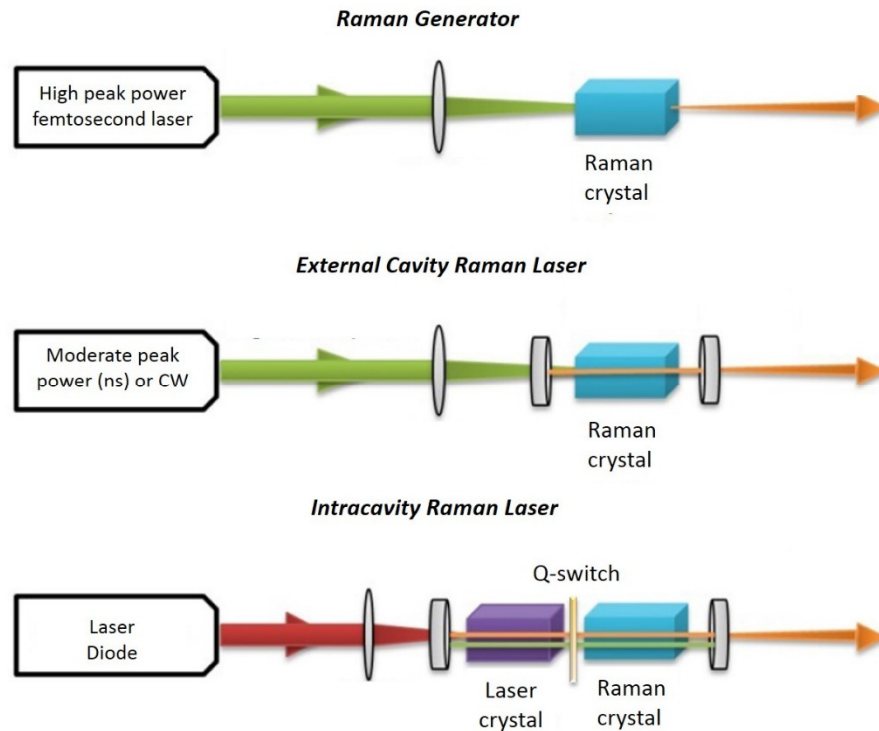


Fig. 1.7 General Raman laser cavity designs.

crystals using two different master oscillator power amplifier (MOPA) pump laser systems with 15 ps duration (from hybrid fibre solid-state mode-locked MOPA pump) for transient SRS operation and 550 ps (from a passively Q-switched MOPA pump) duration for steady-state SRS operation. High pump intensities of the order of GW/cm^2 were required to reach the threshold for Stokes generation in both regimes ($7.7 \text{ GW}/\text{cm}^2$ for the transient regime and $3.6 \text{ GW}/\text{cm}^2$ for the steady-state regime) [59]. Out of the two configurations, the transient regime one had higher threshold for Stokes generation as an example. Significant improvement in optical-to-optical conversion efficiency was observed for Stokes generation for the transient operation (37 %) compared to steady-state operation (28 %).

To reduce the threshold it is desirable to place the Raman crystal inside a resonator resulting in an *External Cavity Raman Laser* system. This resonator allows the generated Stokes fields to resonate in the cavity and be amplified over many passes. The external cavity Raman laser configuration is only suitable for pump lasers whose duration is much greater than the transit time of the crystal so that the Stokes can

indeed build up over many round trips. The cavity is formed by an input coupler and an output coupler: The input coupler needs to be highly transmitting for the pump wavelength and highly reflective for the Stokes wavelength. The required pump beam intensity is considerably reduced to 1 to 100 MW/cm² compared to the Raman generators (range of GW/cm²). The output coupler would be partially transmitting for the Stokes wavelength, and can be highly reflective for the pump wavelength to achieve two passes of the pump beam. This configuration has been widely used in moderate peak power systems like nanosecond and continuous regimes. The first continuous wave Raman laser employed an external cavity Raman laser design which generated output power of 150 mW [60] in a barium nitrate crystal. Some of the laser systems employing the external cavity Raman laser configuration based on barium nitrate and potassium gadolinium tungstate crystals have shown high conversion efficiencies such as 60 % [61, 62].

The third kind of cavity design is called an *Intracavity Raman Laser* where the Raman crystal is placed inside the cavity of a conventional solid-state laser (like an Nd laser at 1064 nm), avoiding the necessity of an additional cavity for the Raman crystal. Both the pump and the Stokes fields share the same cavity mirrors having high reflectivity for the laser wavelength and appropriate output coupling for the Stokes wavelengths. The Raman crystal, being inside the laser cavity, experiences the intense intracavity pump field enabling efficient Raman conversion. This means that the intracavity design allows the Raman conversion of lower power lasers which otherwise would not have enough power to enable SRS. A Q-switch can be inserted into the cavity for generation of pulses or the laser can run in continuous wave mode. The first diode-pumped crystalline Raman lasers were demonstrated using an intracavity configuration in Q-switched [63] and continuous wave [64] regimes.

Some Raman materials can accommodate laser active ions such as Neodymium (Nd) or Ytterbium (Yb) making it possible to generate the fundamental as well as the Stokes wavelengths in the same crystal, called self-Raman crystals. Using a self-Raman crystal has the advantage of compactness and less loss due to the absence of an extra crystal for Raman activity. But they suffer from strong thermal lensing as the

self-Raman crystal is subjected to additional heat caused by SRS in addition to the pump lasing. Detailed treatment of thermal lensing in Raman crystal can be found in [32]. The first Nd doped self-Raman laser was reported in KGW by Grabtchikov *et. al.* [53]. Several other crystal were also reported for self-Raman activity, Nd:Ca(NbO₃) [54], Nd:PbWO₄ [55], Nd:SrWO₄ [56], which however suffered from poor thermal characteristics. Neodymium doped vanadate crystals, on the other hand, have achieved efficient conversion at multi-Watt level such as Nd:YVO₄ [65-68], Nd:GdVO₄ [69-71] and Nd:LuVO₄ [72].

While each cavity design has its own unique properties and features, the pump laser that is being used determines the optimum design for use. High peak power pump lasers can employ the external cavity design as well as Raman generator design and are relatively simple. Such lasers would form “add-on” systems which can be added to any existing laser system to extend the wavelength accessibility. On the other hand the intracavity design is much complex but more suitable for low power lasers and CW lasers, as the threshold for SRS is more easily attained.

1.6 Synchronously pumped Raman laser approach to ultrashort pulses

Ultrafast Raman laser systems, pumped by ultrafast laser pulses, have more complicated design considerations when compared to systems pumped by continuous wave or nanosecond pulses. The Raman generators, which use a single pass process, suffer from low beam quality and also do not allow control over the cascading process [34] and need amplified laser systems to reach the threshold. On the other hand the pulse duration of ultrafast lasers are so short that a resonating cavity field cannot build up in a simple external cavity Raman laser.

Hence we employ a scheme known as synchronous pumping [73-75] for all the laser systems explored in this thesis. This design allows Raman conversion of nJ-scale ultrafast lasers. Synchronous pumping involves making a Raman cavity the exact length of the pump laser cavity. In other words, the roundtrip time of the pulse circulating in the Raman laser is made equal to the inter-pulse time of the train of pulses from the pump laser so that a circulating Stokes pulse gets amplified by

successive pump pulses. Synchronous pumping is an effective method for minimizing the pump power requirement since each pump pulse needs only cause sufficient amplification for the Stokes pulse to counter round-trip losses, needing a gain of order of $e^{0.1}$ compared to a Raman generator needing a gain of the order of e^{25} and hence 250 times higher pump intensity.

The three Raman laser systems explored in this thesis employ synchronous pumping using a mode-locked NdYVO₄ laser (*Spectra Physics Vanguard 2000-HM532*) that generated up to 4.8 W average power at 1064 nm with pulse duration of 15 ps, repetition rate of 80 MHz, and beam quality factor M^2 of 1.1. The picosecond diamond Raman laser explained in chapter 2 of this thesis forms the first synchronously pumped ring solid-state Raman laser [76].

The first synchronously pumped Raman laser was demonstrated by Colles *et. al.* in 1970 in liquid medium of benzene [77] generating Stokes pulses as short as 0.3 ps from 5 ps pump pulses. This demonstrates that pulse compression can be achieved. The first solid-state synchronously pumped Raman laser was demonstrated by Grigoryan *et. al.* in 1989 in a LiIO₃ crystal generating Stokes pulse of 1 ps duration [78]. Synchronous pumping can also be used for ultrafast optical parametric oscillators, which share many features such as no energy storage and pulse compression [79].

Synchronous pumping involves careful cavity length tuning to reach the perfect synchronization. In the characterization of the laser cavities mentioned in this thesis, the perfect synchronization cavity length ($\Delta x = 0$) is defined as the cavity length for which the Raman laser experiences minimum threshold. Similar to OPOs, here in Raman lasers, pulse compression is achieved by group velocity dispersion of the pump and the Stokes fields in the crystal. Detuning of the cavity from the perfect synchronization length demands pulse reshaping mechanisms leading to pulse compression. This is discussed in detail in next chapter.

Efficient external cavity Raman lasers employing the synchronous pumping scheme have been reported for Q-switched mode-locked pump lasers with μJ or mJ scale energies [80] as well as CW-mode-locked pump lasers with nJ scale energies in visible [74, 81] and UV [82] regions. The diamond Raman laser demonstrated by the author of this thesis [76] as well as those reported by Murtagh *et. al.* [83, 84] extend the possibilities of CW mode-locked lasers, by utilising the synchronously pumped external cavity design, into the IR region.

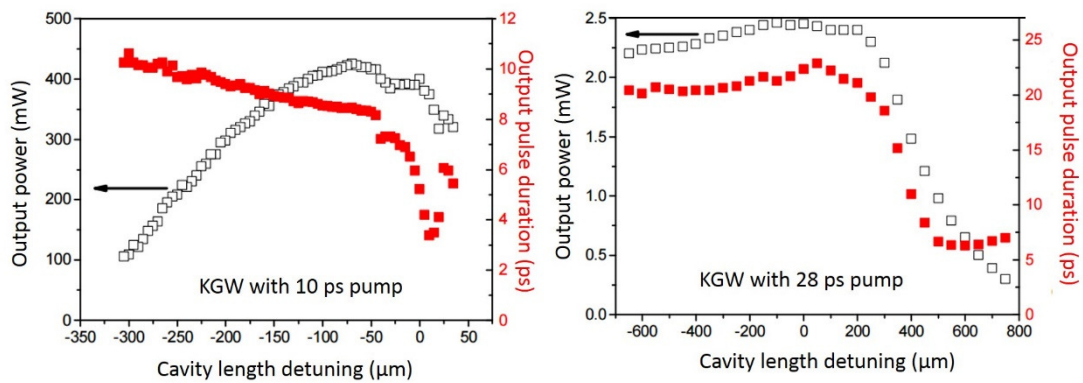


Fig. 1.8 Different laser characteristics of KGW Raman laser pumped by different pump pulse duration picosecond lasers, from [85].

In [85] the authors make a comparative study of synchronously pumped Raman lasers pumped by 532 nm in KGW and Diamond crystals with different pulse durations. Diamond has a higher Raman gain coefficient, longer dephasing time and higher thermal conductivity in comparison to KGW [86]. Pump lasers with 10 ps [74] and 28 ps [87] were used for the KGW Raman laser and 22.5 ps [81] pump pulses were employed for the Diamond based Raman laser. Although all the three were synchronously pumped systems, they demonstrated different observations related to pulse shortening mechanism as shown in figure 1.8 taken from [85] which shows the output power and pulse duration as a function of cavity length detuning for a 50 mm KGW crystal pumped by 10 ps and 28 ps green pulses with similar repetition rates. The comparatively less-transient case (28 ps pump) had higher threshold (1.7 W) than the 10 ps pumping case (0.6 W). The output power and the pulse duration of the Stokes behaved differently in both systems. While the 28 ps pumping

failed to maintain conversion efficiency during shorter pulse generation, 10 ps pump pulses had pulse shortening occurring with higher output Stokes power. Generation of such compressed pulses would find application in areas such as two-photon microscopy. The diamond crystal on the other had obtained lower threshold generation of 1.75 W even with a short crystal (7 mm compared to 50 mm) owing to higher Raman gain. The authors of [85] observed best pulse compression happening simultaneously with high Stokes power generation only when pumped with shorter pump pulses. Thus the pump pulse duration in regard to the dephasing time of the Raman medium plays an important role in deciding the pulse compression mechanics.

1.7 Chapter Summary

Ultrafast solid-state Raman lasers are an efficient and convenient method of extending the wavelength reach of existing laser systems. The variety of choices in Raman crystal medium available on the market presents us with multiple possibilities of wavelength generation.

The basic idea of SRS was introduced along with a brief overview of the existing solid-state Raman lasers. Depending upon the response time of the Raman media and the pulse duration of the pump laser, SRS is classified into transient or steady-state regimes. Ultrafast Raman lasers based on crystals fall in the transient regime. The theory of transient SRS was briefly covered with description of the coupled differential equations that are usually employed for theoretical modelling of ultrafast Raman lasers.

The major considerations for Raman laser development including the crystal selection and cavity design was discussed. The synchronous pumping scheme needed for ultrafast Raman lasers was treated in detail with a review of synchronously pumped Raman lasers developed in recent times. The laser systems developed in this thesis employ the synchronous pumping scheme. This scheme allows conversion of nJ-scale picosecond pulses that would be too weak to pump a Raman generator. While there have been investigations using synchronously pumped Raman lasers in

the visible and ultraviolet, there has been no work in the more common infrared range.

In the following chapters of this thesis,

- We develop a highly efficient first Stokes Raman laser in diamond at 1240 nm pumped by a 1064 nm, 15 ps, 80 MHz NdYVO₄ laser. Pulse shortening, characteristic of synchronously pumped lasers, was also observed. We also demonstrate efficient and simple generation of second Stokes at 1485 nm in the same system by parametric coupling of SRS components.
- We develop a lithium niobate Raman laser which can access selectable and controllable multiple wavelengths by using stimulated Raman scattering (SRS) and stimulated polariton scattering (SPS).
- We develop a terahertz wave generator based on cascading of cavity enhanced Stokes fields by SPS in a lithium niobate crystal, thus demonstrating a simple approach to terahertz generation from mode-locked nJ-scale picosecond lasers.

1.8 References for Chapter 1

- [1] A. DeMaria, D. Stetser, H. Heynau, Self mode-locking of lasers with saturable absorbers, *Applied Physics Letters*, 8 (1966) 174-176.
- [2] M. Chini, K. Zhao, Z. Chang, The generation, characterization and applications of broadband isolated attosecond pulses, *Nature Photonics*, 8 (2014) 178-186.
- [3] F. Korte, J. Serbin, J. Koch, A. Egbert, C. Fallnich, A. Ostendorf, B. Chichkov, Towards nanostructuring with femtosecond laser pulses, *Applied Physics A*, 77 (2003) 229-235.
- [4] R.A. Bartels, A. Paul, H. Green, H.C. Kapteyn, M.M. Murnane, S. Backus, I.P. Christov, Y. Liu, D. Attwood, C. Jacobsen, Generation of spatially coherent light at extreme ultraviolet wavelengths, *Science*, 297 (2002) 376-378.
- [5] M. Ferray, A. l'Huillier, X. Li, L. Lompre, G. Mainfray, C. Manus, Multiple-harmonic conversion of 1064 nm radiation in rare gases, *Journal of Physics B: Atomic, Molecular and Optical Physics*, 21 (1988) L31.
- [6] J. Noack, A. Vogel, Laser-induced plasma formation in water at nanosecond to femtosecond time scales: calculation of thresholds, absorption coefficients, and energy density, *Quantum Electronics, IEEE Journal of*, 35 (1999) 1156-1167.
- [7] A. Depresseux, E. Oliva, J. Gautier, F. Tissandier, G. Lambert, B. Vodungbo, J. Goddet, A. Tafzi, J. Nejdli, M. Kozlova, Demonstration of a Circularly Polarized Plasma-Based Soft-X-Ray Laser, *Physical Review Letters*, 115 (2015) 083901.
- [8] R. Senz, G. Müller, Laser in medicine, *Berichte der Bunsengesellschaft für physikalische Chemie*, 93 (1989) 269-277.
- [9] J. Girkin, G. McConnell, Advances in laser sources for confocal and multiphoton microscopy, *Microscopy research and technique*, 67 (2005) 8-14.
- [10] E.B. Brown, J.B. Shear, S.R. Adams, R.Y. Tsien, W.W. Webb, Photolysis of caged calcium in femtoliter volumes using two-photon excitation, *Biophysical Journal*, 76 (1999) 489-499.
- [11] L. Johnson, R. Dietz, H. Guggenheim, Optical Maser Oscillation from Ni^{2+} in MgF_2 Involving Simultaneous Emission of Phonons, *Physical Review Letters*, 11 (1963) 318.
- [12] P. Moulron, Ti-doped Sapphire Tunable Solid State Laser, *Opt. News*, 8 (1982).

- [13] D.E. Spence, P.N. Kean, W. Sibbett, 60-fsec pulse generation from a self-mode-locked Ti: sapphire laser, *Optics Letters*, 16 (1991) 42-44.
- [14] D.H. Sutter, G. Steinmeyer, L. Gallmann, N. Matuschek, F. Morier-Genoud, U. Keller, V. Scheuer, G. Angelow, T. Tschudi, Semiconductor saturable-absorber mirror–assisted Kerr-lens mode-locked Ti: sapphire laser producing pulses in the two-cycle regime, *Optics Letters*, 24 (1999) 631-633.
- [15] C. Shank, A. Dienes, W. Silfvast, single pass gain of excplex 4-MU and rhodamine 6G dye laser amplifiers, *Applied Physics Letters*, 17 (1970) 307-309.
- [16] P. Klopp, U. Griebner, M. Zorn, M. Weyers, Pulse repetition rate up to 92 GHz or pulse duration shorter than 110 fs from a mode-locked semiconductor disk laser, *Applied Physics Letters*, 98 (2011) 071103.
- [17] B.W. Tilma, M. Mangold, C.A. Zaugg, S.M. Link, D. Waldburger, A. Klenner, A.S. Mayer, E. Gini, M. Golling, U. Keller, Recent advances in ultrafast semiconductor disk lasers, (2014).
- [18] S. Poole, D.N. Payne, M.E. Fermann, Fabrication of low-loss optical fibres containing rare-earth ions, *Electronics Letters*, 21 (1985) 737-738.
- [19] R.J. Mears, L. Reekie, S. Poole, D.N. Payne, Neodymium-doped silica single-mode fibre lasers, *Electronics Letters*, 21 (1985) 738-740.
- [20] S. Yamashita, K. Hotate, Multiwavelength erbium-doped fibre laser using intracavity etalon and cooled by liquid nitrogen, *Electronics Letters*, 32 (1996) 1298-1299.
- [21] R.L. Byer, Optical parametric oscillators, *Quantum Electronics: A Treatise*, 1 (1975).
- [22] S.E. Harris, Tunable optical parametric oscillators, in, DTIC Document, 1970.
- [23] J. Giordmaine, R.C. Miller, Tunable Coherent Parametric Oscillation in LiNbO_3 at Optical Frequencies, *Physical Review Letters*, 14 (1965) 973.
- [24] R.S. Chang, R.H. Lehmberg, M.T. Duignan, N. Djeu, Raman beam cleanup of a severely aberrated pump laser, *Quantum Electronics, IEEE Journal of*, 21 (1985) 477-487.
- [25] E. Granados, D.J. Spence, Pulse compression in synchronously pumped mode locked Raman lasers, *Optics Express*, 18 (2010) 20422-20427.

- [26] J. Digman, R. Hollins, Beam combination in Raman amplifiers, in: *Nonlinear Optics: Materials, Fundamentals, and Applications*, 1994. NLO'94 IEEE, IEEE, 1994, pp. 370-372.
- [27] C.V. Raman, A new radiation, *Indian Journal of physics*, 2 (1928) 387-398.
- [28] C.V. Raman, K.S. Krishnan, A new type of secondary radiation, *Nature*, 121 (1928) 501-502.
- [29] G. Landsberg, L. Mandelstam, A new appearance in the light diffusion in crystals, *Naturwissenschaften*, 16 (1928) 772.
- [30] R.W. Wood, Wave-length shifts in scattered light, *Nature*, 122 (1928) 349.
- [31] E. Woodbury, W. Ng, Ruby laser operation in near IR (1962) pp. 2367-&.
- [32] H.M. Pask, The design and operation of solid-state Raman lasers, *Progress in Quantum Electronics*, 27 (2003) 3-56.
- [33] H. Pask, P. Dekker, R. Mildren, D. Spence, J. Piper, Wavelength-versatile visible and UV sources based on crystalline Raman lasers, *Progress in Quantum Electronics*, 32 (2008) 121-158.
- [34] P. Černý, H. Jelínková, P.G. Zverev, T.T. Basiev, Solid state lasers with Raman frequency conversion, *Progress in Quantum Electronics*, 28 (2004) 113-143.
- [35] P. Zverev, T. Basiev, A. Prokhorov, Stimulated Raman scattering of laser radiation in Raman crystals, *Optical Materials*, 11 (1999) 335-352.
- [36] T. Basiev, R. Powell, *Handbook of Laser Technology and Applications*, New York: Institute of Physics Publishing, 200 (2003) B1.
- [37] A.A. Kaminskii, *Laser crystals: their physics and properties*, Springer, 2013.
- [38] A.A. Kaminskii, K.-i. Ueda, H.J. Eichler, Y. Kuwano, H. Kouta, S.N. Bagaev, T.H. Chyba, J.C. Barnes, G.M. Gad, T. Murai, Tetragonal vanadates YVO_4 and GdVO_4 —new efficient $\chi^{(3)}$ - materials for Raman lasers, *Optics Communications*, 194 (2001) 201-206.
- [39] Y. Chen, M. Ku, L. Tsai, Y. Chen, Diode-pumped passively Q-switched picosecond $\text{Nd:GD}_x\text{Y}_{1-x}\text{VO}_4$ self-stimulated Raman laser, *Optics Letters*, 29 (2004) 2279-2281.
- [40] A. Kaminskii, K. Ueda, H. Eichler, Y. Kuwano, H. Kouta, S. Bagayev, T. Chyba, J. Barnes, T. Murai, J. Lu, Tetragonal vanadates YVO_4 and GdVO_4 —new efficient $\chi^{(3)}$ - active crystals for Raman laser converters, *Laser Physics*, 11 (2001) 1124-1133.

- [41] J. Goldhar, J.R. Murray, Intensity averaging and four-wave mixing in Raman amplifiers, *Quantum Electronics, IEEE Journal of*, 18 (1982) 399-409.
- [42] R. Chang, N. Djeu, Amplification of a diffraction-limited Stokes beam by a severely distorted pump, *Optics letters*, 8 (1983) 139-141.
- [43] V. Bespalov, A. Betin, G. Pasmanik, Reproduction of the pumping wave in stimulated-scattering radiation, *Radiophysics and Quantum Electronics*, 21 (1978) 675-688.
- [44] A. Flusberg, D. Korff, Wave-front replication versus beam cleanup by stimulated scattering, *JOSA B*, 4 (1987) 687-690.
- [45] A. Penzkofer, A. Laubereau, W. Kaiser, High intensity Raman interactions, *Progress in Quantum Electronics*, 6 (1979) 55-140.
- [46] R.L. Carman, F. Shimizu, C. Wang, N. Bloembergen, Theory of Stokes pulse shapes in transient stimulated Raman scattering, *Physical Review A*, 2 (1970) 60.
- [47] W. Kaiser, M. Maier, *Laser handbook*, N.-Holland, Amsterdam, 2 (1972) 1077.
- [48] N. Bloembergen, *Nonlinear optics*. 1965, in, New York: Benjamin.
- [49] A.A. Kaminskii, H.J. Eichler, K.-i. Ueda, N.V. Klassen, B.S. Redkin, L.E. Li, J. Findeisen, D. Jaque, J. Garcia-Sole, J. Fernández, Properties of Nd ³⁺-doped and undoped tetragonal PbWO₄, NaY(WO₄)₂, CaWO₄, and undoped monoclinic ZnWO₄ and CdWO₄ as laser-active and stimulated Raman scattering-active crystals, *Applied Optics*, 38 (1999) 4533-4547.
- [50] T.T. Basiev, A.A. Sobol, P.G. Zverev, V.V. Osiko, R.C. Powell, Comparative spontaneous Raman spectroscopy of crystals for Raman lasers, *Applied Optics*, 38 (1999) 594-598.
- [51] W. Johnston Jr, I. Kaminow, J. Bergman Jr, Stimulated Raman gain coefficients for Li⁶NbO₃, Ba₂NaNb₅O₁₅, and other materials, *Applied Physics Letters*, 13 (1968) 190-193.
- [52] W.D. Johnston, I.P. Kaminow, Temperature Dependence of Raman and Rayleigh Scattering in LiNbO₃ and LiTaO₃, *Physical Review*, 178 (1969) 1528-1528.
- [53] A. Grabtchikov, A. Kuzmin, V. Lisinetskii, V. Orlovich, G. Ryabtsev, A. Demidovich, All solid-state diode-pumped Raman laser with self-frequency conversion, *Applied Physics Letters*, 75 (1999) 3742-3744.

- [54] A. Kaminskii, J. Dong, K. Ueda, M. Bettinelli, M. Grinberg, D. Jaque, Q-switched nanosecond Nd³⁺:Ca(NbO₃)₂ crystalline self-Raman laser with single-step cascade SE ($\lambda_{SE} = 1.0615 \mu\text{m}$ of $^4F_{3/2} \rightarrow ^4I_{11/2}$ channel) \rightarrow SRS ($\lambda_{St1} = 1.1741 \mu\text{m}$ of $\omega_{SRS} \approx 904 \text{ cm}^{-1}$ promotion vibration mode) wavelength conversion, *Laser Physics Letters*, 6 (2009) 782.
- [55] W. Chen, Y. Inagawa, T. Omatsu, M. Tateda, N. Takeuchi, Y. Usuki, Diode-pumped, self-stimulating, passively Q-switched Nd³⁺:PbWO₄ Raman laser, *Optics Communications*, 194 (2001) 401-407.
- [56] L. Ivleva, T. Basiev, I. Voronina, P. Zverev, V. Osiko, N. Polozkov, SrWO₄:Nd³⁺—new material for multifunctional lasers, *Optical Materials*, 23 (2003) 439-442.
- [57] R.P. Mildren, The outlook for diamond in Raman laser applications, *MRS Proceedings*, Cambridge Univ Press, 2009, pp. 1203-J1213-1201.
- [58] P. Černý, H. Jelínková, Near-quantum-limit efficiency of picosecond stimulated Raman scattering in BaWO₄ crystal, *Optics Letters*, 27 (2002) 360-362.
- [59] P. Farinello, F. Pirzio, X. Zhang, V. Petrov, A. Agnesi, Efficient picosecond traveling-wave Raman conversion in a SrWO₄ crystal pumped by multi-Watt MOPA lasers at 1064 nm, *Applied Physics B*, 120 (2015) 731-735.
- [60] A. Grabtchikov, V. Lisinetskii, V. Orlovich, M. Schmitt, R. Maksimenka, W. Kiefer, Multimode pumped continuous-wave solid-state Raman laser, *Optics Letters*, 29 (2004) 2524-2526.
- [61] R.P. Mildren, H.M. Pask, J.A. Piper, High-Efficiency Raman converter generating 1.5 W of red-orange output, in: *Advanced Solid-State Photonics*, Optical Society of America, 2006, pp. MC3.
- [62] C. He, T.H. Chyba, Solid-state barium nitrate Raman laser in the visible region, *Optics Communications*, 135 (1997) 273-278.
- [63] H. Pask, J. Piper, Diode-Pumped LiIO₃ Intracavity Raman Lasers, *IEEE journal of Quantum Electronics*, 36 (2000) 949-955.
- [64] H.M. Pask, Continuous-wave, all-solid-state, intracavity Raman laser, *Optics Letters*, 30 (2005) 2454-2456.
- [65] Y. Chen, High-power diode-pumped actively Q-switched Nd:YVO₄ self-Raman laser: influence of dopant concentration, *Optics Letters*, 29 (2004) 1915-1917.

- [66] Y. Chen, Compact efficient all-solid-state eye-safe laser with self-frequency Raman conversion in a Nd:YVO₄ crystal, *Optics Letters*, 29 (2004) 2172-2174.
- [67] Y. Chen, Efficient subnanosecond diode-pumped passively Q-switched Nd:YVO₄ self-stimulated Raman laser, *Optics Letters*, 29 (2004) 1251-1253.
- [68] X. Chen, X. Zhang, Q. Wang, P. Li, Z. Cong, Diode-pumped actively Q-switched c-cut Nd:YVO₄ self-Raman laser, *Laser Physics Letters*, 6 (2009) 26.
- [69] A.J. Lee, D.J. Spence, J.A. Piper, H.M. Pask, A wavelength-versatile, continuous-wave, self-Raman solid-state laser operating in the visible, *Optics Express*, 18 (2010) 20013-20018.
- [70] Y. Chen, Efficient 1521-nm Nd:GdVO₄ raman laser, *Optics Letters*, 29 (2004) 2632-2634.
- [71] A. Lee, H. Pask, P. Dekker, J. Piper, High efficiency, multi-Watt CW yellow emission from an intracavity-doubled self-Raman laser using Nd:GdVO₄, *Optics Express*, 16 (2008) 21958-21963.
- [72] Y. Lü, X. Zhang, S. Li, J. Xia, W. Cheng, Z. Xiong, All-solid-state cw sodium D² resonance radiation based on intracavity frequency-doubled self-Raman laser operation in double-end diffusion-bonded Nd³⁺:LuVO₄ crystal, *Optics Letters*, 35 (2010) 2964-2966.
- [73] E. Desurvire, H.J. Shaw, Synchronously pumped ring fiber Raman laser, Google Patents, 1988.
- [74] E. Granados, H.M. Pask, D.J. Spence, Synchronously pumped continuous-wave mode-locked yellow Raman laser at 559 nm, *Optics Express*, 17 (2009) 569-574.
- [75] A.R. Chraplyvy, J. Stone, Synchronously pumped D² gas-in-glass fiber Raman laser operating at 1.56 μm , *Optics Letters*, 9 (1984) 241-242.
- [76] A.M. Warrier, J. Lin, H.M. Pask, R.P. Mildren, D.W. Coutts, D.J. Spence, Highly efficient picosecond diamond Raman laser at 1240 and 1485 nm, *Optics Express*, 22 (2014) 3325-3333.
- [77] M. Colles, Ultrashort Pulse Formation in a Short-Pulse-Stimulated Raman Oscillator, *Applied Physics Letters*, 19 (1971) 23-25.
- [78] G.G. Grigoryan, S. Sogomonyan, Synchronously pumped picosecond Raman laser utilizing an LiIO₃ crystal, *Soviet Journal of Quantum Electronics*, 19 (1989) 1402.

- [79] G. Hall, M. Ebrahimzadeh, A. Robertson, G. Malcolm, A. Ferguson, Synchronously pumped optical parametric oscillators using all-solid-state pump lasers, *JOSA B*, 10 (1993) 2168-2179.
- [80] M. Weitz, C. Theobald, R. Wallenstein, J.A. L'huillier, Passively mode-locked picosecond Nd:YVO₄ self-Raman laser, *Applied Physics Letters*, 92 (2008) 1122.
- [81] D.J. Spence, E. Granados, R.P. Mildren, Mode-locked picosecond diamond Raman laser, *Optics Letters*, 35 (2010) 556-558.
- [82] E. Granados, D.J. Spence, R.P. Mildren, Deep ultraviolet diamond Raman laser, *Optics Express*, 19 (2011) 10857-10863.
- [83] M. Murtagh, J. Lin, R.P. Mildren, G. McConnell, D.J. Spence, Efficient diamond Raman laser generating 65 fs pulses, *Optics Express*, 23 (2015) 15504-15513.
- [84] M. Murtagh, J. Lin, R.P. Mildren, D.J. Spence, Ti: sapphire-pumped diamond Raman laser with sub-100-fs pulse duration, *Optics Letters*, 39 (2014) 2975-2978.
- [85] D.J. Spence, E. Granados, H.M. Pask, R.P. Mildren, KGW and diamond picosecond visible Raman lasers, *Advanced Solid-State Photonics*, Optical Society of America, 2010, pp. ATuA20.
- [86] R.P. Mildren, J.E. Butler, J.R. Rabeau, CVD-diamond external cavity Raman laser at 573 nm, *Optics Express*, 16 (2008) 18950-18955.
- [87] E. Granados, H.M. Pask, E. Esposito, G. McConnell, D.J. Spence, Multi-wavelength, all-solid-state, continuous wave mode locked picosecond Raman laser, *Optics Express*, 18 (2010) 5289-5294.

2

Synchronously pumped picosecond Diamond Raman laser

In this chapter we introduce a diamond Raman laser pumped by a CW mode-locked picosecond laser at 1064 nm generating first and second order Stokes wavelengths at 1240 nm and 1485 nm.

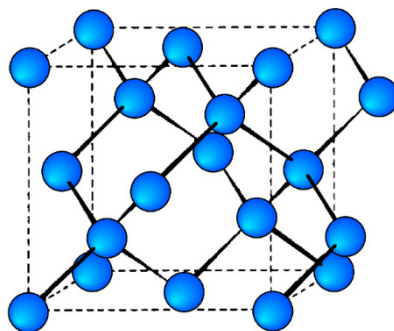


Fig 2.1 Diamond crystalline structure formed by superposition of two fcc structures.

2.1 Structure of diamond and accessing maximum Raman gain

Diamond, which follows the face-centred cubic Bravais lattice structure, may be described as an interpenetration of two face-centred cubic lattices of carbon atoms,

each atom in one lattice being linked to its four nearest neighbours in the other lattice by tetrahedrally directed valence bonds. Incident electromagnetic photons interact with the strong vibrational mode characteristic of diamond caused due to relative motion of the two face-centred cubic lattices along the carbon-carbon bonds, the crystallographic [111] axis. This results in the strongly observed Raman frequency of 1332.3 cm^{-1} . The Raman gain is highest for pump lasers polarised along the [111] or equivalent directions, 33 % higher than for [100] or [110] directions.

Raman himself was fascinated by the different properties exhibited by diamond and had done an exhaustive study. Some of the other initial Raman studies in diamond were done by Ramaswamy (1930) [1], Robertson and Fox (1930) [2], Bhagavantham (1930) [3], Robertson, Fox and Martin (1934) [4] and Nayar (1942) [5]; all of them observing the strong Raman line with frequency shift of 1332 cm^{-1} .

In addition to the strong 1332 cm^{-1} Raman line, many other absorption and emission lines characteristic of impurities and defects in natural diamond samples were observed by the early 20th century investigations. The manufacturing of high purity synthetic diamond crystals has escalated the use of diamonds in lasers. These synthetic crystals are in many ways superior to the naturally occurring ones making them a good candidate for varied industrial applications. One of the common methods of making synthetic diamonds is by chemical vapour deposition (CVD). From

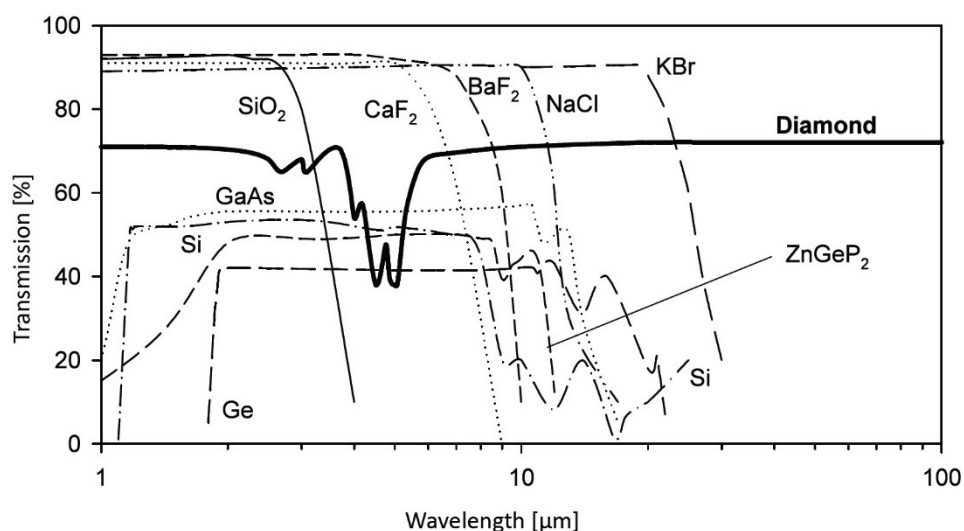


Fig 2.2 Transparency of diamond along with other known crystals. [6]

an optical point of view, diamond has the widest optical transparency band among known crystals as seen from figure 2.2 [6], ranging from 0.2 μm to the terahertz region of the spectrum with a reduced transparency only in the intrinsic absorption bands associated with the direct excitation of multiple phonons. The wide bandgap and lack of first-order infrared absorption makes diamond one of the best materials for frequency conversion particularly in Raman laser construction. The wide transparency range makes it possible for using diamond for extending the wavelength output of existing lasers into UV, visible, infrared and even terahertz sections of the spectrum.

2.2 Diamond Raman lasers

Diamond is also particularly interesting as a Raman material due to its high thermal conductivity and high Raman gain [7]. The Raman gain (g_R) is given by the following formula in terms of the scattering cross-section $d\sigma/d\Omega$:

$$g_R = \frac{16\pi c^2 N}{h\mu_s^2 \omega_s^3 \Gamma} \left(\frac{d\sigma}{d\Omega} \right) \quad (2.1)$$

$$\frac{d\sigma}{d\Omega} = \frac{\mu_s \omega_s^4}{c^4 \mu_p} \frac{h}{4\pi \omega_R} \left(\frac{d\alpha}{dq} \right)^2 \quad (2.2)$$

where N is their number density, μ_p and μ_s are the refractive indices at fundamental and Stokes (ω_s) frequencies, h the Plank's constant, ω_R is the angular frequency of the Raman shift, Γ is the linewidth and $(d\alpha/dq)$ quantifies the change in material polarisability α with oscillator displacement q . With the reduced mass for diamond

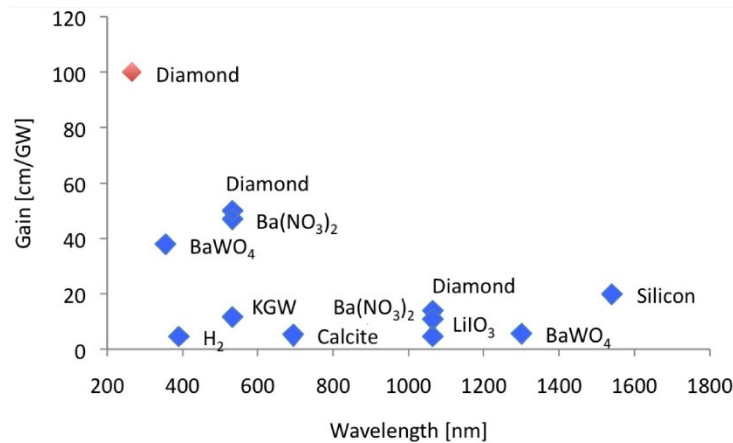


Fig 2.3 Gain of different Raman materials.

being low, we observe a high Raman gain cross section. This can be seen from the comparison of diamond gain with other crystals at different wavelengths given in figure 2.3, taken from the thesis of Eduardo Granados, titled “*Mode locked lasers in the deep ultraviolet and the visible*”.

The first observation of SRS in solids was demonstrated in diamond [8] which employed a single pass experimental setup. In spite of the generally high conversion efficiencies [9], practicality of single or double pass stimulated Raman experiments can be limited due to poor output beam quality and output often spreading over multiple unwanted Stokes and anti-Stokes orders. On the other hand, as discussed in chapter 1, placing a resonant cavity around the Raman gain medium, it reduces the threshold for Raman generation and enables the output spectrum and spatial beam properties to be constrained by the cavity optics [10]. The highest quoted slope efficiency of 75 % was for an external cavity diamond Raman laser [11] in spite of the fact that residual stress-induced birefringence limited the efficiency. In this present work of ours we present still higher slope efficiency (76 %) with an external synchronous ring cavity design generating first-Stokes at 1240 nm and second-Stokes at 1485 nm.

2.3 Mode-locked Picosecond Diamond Raman laser

In this section we report picosecond Raman laser operation by using a synchronous pumping scheme in a ring cavity configuration. This forms the first synchronously pumped ring Raman laser. Using diamond as the Raman medium, we demonstrate several important features of this type of architecture including a selectable method for uni-directional forwards and backwards operation, and efficient second-Stokes generation in a singly resonant cavity. We show that the second-Stokes output is generated in the forward direction through the combined processes of four-wave mixing (FWM) and single-pass SRS, which enables Raman cavity mirror coatings to be simplified. Up to 1.0 W output power was obtained in the eye-safe region at 1485 nm, corresponding to 21 % overall conversion efficiency.

2.3.1 Experimental setup

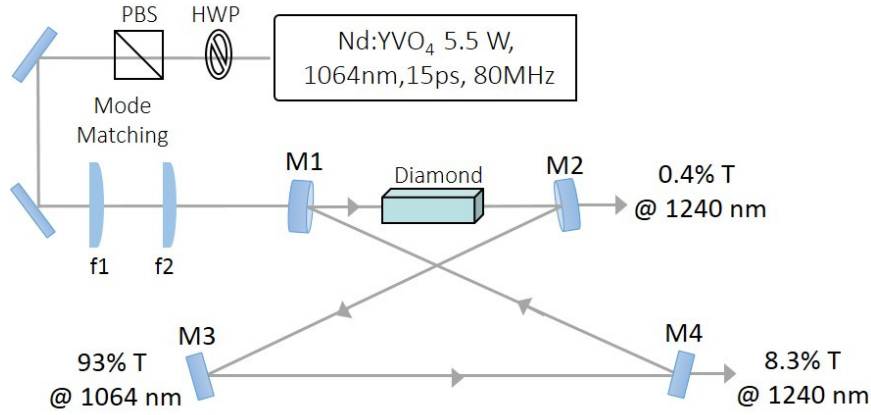


Fig 2.4 Optical schematic of synchronously pumped diamond Raman laser with M₁ as the input coupler and M₂ & M₄ as the output couplers. The pump laser mode is matched with the cavity mode using mode matching lenses f₁ and f₂. The coating specifications for each mirror are summarized in table 2.1.

The experimental setup is shown in figure 2.4. An 8 mm long CVD grown rectangular diamond crystal, with anti-reflective coating at 1240 nm ($R=0.06\%$ per pass for each end-face) was used in this study. In previous works on Raman lasers [12, 13] utilizing diamond crystals, Brewster cut crystals were implemented to compensate cavity astigmatism completely as well as keep the surface reflection losses low. But this causes an increase in the threshold of the laser by a factor of 2.4 owing to the elongation of the cavity waist in the tangential plane. Since we use a rectangular crystal, the folding angle of the cavity at mirrors M₁ and M₂ were kept as small as possible, approximately to 5 degrees, so as to minimise astigmatism. The diamond was oriented such that the pump beam propagated along the [110] axis and was polarised along [111] axis accessing maximum gain from the diamond crystal [14]. The diamond crystal was pumped by a CW mode-locked Nd:YVO₄ laser (*Spectra Physics Vanguard 2000-HM532*) that generated up to 5.5 W average power at 1064 nm with pulse duration of 15 ps, repetition rate of 80 MHz, and beam quality factor M^2 of 1.1.

Table 2.1 Summary of mirror coatings.

Mirror	1064 nm	1240 nm
M1	T= 93 %	R>99.99 %
M2	-	T= 0.4 %
M3	T= 93 %	R>99.99 %
M4	R>99.99 %	T= 8.3 %

A combination of half wave plate (HWP) and polariser beam-splitting cube (PBS) was used to control the laser power incident on the external Raman cavity. This avoided changing of operating characteristics of the pump laser for power variation. Two plano-convex lenses ($f_1 = 500$ mm and $f_2 = 200$ mm separated by 141 cm forming close to telescope armament for beam expansion) were used to focus the pump beam through the input mirror M1 into the centre of the diamond crystal with a focal spot radius $\omega_p = 22$ μm . Position of Lens f_2 was crucial as it decided the mode matching and hence was placed on a translation stage for optimisation.

The diamond cavity was a bow-tie shaped ring cavity composed of two curved mirrors (M1 and M2, ROC = 200 mm) and two flat mirrors (M3 and M4). M1 acted as the input coupler for the external cavity transmitting 93 % of 1064 nm into the Raman cavity. M1 and M3 were highly reflecting for the 1st Stokes wavelength of 1240 nm while M4 acted as the output coupler transmitting 8.3 % of the 1st Stokes along with M2 leaking 0.4 % at 1240 nm. A separation of approximately 205 mm between M1 and M2 produced a resonator TEM₀₀ mode at the centre of the diamond with a similar mode size ($\omega_0 = 20$ μm) to the focused pump.

For optimization of the laser performance, the laser cavity was synchronized with the pump laser. The position Δx of mirror M4 was tuned by using a high precision translation stage. $\Delta x = 0$ is defined as the cavity length measured for lowest threshold of lasing. Negative values correspond to shorter cavities and positive values refer to longer cavities.

2.3.2 The ring cavity design

Our picosecond diamond Raman laser forms the first reported synchronously pumped solid-state ring Raman laser. As the name suggests, in a ring cavity, the pump and the Stokes fields follow a ring trajectory inside the cavity. Most of the reported solid state Raman lasers based on crystals employed standing wave resonator cavity [12, 13, 15, 16]. There are several advantages of using a ring cavity over the standing wave cavity. In a standing-wave cavity, the intracavity Stokes field is predominantly amplified when traveling forward together with the pump pulse along the Raman crystal; the return pass through the crystal can provide a small level of additional gain if the (potentially strongly) depleted pump power is also returned from the end mirror, but at the expense of almost doubled round-trip losses. A ring cavity design thus does not strongly reduce the round-trip Raman gain and can almost halve the round-trip losses compared to a standing-wave cavity. This is especially important in the present case where our cavity losses are mostly accounted for by scattering and surface losses associated with the Raman crystal. The synchronously pumped ring Raman laser will ordinarily provide unidirectional operation without requiring an intracavity optical diode, owing to enhanced temporal overlap of the pump and co-propagating Stokes pulses through the Raman crystal, which is discussed again in detail in section 2.3.4. Finally, an external ring cavity gives no back-reflections to the pump laser system, avoiding the potential need for an isolator between the cavity and the pump laser. These advantages for ring cavities are of course in common with $\chi^{(2)}$ optical parametric oscillators (OPOs), e.g. [17], which share the similarity of being a gain system with no energy storage in the gain media.

2.3.3 Efficient 1240 nm Stokes generation from Diamond

In our picosecond diamond Raman laser while, M4 acted as the output coupler, power leaking out of M2 was also considered for total Stokes power output. Proper synchronization of the cavity with the pump laser resulted in efficient generation of 1240 nm Stokes. Power transfer data for $\Delta x = 0 \mu\text{m}$ is plotted in figure 2.5. We have

achieved an overall conversion efficiency $\eta_o = 59\%$. Far above the SRS threshold (above 3.5 W pump power), the residual pump power started to clamp and the slope efficiency η_s tended towards a limit of 76 %, signalling an efficient laser. The residual pump power leaking out of M3 shows how efficiently the pump power is depleted and transferred to Stokes above the lasing threshold.

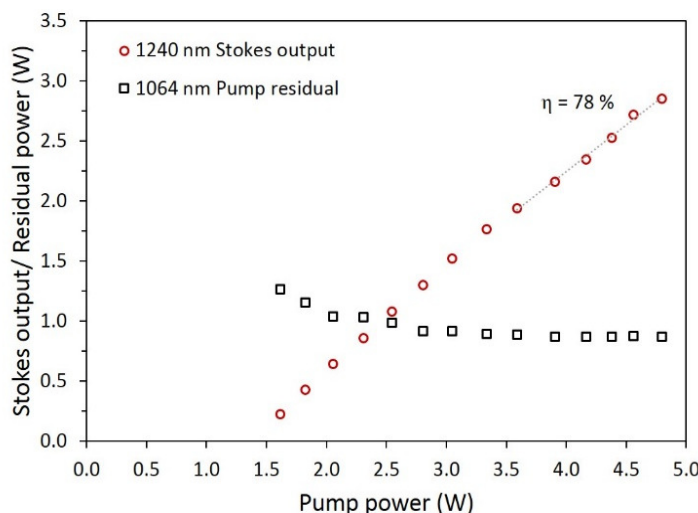


Fig. 2.5 Power transfer measurements of 1240 nm laser output and residual pump power at $\Delta x = 0 \mu\text{m}$.

The cavity length was tuned by translating the mirror M4 on a high precision manual translation stage (Newport) and the lasing threshold was noted for all lengths within the stability range of the laser. The position of minimum threshold was defined as zero ($\Delta x = 0$) and the system was characterised for Stokes output power and pulse duration for all values of Δx . Figure 2.6 depicts these characterisations based on cavity length tuning. The output power and pulse duration were measured at the maximum pump power of 4.8 W. First-Stokes output was obtained within a detuning range of $\Delta x = -400$ to $+45 \mu\text{m}$. The minimum SRS threshold was 1.53 W at $\Delta x = 0 \mu\text{m}$ (by definition), where the maximum output power of 2.75 W at 1240 nm was also obtained. The pulse duration of the first-Stokes output was measured with an autocorrelator (FROG, MesaPhotonics) and the minimum pulse duration of 9 ps at 1240 nm (assuming that the pulses were Gaussian in time) was obtained at $\Delta x = +45 \mu\text{m}$, which is a 60 % reduction from the pump pulse width. The beam quality factor M^2 for the 1240 nm output was measured to be 1.55 at the maximum output power

as seen by figure 2.7 (DataRay Beamscope-p8 scanning slit system). M^2 can be defined as the ratio of the divergence of the actual beam, to that of a theoretical,

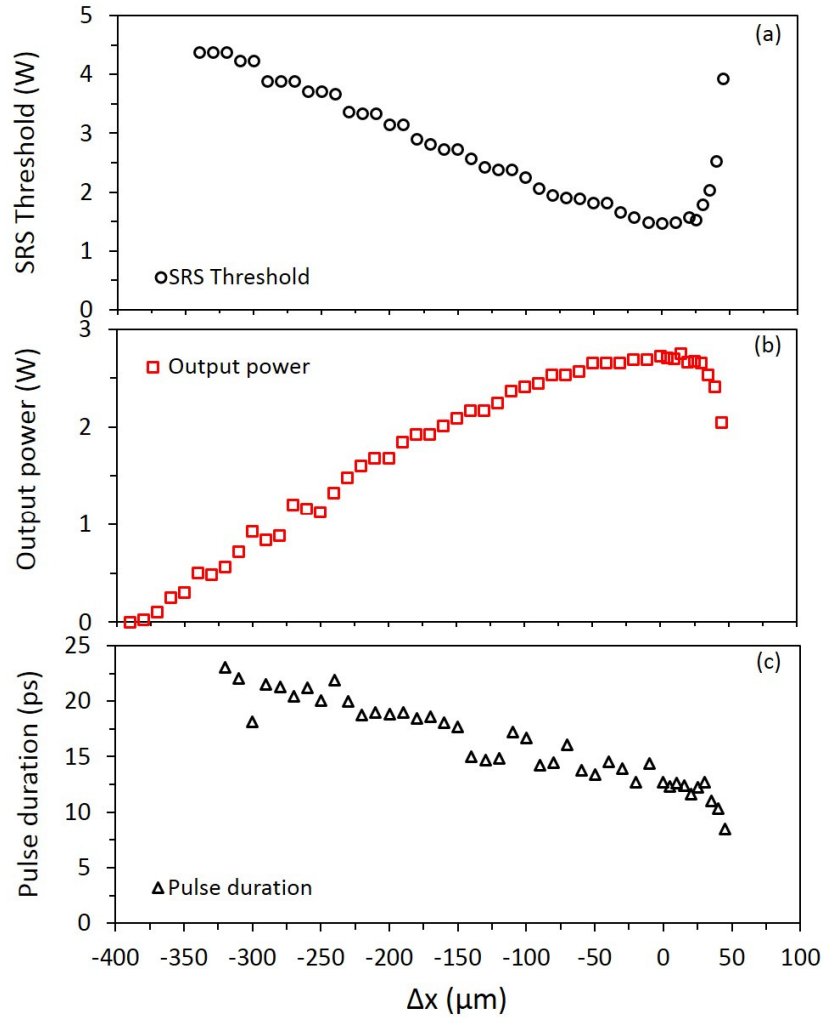


Fig. 2.6 SRS threshold (a) maximum output power (b) and pulse duration (c) of the 1240 nm laser output as a function of cavity length detuning Δx . The maximum output power and pulse duration data were measured for an incident pump power of 4.8 W.

diffraction-limited beam with the same waist diameter. The beamscope has a linear scanning probe with xy slit, light passing through the slit detected by a germanium (800 to 1800 nm) detector. The beamscope oriented at 45° to the optical table using a provided stage allows to generate multiple images of the beam in both the axis over a defined distance which covers the beam waist. The x-axis and y-axis scan can be seen in figure 2.7 along with the M^2 measurement dialog. The correlation between the beam diameters in both x axis and y planes over the scanning range shows the

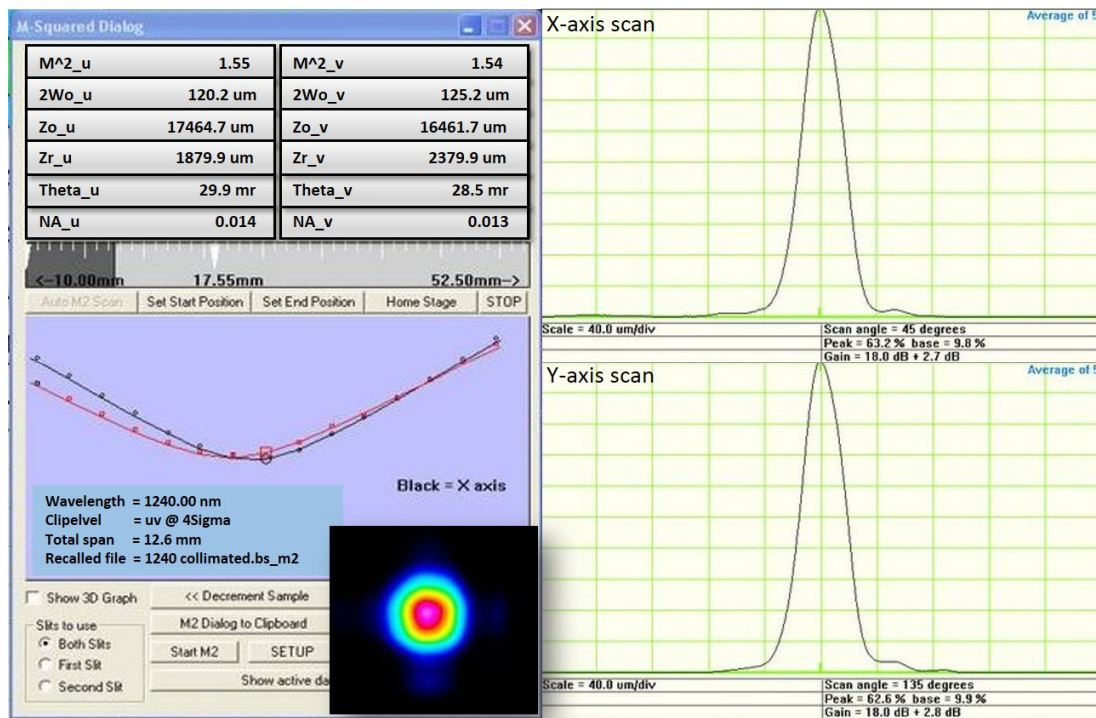


Fig. 2.7 1240 nm Stokes M² scan measurement using beamscope with the beam profile in inset. The X and Y axis scan of the beam profile can also be seen.

quality of our Stokes beam. The beam profile of the Stokes beam can be seen in the inset of figure 2.7.

Synchronous Raman lasers, unlike OPOs, can lase in forwards as well as backwards directions as the underlying Raman gain coefficients in both the directions are equal. We expect a ring cavity design usually to provide unidirectional forward operation owing to the fact that the geometric factors favour forward action due to enhanced temporal overlap between the pump and the co-propagating Stokes pulses through the Raman crystal. The overlap time for a 15 ps pump pulse and any point moving with the Stokes pulse envelope is 64 ps for forwards Stokes pulse (corresponding to the full 8-mm crystal length) but only 7.5 ps for a backwards Stokes pulse (corresponding to the collision time of the pulses). We see then that the geometry will strongly favour forward operation, and the observation of only forward lasing in our experiment is as expected.

The first-Stokes generation in this work seems to be more efficient for both overall and slope efficiencies than the synchronously pumped Raman lasers reported

previously. Compare our values $\eta_o=59\%$, $\eta_s=76\%$ with $\eta_o=25.6\%$, $\eta_s=42\%$ in [15], $\eta_o=29\%$, $\eta_s=41\%$ in [12] and $\eta_o=10.3\%$, $\eta_s=25\%$ in [13]. The improvement is mainly attributed to the ring-cavity configuration for the present work, as well as superior coatings for both the cavity mirrors and Raman crystal used in our system. As discussed before, the ring cavity almost halves the round-trip losses without reducing the round-trip Raman gain.

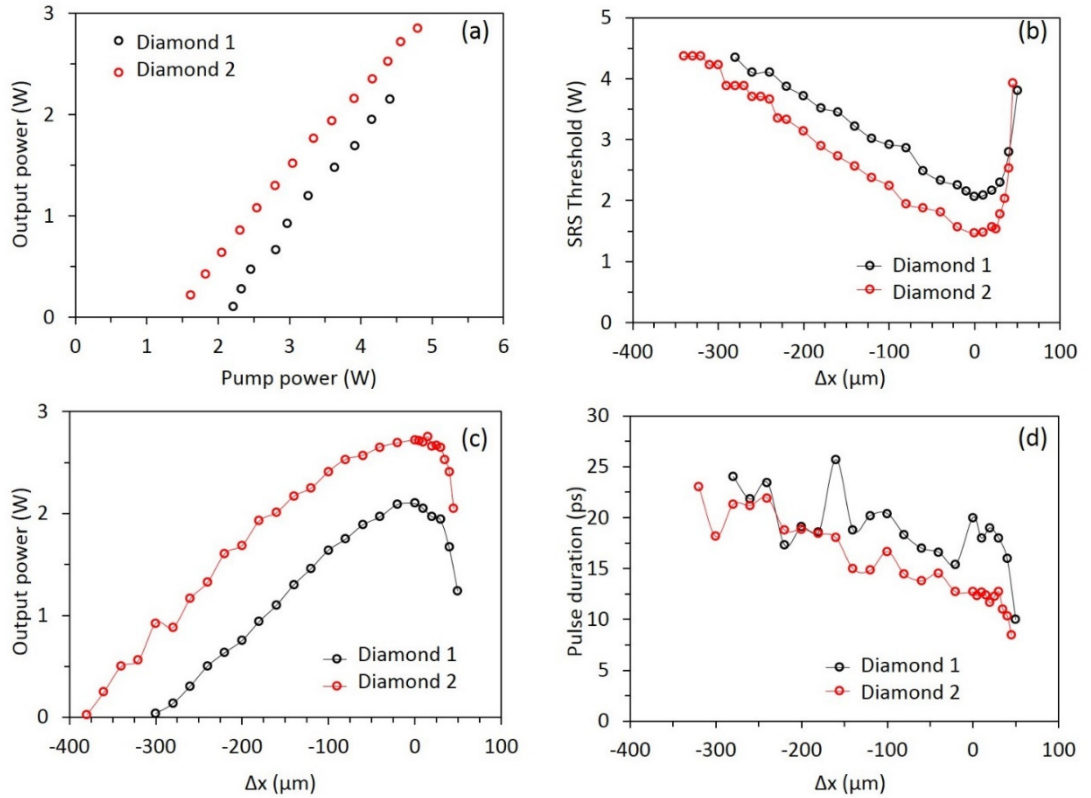


Fig 2.8 (a) Power transfer measurements, (b) SRS threshold, (c) Stokes output power and (d) pulse compression comparison of Diamond 1(0.4 % reflectivity) and Diamond 2 (0.06 % Reflectivity).

The surface reflections at the end faces of the diamond crystal play a crucial role in determining the laser performance by contributing towards intra-cavity losses. To demonstrate this significance, we compare to results using another diamond crystal having same dimensions, but with higher end-face reflectivity of 0.4 % per end-face compared to the 0.06 % reflectivity of our present diamond. The observations are

depicted in figure 2.8. The higher reflectivity diamond (0.4 % reflectivity) is termed as diamond 1 and lower reflectivity one (0.06 % reflectivity) is termed as diamond 2. With the higher reflectivity diamond, reduced output power at 1240 nm of 2.1 W and overall conversion efficiency, η_o of 43 %, was obtained compared to output power of 2.75 W and overall conversion efficiency, η_o of 59 % obtained for our system reported above using diamond 2. The cavity detuning measurements also revealed a better performance by the diamond with lower end-face reflectivity. The one with better AR coating, diamond 2 had lower threshold, greater Stokes output power and shorter pulse duration throughout the stability range as shown above. The reflectivity of the working wavelengths by the end faces of the lasing crystal reduces the gain of the laser by contributing towards resonator losses. To withstand the high intracavity power of ultrafast lasers form another challenge for these antireflective coatings. From a technical point of view these coatings need to mechanical strength which need to be unaffected by environmental conditions such as temperature and humidity inorder to have improved laser stability and lifetime. These antireflective coatings with high damage threshold are also costlier in the market. Thus better the anti-reflectivity of the diamond end faces, higher is the gain achieved.

2.3.4 Pulse compression mechanism in synchronously pumped Raman lasers.

We note that our laser, as well as previous synchronous Raman lasers can have shorter output Stokes pulse duration than the pump pulse duration. The compression mechanism of Stokes pulses in Raman lasers is similar to that of optical parametric oscillators (OPOs) with the group velocity dispersion causing a temporal walk off between the pump and the Stokes pulses, driving the compression. The cavity detuning controls compression of the Stokes pulses as described in this section.

We need to analyse the group velocities of the pulses to understand compression. The walk off time between the pump and the Stokes pulses in a medium of length L , is given by:

$$\text{Walk-off} = L \left(\frac{1}{V_S} - \frac{1}{V_P} \right) \approx 2\pi c L * GVD * \left[\frac{1}{\lambda_P} - \frac{1}{\lambda_S} \right] \quad (2.3)$$

where GVD is the group velocity dispersion, given by:

$$GVD = \frac{d^2 k}{d\omega^2} = \frac{d}{d\omega} \left(\frac{1}{V_g} \right) \quad (2.4)$$

and V_S and V_P are the group velocities of the Stokes and the pump pulses given by:

$$V = \frac{d\omega}{dk} = \frac{c}{n(\omega) + \omega \frac{\partial n}{\partial \omega}} \quad (2.5)$$

where λ_P and λ_S are the pump and Stokes wavelengths, k and ω are the wave-vector and frequencies, n the refractive index as a function of ω . The equation of walk-off in terms of GVD is an approximation because GVD is itself a function of wavelength.

The steady state condition of the synchronously pumped laser requires the relative position of both the Stokes pulse and the pump pulse to be same at the beginning of each round trip. This also needs to be satisfied for all cavity lengths. Any retardation or enhancement of the Stokes pulse with respect to the pump pulse during each round trip due to cavity detuning is compensated by Stokes pulse reshaping. This reshaping can lead to compression. The pulse compression mechanism and dynamics in synchronous pumped Raman lasers was theoretically modelled and studied in [18].

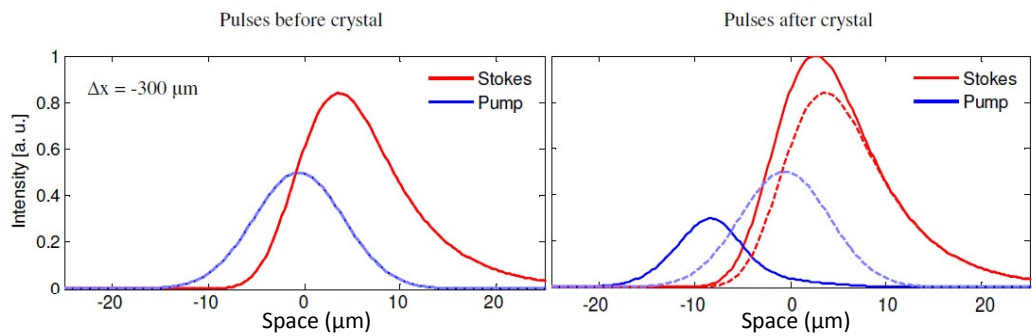


Fig. 2.9 Pulse shapes of pump (blue line) and Stokes (red line) pulses at cavity length of $\Delta x = -300 \mu\text{m}$ before (left) and after (right) of the KGW crystal for shorter cavities [18]. The dashed plots on the right side is produced for comparison.

We discuss the simulations from [18] to illuminate the physics in the present laser. This laser was at 559 nm with a 50 mm long KGW crystal pumped by 10 ps CW mode-locked laser. Figure 2.9 shows in space, the pump and the Stokes pulses before and

after the crystal taken from [18], which shows the pump and Stokes pulse shapes at cavity length of $\Delta x = -300 \mu\text{m}$. The plots are a snapshot in time, with the pulses moving to the right. The blue solid line and the red solid line represents the pump pulse and the Stokes pulse respectively in space. The pump pulse appears to move backwards during the transit through the crystal as the frame we are plotting in is moving at the Stokes group velocity. For shorter cavities, an unamplified Stokes pulse would arrive ahead of the pump pulse after each round-trip, requiring the Stokes pulse to be retarded by gain reshaping. The gain must then amplify the back of the Stokes pulse. The pump pulse then would aligns with the tail of Stokes pulse to effect the reshaping of the pulse. This leads to preferential amplification of the trailing edge of the Stokes pulse.

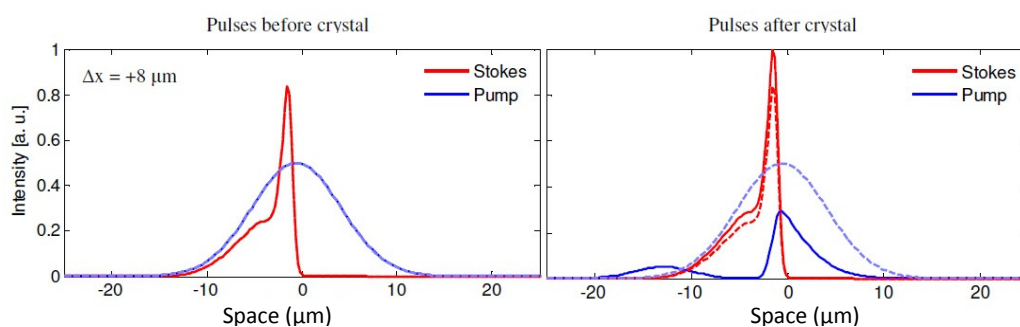


Fig. 2.10 Pulse shapes of pump (blue line) and Stokes (red line) pulses at cavity length of $\Delta x = +8 \mu\text{m}$ before (left) and after (right) of the KGW crystal for longer cavities. [18] The dashed plots on the right side is produced for comparison.

The dynamics of compression are quite different for longer cavities i.e. for $\Delta x > 0$. For longer cavities, the unamplified Stokes pulse would arrive little delayed with respect to the pump pulse. To maintain the steady state, the Stokes pulse needs to be advanced by the gain reshaping. This requires the pump pulse to align itself with the leading edge of the Stokes beam causing preferential amplification of the leading edge of the Stokes pulse. This can be seen in figure 2.10, taken from [18]. For longer cavity lengths, this steepened edge could sweep through the centre of the pump pulse due to group velocity walk-off, extracting the accumulated energy into a short pulse. In our present laser, the minimum pulse compression of 9 ps was observed at $\Delta x = +45 \mu\text{m}$.

Only small positive detuning is tolerated by the system. Raman being a non-instantaneous process, it tends to preferentially amplify the back of the pulses due to build-up of phonons. Larger negative detuning, which requires this preferential amplification of tail, is thus much more tolerated.

While we see this Δx asymmetry in the present laser, we get only weak compression. In our present system, for diamond, the temporal walk-off between the pump and the Stokes during the transit through the crystal was 0.35 ps; which was only 2.3 % of the pump pulse duration. As explained in [18], the important factor for simultaneous efficient operation and pulse compression is a large temporal walk-off between the Stokes and pump pulses during each transit through the crystal allowing the shorter Stokes pulses to walk through and extract energy from the entire pump pulse. Compression is thus more expected for longer crystals with higher dispersion as well as using shorter pump pulses.

The laser described in [18] uses a 50 mm long KGW crystal pumped with a CW mode-locked laser (2 W, 10 ps, 80 MHz) shifting the pump wavelength of 532 nm to 559 nm by the 907 cm^{-1} shift. Whereas our laser presented in this chapter uses a 8 mm long diamond crystal pumped by CW mode-locked laser (5.5 W, 15 ps, 80 MHz) shifting the pump wavelength of 1064 nm to 1240 nm and 1485 nm by the 1333 cm^{-1} shift.

Detailed modelling study of 532 nm diamond picosecond Raman laser appears in [12], where the authors observed less pulse compression. For KGW in [18], the temporal walk off between the pump and the first-Stokes was 4.1 ps per pass whereas for diamond in [12] the walk-off was only 460 fs. Taking a ratio between the walk off and the pump pulse duration, the 25 mm long KGW crystal had 41 % while 8 mm diamond had only 1.6 %. We see that less compression happens when the walk-off is a lesser percentage of the pump pulse duration. For better compression, this percentage can be increased by using a longer crystal or by using a Raman crystal with more dispersion or by using a shorter pump pulse. Although dispersion is similar in diamond and KGW prior experiments by Spence *et. al.* [19] shows that longer crystal with shorter dephasing times and greater group velocity dispersion provides

wavelengths to enable efficient conversion. In 2010, Granados *et al.* [16] reported a cascaded synchronously-pumped CW mode-locked Raman laser. A 50 mm-long KGW crystal was pumped by a frequency-doubled Nd:YVO₄ laser that yielded 7 W at 532 nm, with 28 ps pulses in an 80 MHz pulse train. Both first-Stokes (559 nm) and second-Stokes (589 nm) pulses were resonated in the synchronized standing-wave Raman cavity, resulting in 2.5 W output power for 559 nm and 1.4 W for 589 nm, with 35.7 % and 20 % overall conversion efficiency respectively. The laser system used prisms in the cavity to split wavelengths onto different end mirrors to enable independent control of cavity lengths for the first and second Stokes pulses, required to compensate for their group velocities in the crystal. This work completely demonstrates the nuances involved in developing a cascaded Raman laser.

Table 2.2 Summary of mirror coatings.

Mirror	1064 nm	1240 nm	1485 nm
M1	T= 93 %	R>99.99 %	T= 90 %
M2	-	T= 0.4 %	T= 91 %
M3	T= 93 %	R>99.99 %	T= 90 %
M4 ₁	R>99.99 %	R>99.99 %	R>99.99 %

Efficient generation of 1240 nm from our laser system, as explained in 2.3.2, motivated us to induce cascading by changing the Q of the cavity for 1240 nm. The 8.3 % transmitting output coupler of section 2.3.2 (M4) is replaced by a new HR output coupler (named as M4₁), which is HR at 1064 nm as well as 1240 nm. Table 2.2 gives the summary of coatings of all the mirrors used in this setup. This radically decreased the loss of the 1240 nm field, with the aim to increase its intracavity intensity to induce cascading to 1485 nm. Mirror M2 becomes the output coupler in this arrangement with 0.4 % output coupling for first Stokes at 1240 nm and 91 % output coupling for second Stokes at 1485 nm. The change of M4 to M4₁ presented us with new exciting observations. Efficient second Stokes generation at 1485 nm was achieved from the forwards 1240 nm field. Backwards generation of first-Stokes at 1240 nm was also now observed for some Δx . Figure 2.11 shows the cavity with new output coupler with transmittance percentages.

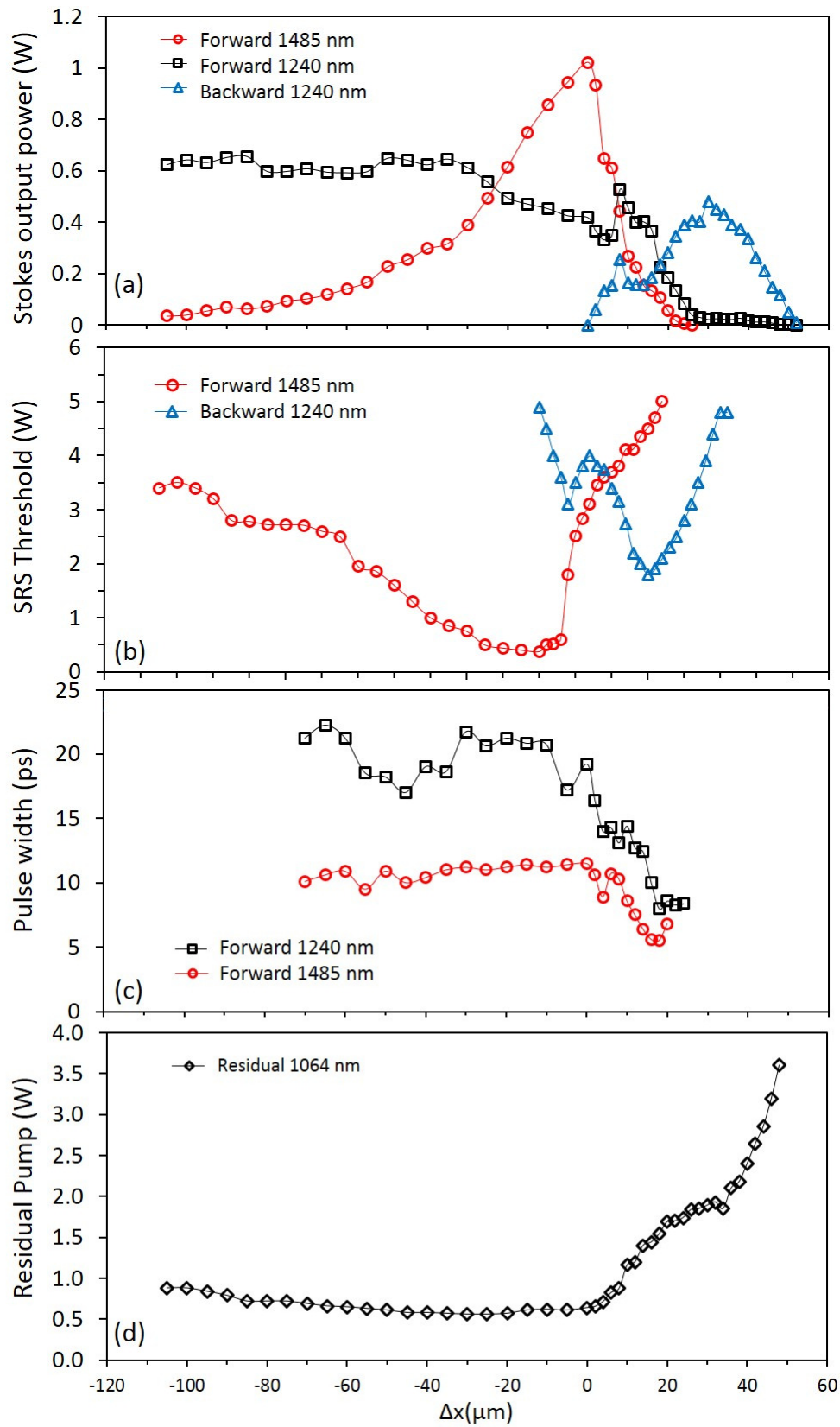


Fig. 2.12 (a) Output power, (b) threshold and (c) pulse duration of the laser output as a function of cavity length detuning Δx . The output power, residual power and pulse duration were measured for an incidence pump power of 4.8 W.

The laser performance of our picosecond diamond Raman laser with this new high-Q first Stokes cavity, as a function of Δx is summarized in figure 2.12. The first Stokes can also be seen to be generated forwards over a longer range (from $-105\ \mu\text{m}$ to $+50\ \mu\text{m}$) compared to second-Stokes $1485\ \text{nm}$ operating in a narrower Δx region (from $-105\ \mu\text{m}$ to $+22\ \mu\text{m}$). The first Stokes was also generated in the backward direction over a small positive Δx region (0 to $50\ \mu\text{m}$). A maximum of $1.02\ \text{W}$ was observed for second Stokes ($1485\ \text{nm}$) at $\Delta x = 0\ \mu\text{m}$ while forward first Stokes and backward first Stokes generated a maximum of $0.65\ \text{W}$ (at $\Delta x = -85\ \mu\text{m}$) and $0.49\ \text{W}$ (at $\Delta x = +30\ \mu\text{m}$) respectively. The $1240\ \text{nm}$ first Stokes power generated was lesser compared to the section 2.3.2, where we observed only forward first Stokes generation as expected when cascading to second Stokes as well as with competition from backward Stokes. The maximum $1485\ \text{nm}$ out power generated was $1.0\ \text{W}$ at $\Delta x = 0\ \mu\text{m}$ with $4.8\ \text{W}$ pump power, corresponding to $\sim 21\%$ overall conversion efficiency. This shows an efficient generation of $1485\ \text{nm}$ by parametric coupling of Raman components.

Figure 2.12 (b) gives the threshold variation of forward and backward first Stokes generation. The minimum threshold observed for forward first Stokes generation was $0.37\ \text{W}$ which is less than the low-q cavity case of $1.5\ \text{W}$ in section 2.3.2.

Figure 2.12 (c) shows the pulse duration measurements of forward first Stokes as well as second Stokes. The $1485\ \text{nm}$ output pulse duration was around $10\ \text{ps}$ for most of the negative Δx cavity detuning range and dropped steeply for positive detuning. The shortest pulse duration was $6\ \text{ps}$ at $\Delta x = +20\ \mu\text{m}$ with a measured beam quality factor M^2 of ~ 2.2 at the maximum output power. The first Stokes of $1240\ \text{nm}$ also had the shortest pulse duration of $8\ \text{ps}$ at $\Delta x = +20\ \mu\text{m}$, compared to $9\ \text{ps}$ observed in section 2.3.2.

The pump depletion study was also carried out as seen in figure 2.12 (d) which shows the residual pump power leaking out through cavity mirror M3. A high level of pump depletion can be observed in the region where efficient second Stokes was generated. For positive detuning regions, only backward generation of first Stokes

was occurring as seen in figure 2.12 (a). This is relatively inefficient and the pump is not well depleted.

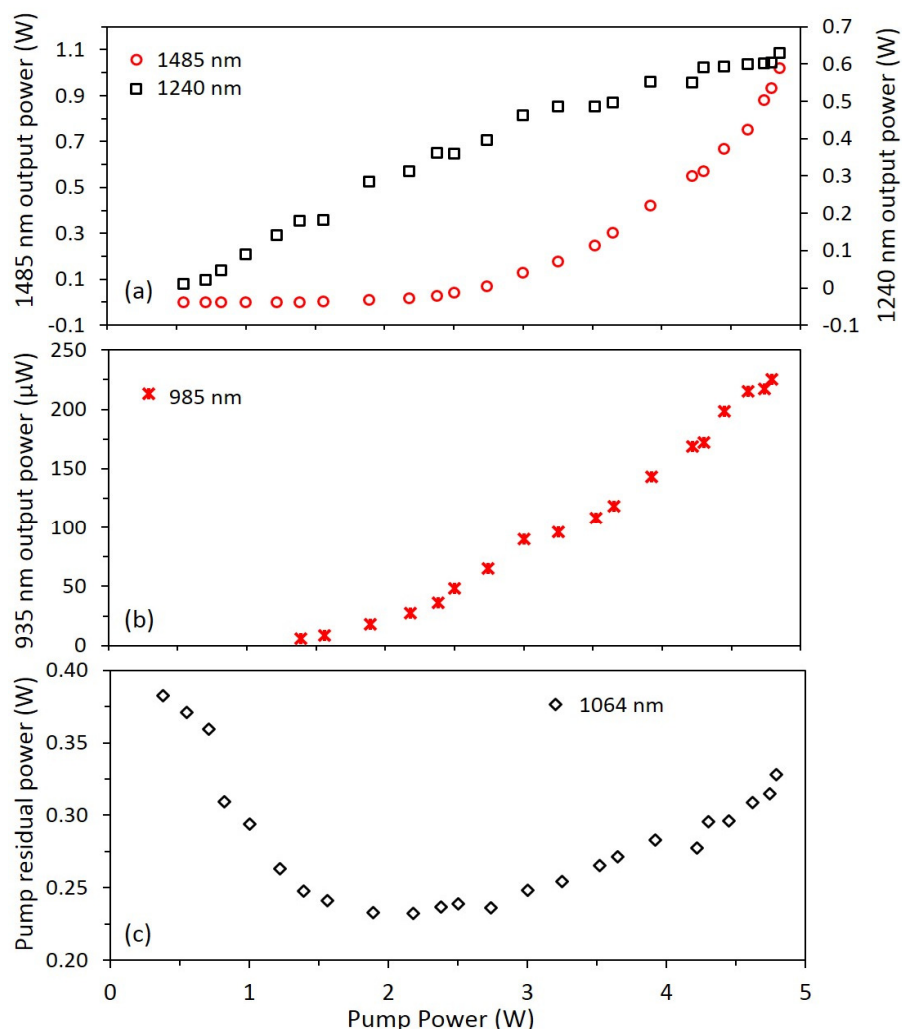


Fig. 2.13 (a) Second-Stokes (1485 nm) output power and first-Stokes (1240 nm) leaking power, (b) Anti-Stokes (935 nm) output power and (c) Residual fundamental (1064 nm) power as a function of pump power at $\Delta x = 0 \mu\text{m}$.

We also observed a small collinear output at 935 nm corresponding to the anti-Stokes wavelength. To further investigate the behaviour of this laser, we measured the second-Stokes, anti-Stokes and first-Stokes power coupled from M2 as well as residual pump power as a function of pump power. Figure 2.13 (a) shows the variation of first Stokes (forward) and second-Stokes power with respect to the pump power. The small collinear 935 nm output is plotted in figure 2.13 (b). The anti-Stokes

power below 1.4 W pump power was not measured owing to the limited sensitivity of the power meter used in the experiment. Efficient lasing action was confirmed by the pump power depletion measurements as seen by residual pump values for all pump power in figure 2.13 (c).

Second-Stokes was generated efficiently, despite the fact that the second-Stokes wavelength was extremely weakly resonated. The cavity mirror coatings allowed only 0.02 % of second-Stokes power at the exit of the crystal to circulate for the next round trip. Also the generated second Stokes at 1485 nm demonstrated a thresholdless behaviour which is inconsistent with both resonated second Stokes generation as well as single pass second Stokes generation indicating the absence of normal SRS cascading mechanism acting in the system. This thresholdless behaviour is shown in figure 2.14.

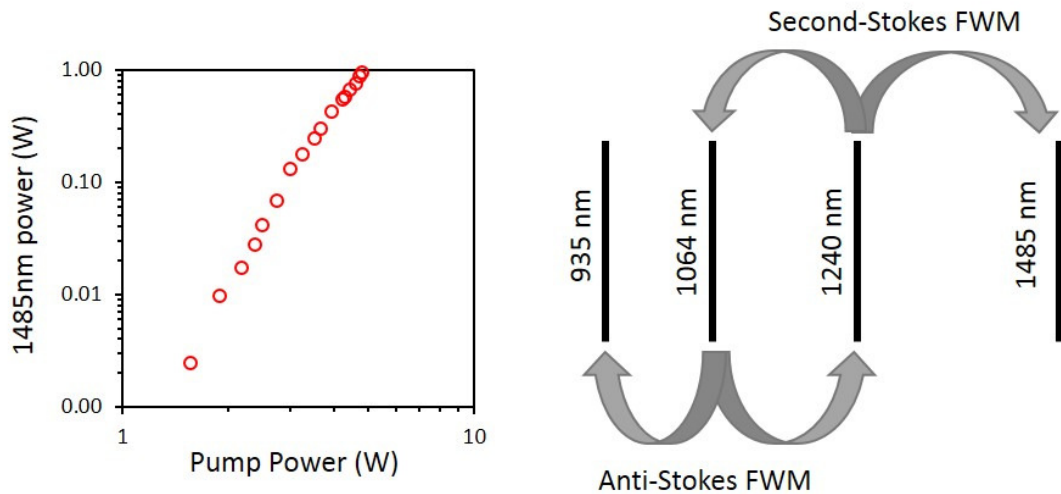


Fig. 2.14 Left: Second Stokes output power vs. pump power on a log-log plot showing threshold-less behaviour of second-Stokes generation. Right: Generation of anti-Stokes as well as second Stokes by FWM.

The efficient second Stokes generation was found to be due to parametric generation of second Stokes by Four Wave Mixing (FWM) seeding the single pass generation of second-Stokes. In this process second-Stokes is generated parametrically when two Stokes photons create a second-Stokes and a pump photon. The presence of anti-Stokes generation at 935 nm points to a different parametric four-wave-mixing, where two pump photons create a Stokes and anti-Stokes pair. With a strong pump

field, and a collinear resonated Stokes field, these processes can be strong. This process is depicted schematically in figure 2.14-right where the anti-Stokes as well as second Stokes generation is shown.

Figure 2.14 shows schematically the different FWM processes happening in the system. FWM for generating second-Stokes and anti-Stokes can be described by following equations [31].

$$P_{SS} = \frac{g_R^2 \omega_{SS}^2 P_L P_S^2}{A^2 \omega_S^2 \Delta k_{SS}^2} \sin^2 \left(\frac{z \Delta k_{SS}}{2} \right) \quad (2.6)$$

$$P_{AS} = \frac{g_R^2 \omega_{AS}^2 P_S P_L^2}{A^2 \omega_L^2 \Delta k_{AS}^2} \sin^2 \left(\frac{z \Delta k_{AS}}{2} \right) \quad (2.7)$$

where P_L, P_S, P_{SS}, P_{AS} are the powers while $\omega_L, \omega_S, \omega_{SS}, \omega_{AS}$ are the angular frequencies of the fundamental, first Stokes, second Stokes and anti Stokes respectively; A is the beam area which is assumed equal for all four optical fields; g_R is Raman gain coefficient at fundamental wavelength; z is the effective interaction length; Δk_{SS} and Δk_{AS} are the phase mismatch of the FWM for second-Stokes and anti-Stokes respectively.

For exact phase matching condition, i.e the phase mismatch is zero, the second Stokes and the anti Stokes have a quadratic dependence on the interaction length. But due to dispersion of diamond in the infrared region, in the collinear geometry the parametric process is not phase matched. For anti-Stokes the wave vector mismatch can be written $\Delta k_{AS} = 2k_P - k_S - k_{AS}$ where k_P, k_S, k_{AS} are the wave vectors of the pump, Stokes, and anti-Stokes fields. For diamond, with a pump wavelength of 1064 nm we calculate, $k_{AS} = 8065 \text{ m}^{-1}$ [32], corresponding to a dephasing length of 390 μm . Along the 8-mm-long diamond crystal then, the anti-Stokes will be created and back-converted many times as the nonlinear polarisation at the anti-Stokes frequency comes in and out of phase with the propagating anti-Stokes wave; the anti-Stokes output that we see is a result of generation over just part of a dephasing length at the exit of the crystal.

Parametric generation of the second Stokes also occurs via phase-mismatched FWM with two Stokes photons generating a pump and second Stokes photon, where the

second-Stokes wave vector mismatch $\Delta k_{SS} = 2k_S - k_P - k_{SS}$ is 6857 m^{-1} in our case. Second-Stokes generation should be much stronger than for anti-Stokes: the former is proportional to $P_P P_S^2$, whereas the latter is proportional to $P_S P_P^2$ where P_P and P_S are the pump and Stokes intracavity power, and in this laser the cavity-enhanced Stokes field is substantially the stronger of the two except very close to threshold.

In contrast to the anti-Stokes wave, the second-Stokes wave will of course also see SRS gain pumped by the Stokes field. The FWM described by equations (2.6) & (2.7) gives a sine-like creation and destruction of second Stokes and anti Stokes when propagating along the diamond crystal. If the second-Stokes field were generated merely via FWM, the crystal length must be carefully selected to ensure that the exiting face of the crystal is located at the peak of the interference pattern. When SRS is included in the consideration, the second-Stokes will amplify according to equation (2.8) and break the symmetry of creation and destruction to generate a strong second-Stokes signal.

$$\frac{dP_{SS}}{dz} = g_R \frac{\omega_{SS}}{\omega_S} P_S P_{SS} \quad (2.8)$$

In general, single-pass SRS initiates from the second-Stokes spontaneous Raman noise induced by the incident first-Stokes field. However, FWM due to parametric coupling provides a much stronger initial seed which can therefore help build up the second-Stokes field much more rapidly. Thus the parametric generation of second-Stokes seeds the SRS process, generating the second-Stokes field in a single-pass; the weakly-resonated second-Stokes field is negligible in this case. This interpretation is supported by the threshold-less behaviour of the second-Stokes, seen clearly in figure 2.14, and in the anti-Stokes of figure 2.13.

This method to generate second-Stokes is much simpler than Granado's method [16] of resonating the second-Stokes as it avoids splitting of resonators to control the cavity lengths of first and second-Stokes separately. It is still not clear whether this method would work easily in the visible region. One would have expected to see single pass second-Stokes generation when the second-Stokes cavity was misaligned.

FWM seems to be best in the infrared region and even better for longer wavelengths. As seen in figure 2.15, the shorter wavelengths experience higher dispersion and hence have higher wave vector mismatch (Δk_{ss}) which would result in weaker FWM seeding.

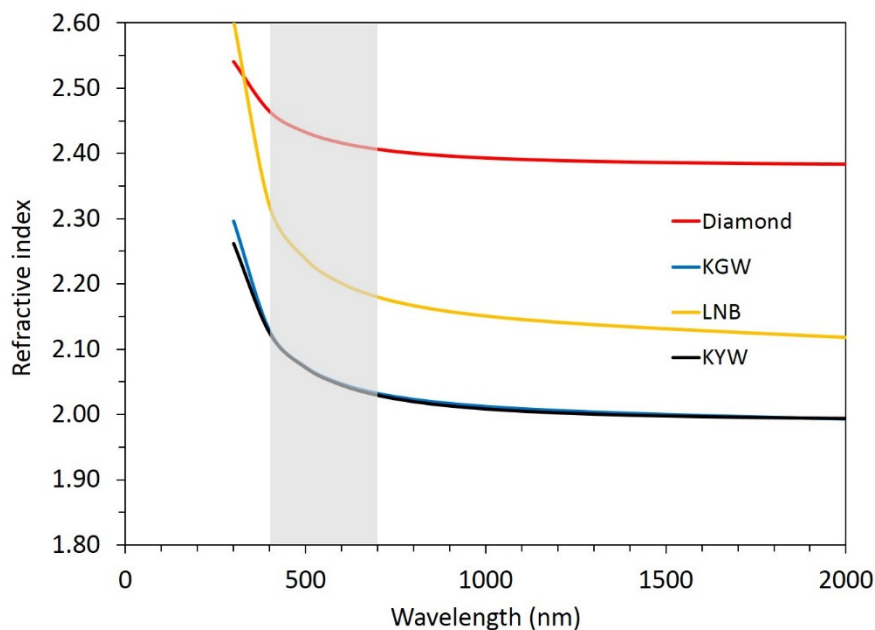


Fig. 2.15 Refractive indices of Potassium Gadolinium Tungstate (KGW), Potassium Yttrium Tungstate (KYW), Lithium niobate (LNB) and Diamond over broad range of wavelengths with the visible range represented by grey shade.

While standard cascaded generation is easily achievable in the visible region, cascaded generation of higher order Stokes wavelengths in the infrared region can be more difficult because of the considerable decrease in the SRS gain coefficient with increasing wavelength [33] as well as is limited by the radiation damage threshold of the crystal [34]. But since the crystals have lesser dispersion of refractive index at higher wavelengths, parametric coupling of SRS components can generate a stronger seed for higher order Stokes generation in the infrared region compared to the spontaneous Raman noise which usually seeds the cascading process. Thus FWM seeding single-pass generation helps in efficient higher-Stokes generation in the infrared region and forms an excellent route for accessing multiple wavelengths from a single source.

Parametric coupling of SRS components have been studied and theoretically modelled in single pass Raman generators where they observed reduced generation threshold for cascaded Stokes generation by parametric coupling compared to their expected generation by the simple cascaded SRS mechanism [29, 34-37].

T. T. Basiev *et. al.* observed multiple Stokes generation with greatly differing thresholds in $\text{Ba}(\text{NO}_3)_2$ [38] while Voronina *et. al.* could observe multiple Stokes generation in BaWO_4 crystal [39] with quite similar lasing thresholds, which was attributed to parametric coupling of SRS components in the less dispersive BaWO_4 crystal: $\text{Ba}(\text{NO}_3)_2$ is known to have higher dispersion of refractive index than BaWO_4 in the infrared region [40]. This shows the importance of dispersion of refractive index in the reduction of threshold for multiple Stokes generation.

Owing to efficient single pass generation, it becomes easier to design the cavity mirror coatings which are not required to have reflectivity at the second-Stokes wavelength, nor is there a requirement for intracavity dispersion management as was used in [16]. Thus the combination of FWM and single-pass SRS for generating the second-Stokes output represents a practically convenient method for efficient generation with regard to cavity design considerations.

2.3.6 Backwards generation of first Stokes (1240 nm)

Unlike the low-Q cavity of section 2.3.3, with M4 output coupler with unidirectional first-Stokes intracavity fields, the high-Q cavity of section 2.3.5, with mirror M4₁ could lase in the forward as well as the backward direction. In contrast to OPOs, synchronously pumped Raman laser cavities can lase in forward as well as backward directions as the underlying Raman gain coefficient is the same for forwards- and backwards-SRS.

To compare forward and backward gain, we must consider the overlap times of co-propagating and counter-propagating pump and Stokes fields. For the 8 mm diamond crystal that we use in our experiment, the time of overlap between a point on the Stokes pulse and the pump pulse for the forward and the backward Stokes cases can be found by the following equations.

$$\text{Forward Stokes} \quad \text{Overlap time} = \frac{\tau_P}{1 - \frac{V_{gP}}{V_{gS}}} \text{ or } \frac{L}{V_{gS}} \quad (\text{Whichever is smaller}) \quad (2.9)$$

$$\text{Backward Stokes} \quad \text{Overlap time} = \frac{\tau_P}{1 + \frac{V_{gS}}{V_{gP}}} \text{ or } \frac{L}{V_{gS}} \quad (\text{Whichever is smaller}) \quad (2.10)$$

where τ_P is the pump pulse duration, V_{gP} and V_{gS} are the pump and the Stokes group velocities in the diamond crystal where the overlap time must be less-than or equal-to the crystal transit time, L/V_{gS} . For a 15 ps pump pulse and group velocities for 1064 nm as 1.2428776×10^8 m/sec and for 1240 nm as 1.2474869×10^8 m/sec, the above calculations show that any point moving with the Stokes pulse envelope has an overlap of 64 ps in the forward Stokes case and 7.5 ps in the backward Stokes pulse case in an 8 mm crystal. This means that the geometry will strongly favour forwards operation unless the crystal length is significantly shortened. Contrary to this theoretical prediction we do observe backward Stokes generation. This forms the discussion of this section.

With the high-Q cavity used for second-Stokes operation, backwards propagating first-Stokes output was also obtained for small positive length detunings of $\Delta x = 0$ to $+55 \mu\text{m}$, measured at output coupler M2. The output power and threshold for the backward first-Stokes output as a function of Δx are characterized in figure 2.12 (a) and 2.12 (b) respectively. The maximum output power for the backward 1240 nm was 0.45 W at $\Delta x = +27 \mu\text{m}$. The pulse duration along the whole operating region was greater than 30 ps (measured by FROG, MesaPhotonics), limited by the scanning range of the autocorrelator, much longer than that for the forward first-Stokes.

Observation of backwards operation given that the geometric factors should favour forward operation by a large factor is intriguing. The answer lies in the complexities of the synchronization effects, acting differently for forwards and backwards operation depending on Δx as explained in section 2.3.4.

In general, the forward SRS operates best for cavity lengths that are matched, or a little shorter than the pump laser (negative detuning). For negative detunings, the steady-state Stokes pulse must be preferentially amplified in its tail to reshape the pulse to cause an effective delay, counteracting the fact that it is advanced on each

round trip owing to the cavity length mismatch. Preferential amplification of the tail is consistent with transient Raman scattering [41], and so relatively large negative detuning can be tolerated [18]. Efficient operation of the forward-Stokes leads to strong depletion of the pump field as shown in figure 2.12 (d) and figure 2.13 (c), and so backward-Stokes operation does not reach its threshold.

On the other hand, for positive detunings, the steady-state forward Stokes pulse must be preferentially amplified in its leading edge to reshape the pulse to cause an effective advancement, counteracting the fact that it is retarded on each round trip owing to the cavity length mismatch. Preferential amplification of the leading edge of the Stokes pulse which is not easily achieved, as the phonon build-up would not have reached its zenith during the leading half of the Stokes pulse. This prevents forward-Stokes laser output for significant positive detuning. In this regime, however, the suppressed forward operation appears to enable backward-Stokes operation to achieve threshold.

Pulse reshaping dynamics are quite different for backward Stokes. In the case of backward Raman Stokes, always the leading edge collides first with the pump pulse. This can be understood by a simple imagination of pump and counter propagating backward Stokes pulses in the crystal. With the leading edge colliding first with the pump pulse, as it depletes the pump, the leading edge would see higher gain compared to the trailing edge and hence preferential amplification of the leading edge would result. Conversely the non-instantaneous Raman process would tend to favour amplification of the trailing edge. The outcome of these conflicting mechanisms seems to be that backward Stokes generation does permit more positive detuning than the forward Stokes. Thus for longer cavities the forward Stokes generation is more strongly suppressed allowing backward Stokes generation to take place despite its geometric disadvantage. This also explains why shorter stability range was observed for backward generated stokes (50 μm) compared to forward generated stokes fields (110 μm) as backward generation simply cannot compete in the negative detuning region.

There must also be a mechanism for altering the reshaping of the backward pulse depending on the particular Δx chosen and so the precise reshaping required. We suggest that the cavity length detuning determines where the pump and the backward Stokes pulses cross each other within the crystal. Depending upon the point of crossing between the pump and the backward Stokes pulses inside the crystal, the preferential amplification of leading or trailing edge of the backward Stokes pulse occurs. For example, see figure 2.16 (a), when the backward Stokes pulse encounters the pump beam at the beginning of the crystal, the leading edge would see low Raman gain as the leading edge could leave the crystal by the time the peak of the pump pulse arrives, suppressing gain for the leading edge. Figure 2.16 (b) shows the other extreme case when the crossing happens near the back (or exit facet) of the crystal. Here the peak of the pump pulse can exit the crystal before the tail of the Stokes pulse arrives, suppressing gain for the trailing edge.



Figure 2.16 Backward Stokes pulses crossing the pump pulses at different portion of the Raman crystal.

2.3.7 Isolating forward and backward generated Stokes fields.

The pulse forming dynamics for the colliding pump and backwards Stokes fields clearly permits operation for larger positive detuning. The next step was to examine operation in this regime and investigate ways by which backwards operation can be made to generate in preference to forward.

The motivation for further exploring backward operation was because we felt that very short Stokes pulses might be generated. Strong compression in backward SRS amplifiers is well studied in gases, with order-of-magnitude or more compressions

possible [42], and potential compression down to pulse durations as short as $0.17\tau_p$ [43] corresponding to 720 fs for diamond, and 38 fs for LiNbO_3 [44].

Intensity enhancement in backward Raman scattering was first observed by Maier *et.al.* where a q-switched ruby laser of peak power 1.4 MW was focused on to a cell of carbon disulphide, resulting in backward Stokes with reduced pulse width of less than 30 ps from the pump laser of 12 ns [45]. Theoretical modelling along with further experiments was published by the same authors in 1969. Glass presented the first design of backward Raman laser systems for practical application [46]. A schematic representation of pulse compression by backward SRS taken from [42] is shown below where a pump pulse of length τ_p passes through Raman medium (travelling left) with a short counter propagating Stokes pulse (travelling right). With the Stokes pulses depleting the pump, a short Stokes pulse can efficiently extract the power from a long pump pulse as seen in figure 2.17. We expected to observe this kind of a compression mechanism happening in our system.

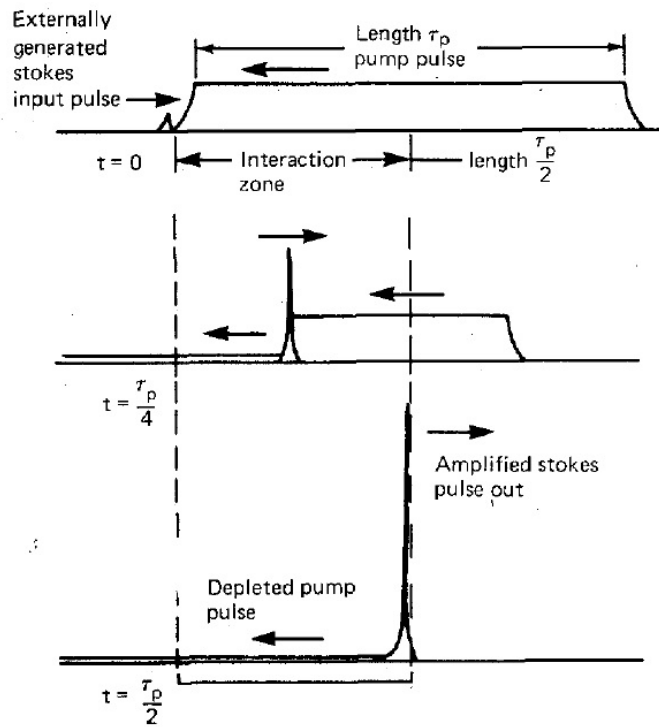


Fig. 2.17 Mechanism of pulse compression by backward SRS Taken from [44].

The Raman cavity was forced to operate in the pure backward direction by introducing an intracavity optical isolator to prevent the forward Stokes field from oscillating. An optical isolator, or optical diode, is an optical component which allows the transmission of light in only one direction. It is mostly employed in situations where back reflections are needed to be prevented from entering back into optical oscillators like laser cavities. A polarisation dependant isolator or a Faraday isolator comprises three major parts viz. input polariser (vertical polarisation), a Faraday rotator and an output polariser called as analyser (polarised at 45 degrees) as schematically represented in figure 2.18 (a). The Faraday rotator forms the element in the optical isolator which administers a non-reciprocal polarisation rotation while maintaining linear polarisation for the entering linearly polarised light.

Faraday rotation is a magneto-optical phenomenon involving the interaction of light with magnetic field in a material. Consider a linearly polarised light passed through a medium subjected to a magnetic field, the direction of the polarisation is continuously changed during the passage by an angle given by the relation, $\beta = \nu B d$, where ν the Verdet constant of the medium (which has an inverse relationship with the wavelength), B is the magnetic flux density in the direction of propagation and d is the length of the medium.

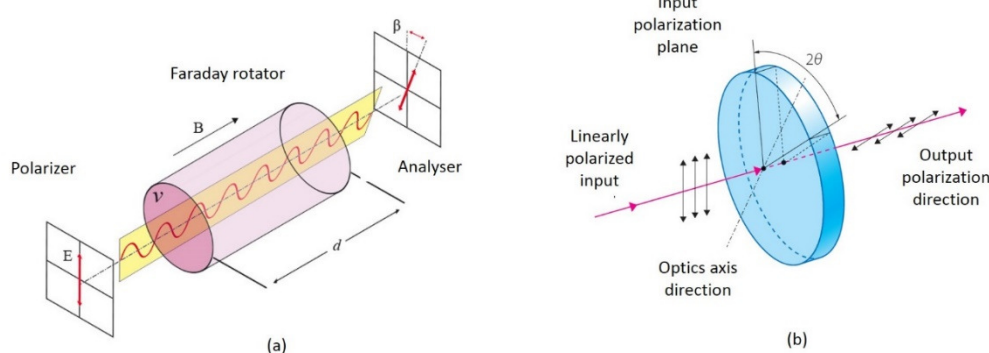


Fig. 2.18 (a) A Faraday material which rotates the polarization of an incoming plane polarized light by an angle β . (b) Half wave plate which flips the polarization of a passing linearly polarized light by twice the angle between the plane of polarization and the optics axis.

The direction of rotation of the polarisation is dependent on the direction of magnetic field and the sign of the Verdet constant. The important aspect of the rotation is that it is non-reciprocal. Polarisation rotation in the Faraday rotator is direction depended which is due to the reversal of helicity on change of direction of propagation with magnetic field. In other words, if a linearly polarised light is passed through a Faraday rotator and allowed to travel back after reflection from a mirror, the rotation changes at the two passes add up instead of cancelling each other, unlike what happens in an optically active medium (e.g. sugar solution) where reflection of the beam back through the medium undoes the optical rotation underwent in the forward pass. This results in the optical diode action of an isolator. For our laser system we used a combination of a Faraday rotator, half wave plate (HWP) and a Brewster plate, in order, to present higher losses for forward operation compared to backward operation. A half wave plate (HWP) flips the direction of a linearly polarised light across its optics axis direction, by an angle equal to twice the angle between the polarisation and the optics axis direction as shown in figure 2.18 (b). A HWP can be used to cancel the rotation β in one propagation direction, but it will add to the rotation in the other propagation direction. With the addition of a polariser we achieve different losses for two directions with the difference maximized for $\beta = 45^\circ$ and $2\theta = 45^\circ$.

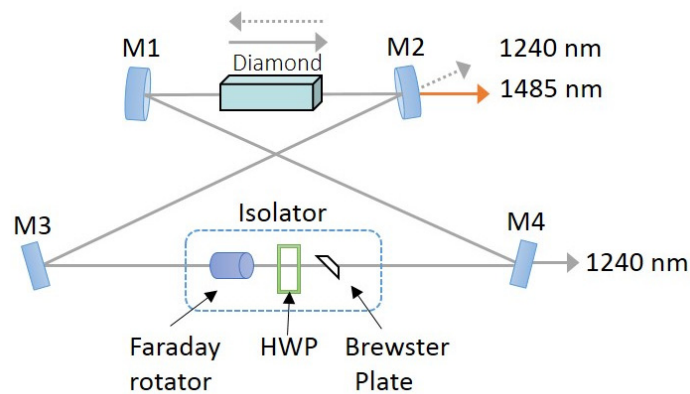


Fig. 2.19 Experimental schematic with inclusion of isolator in the cavity.

Figure 2.19 gives schematic of the isolator in the cavity of the laser. Since the pump beam was horizontally polarised along the crystallographic [111] direction, the

generated Stokes was also expected to be along the same direction. But due to stress-induced birefringence [47], depending upon the positioning of the diamond crystal, the Stokes polarisation was observed to change. Since the working of isolator completely depend on the polarisation of the Stokes, the diamond was adjusted slightly in its position by translating to find a less stressed portion so that we obtain horizontally polarised Stokes light.

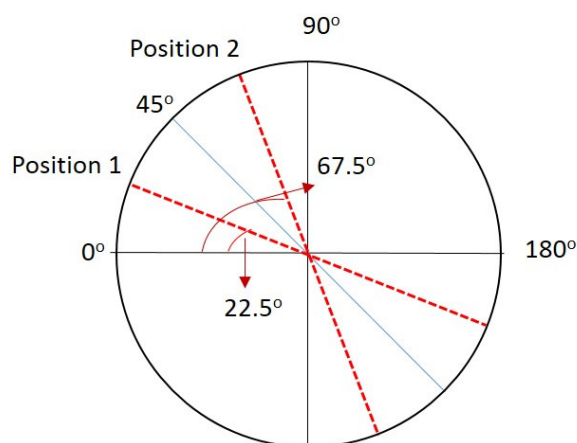


Fig. 2.20 Orientations of HWP for pure forward Stokes generation (position1) and pure backward Stokes generation (position2).

Using a rotator with $\beta = 45^\circ$, the fast axis of the HWP needed to be oriented in two angles with respect to the horizontal plane to obtain pure forward Stokes and pure backward Stokes generation. These two positions are depicted in figure 2.20, where the figure is drawn as seen by forward propagating fields. The fast axis of the HWP needed to be oriented at position 1 inhibit backwards operation to achieve pure forward Stokes generation, and at position 2 to inhibit backwards operation to achieve pure backward Stokes generation.

For pure forward operation, the fast axis of the HWP is rotated to position 1 which is 22.5° with the horizontal. The horizontally polarised forward Stokes enters the isolator through Faraday rotator which causes a 45° rotation. The HWP with optic axis at position 1 sees this rotated forward Stokes which now makes 22.5° with the fast axis of the HWP. This causes the HWP to cause a 45° ($2 \times 22.5^\circ$) rotation flipping across the fast axis bringing back the forward Stokes polarisation to back to horizontal. The Brewster plate would have no effect on the horizontally polarised forward Stokes

allowing it to pass through. For the same orientation, the backwards generated Stokes light is treated differently. The horizontally polarised backward Stokes enters the isolator through the Brewster plate which again will have no effect and allows complete passage. The HWP rotates the polarisation of the backward Stokes by flipping its polarisation by 45° ($2 \times 22.5^\circ$) with respect to the horizontal. Adding on to this the Faraday rotator employs a non-reciprocal rotation to the 45° oriented backward Stokes light making it perfectly perpendicular to the horizontal. Thus we find that orienting the fast axis of the HWP along position 1 allows unaltered passage for forwards Stokes whereas rotates the polarisation by 90° for the backwards Stokes on travelling through the isolator. The 90° rotated backward Stokes sees significant loss due to the Brewster plate thereby preventing the laser reaching threshold for backward Stokes generation and forcing the laser to go forwards only. This is depicted in figure 2.21.


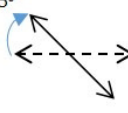
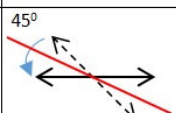
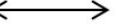
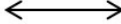


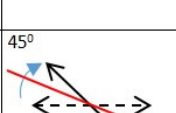



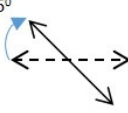



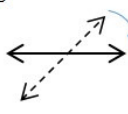



	Entry (FSRS) Exit (BSRS)	Faraday rotator	Half wave plate	Brewster plate	Entry (BSRS) Exit (FSRS)	
Pure forward operation	(1) 					Forward SRS
	(2) 					Backward SRS
Pure backward operation	(3) 				No output	Forward SRS
	(4) 					Backward SRS

Fig. 2.21 Action of isolator for pure forward and pure backward operation. Rows (1) and (2) represents effect of isolator on forward Stokes (FSRS) and backward Stokes (BSRS) for pure forward Stokes generation (with HWP in position 1) and rows (3) and (4) represents effect of isolator on forward Stokes and backward Stokes for pure backward operation (with HWP in position 2).

The same arguments can be applied to understand pure backward operation where the fast axis of the HWP is oriented at position 2, 67.5° with the horizontal. The horizontally polarised forward Stokes enters the isolator through Faraday rotator which causes a 45° rotation. The HWP with optics axis at position 2 sees this rotated forward Stokes which now makes 22.5° with the fast axis of the HWP. This causes the HWP to cause a 45° ($2 \times 22.5^\circ$) rotation flipping across the fast axis making the forward Stokes polarisation vertical. The Brewster plate would induce a significant loss for the forward Stokes completely. Whereas the horizontally polarised backward Stokes enters the isolator through the Brewster plate which again will have no effect and allows complete passage. The HWP rotates the polarisation of the backward Stokes by flipping its polarisation across position 2 by 135° ($2 \times 67.5^\circ$), in other words 45° with respect to the horizontal. Adding on to this the Faraday rotator employs a non-reciprocal rotation to the 45° oriented backward Stokes light making it perfectly parallel to the horizontal. Thus orienting the fast axis of HWP in position 2 results in strong loss for forward Stokes and enables the system to run in pure backward mode.

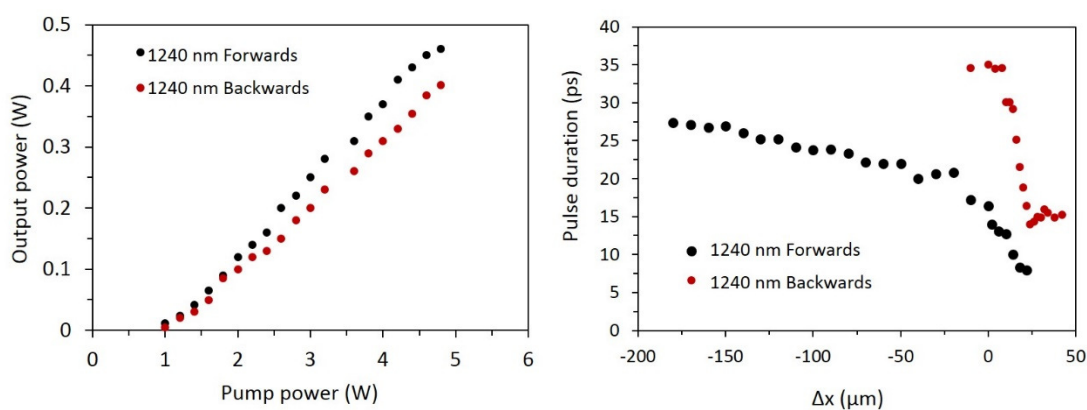


Fig. 2.22 Power transfer measurements (left) and pulse duration measurements (right) of pure forward and pure backwards first Stokes (1240 nm) generation.

The introduction of the isolator into the cavity successfully enabled the first Stokes generation into pure forward 1240 nm or pure backward 1240 nm operation. The two modes were characterized and observations are presented in figures 2.22 and 2.23. The power scaling measurements and pulse duration measurements are shown in figure 2.22 with the power transfer measurements made at $\Delta x = 0 \mu\text{m}$. At

maximum pump power, 0.46 W of forward Stokes and 0.40 W of backward Stokes was observed corresponding to overall conversion efficiency of 9.5 % and 8.3 % respectively. This efficiency is lower than that was observed without the isolator where efficiencies of 13.5 % and 9.3 % was observed for forwards and backwards first-Stokes respectively.

The reduced overall conversion efficiency can be attributed to the losses induced by the isolator components. The decreased intracavity field also results in the absence of second Stokes generation. The forwards Stokes was observed to have a minimum pulse duration of 8 ps at $\Delta x = 22 \mu\text{m}$ which is similar to the minimum pulse width observed in section 2.3.5 with the isolator absent. The backwards Stokes had pulse widths greater than 35 ps for negative detuning, (limited by the scanning range of the autocorrelator) it showed sharp reduction in pulse width towards the positive end of the stability range. A minimum pulse width of 15 ps was observed at $\Delta x = 28 \mu\text{m}$, which is similar to the pump pulse duration.

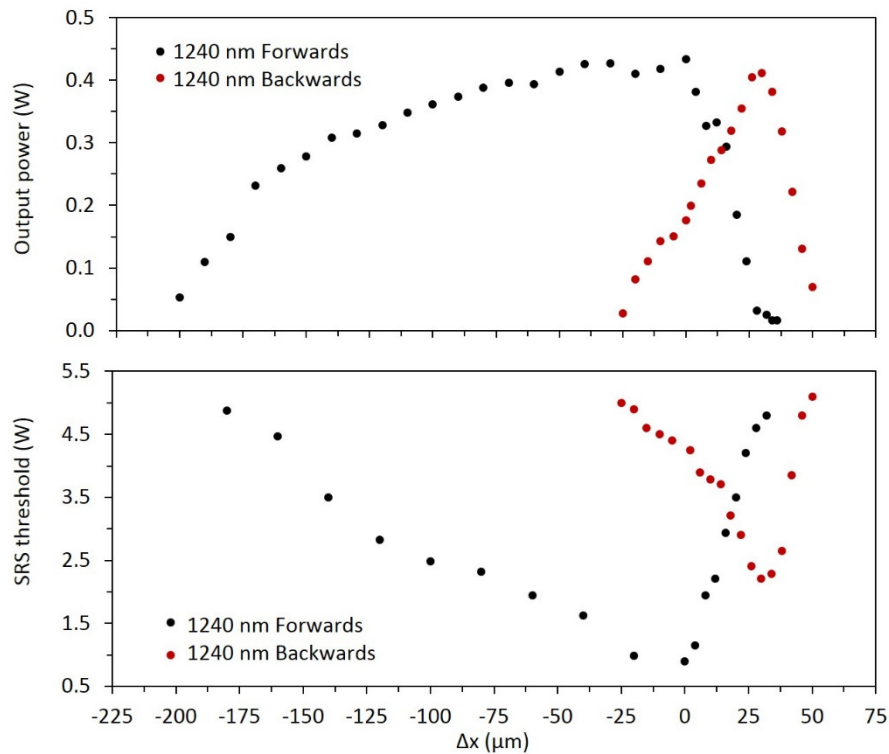


Fig. 2.23 Output power (top) and SRS threshold (bottom) variation with respect to cavity length detuning for pure forwards and pure backwards 1240 nm Stokes generation.

The laser performance of Stokes output power and SRS threshold is given in figure 2.23. The above graphs represent separate observations for pure forward and pure backward cases. They are put together to easily compare with the non-isolator case. The fluctuation in generation near $\Delta x = 0$ was reduced due to less competition between different processes. The top graph of figure 2.23 shows the pure forward and pure backward 1240 nm Stokes power over the stability range, while the bottom graph gives the SRS threshold for each case. The cavity detuning is defined as before with $\Delta x = 0 \mu\text{m}$ for minimum threshold for forwards first Stokes generation. The pure forwards 1240 nm generation had a minimum threshold of 0.8 W while the backwards had a threshold of 2.2 W which indeed is higher compared to the non-isolator case of section 2.3.5. This can be clearly seen from figure 2.24 which compares the laser performances of backward Stokes generation between the two cases, one without the isolator and another with isolator in the cavity. The red graph represents the observations with isolator in the cavity while the black one represents the one without isolator. We see that isolator allows the backwards oscillation to operate for slightly more negative Δx , owing to the removal of competition.

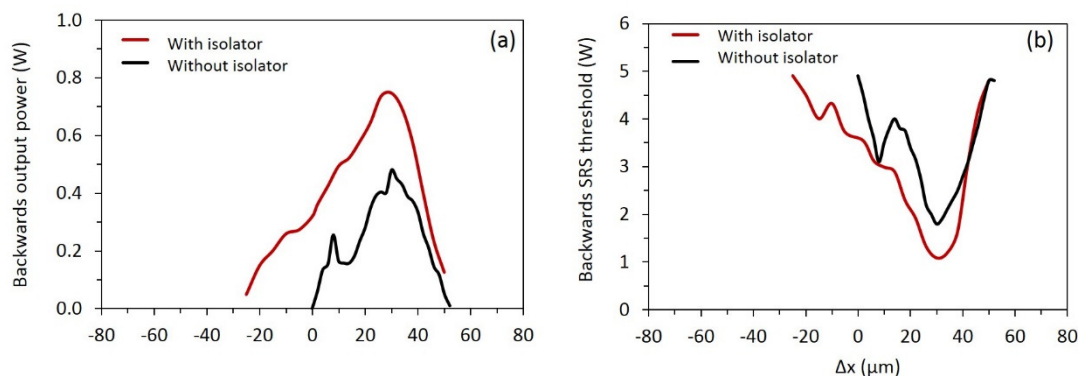


Fig. 2.24 Comparison of laser performances with and without an isolator. (a) Backward Stokes generation and (b) backward SRS threshold variation on cavity detuning.

Figure 2.25 shows the pulse duration, output power and pump depletion for backwards Stokes as a function of Δx . We do observe shortest pulses at the maximum output power for the pure backward Raman laser, which indeed is shorter

compared to the non-isolated case where pulse widths were greater than 35 ps. The minimum pulse width for pure backward Raman laser was 15 ps, which is similar to the pump pulse so showing no compression compared to the pump pulse.

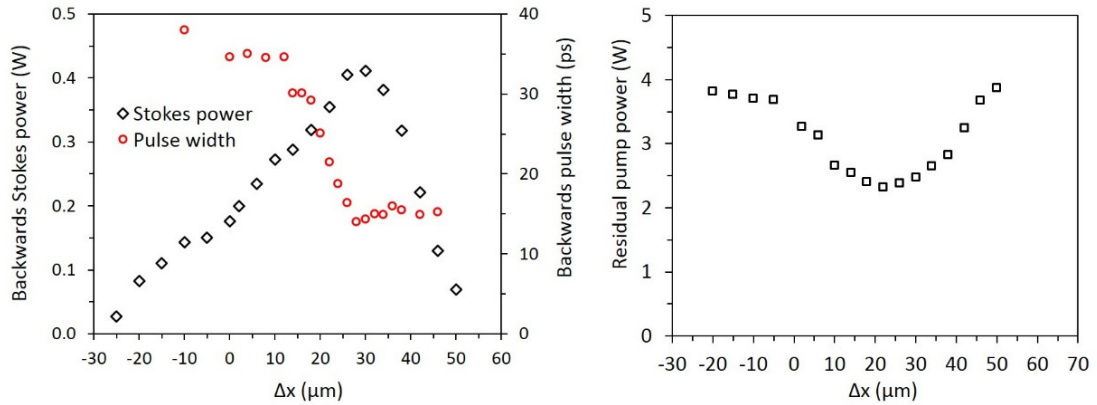


Fig. 2.25 Pulse compression and Stokes output power comparison (left) and residual pump power measurement (right) for pure backward Stokes generation.

The fact that no net compression is observed for pure backward Raman laser in contrast to the observation of previously mentioned backward SRS compression in the literature, can be attributed to weak depletion of the pump by the backward generated Stokes pulses. A residual pump power measurement was done by measuring the leaking pump through mirror M3 and is shown in figure 2.25.

The measurement show that the maximum pump of 4.8 W was depleted relatively weakly, with maximum depletion at $\Delta x = 22 \mu\text{m}$ at which shortest pulses and maximum backward Stokes output power was observed. Strong compression would require a short Stokes pulse extracting the majority of the power from the pump, preventing creation and amplification of an extended Stokes tail. Without strong depletion this does not occur. We suggest that with more pump power or reduced losses we might achieve more significant depletion, and compression may well be possible.

2.4 Chapter Summary

In conclusion, we have demonstrated a simple and highly efficient picosecond diamond Raman laser operating at both 1240 nm and 1485 nm in diamond by using a CW mod-locked pumped synchronous Raman laser in a ring configuration. Up to 2.75 W output power and 59% conversion efficiency was achieved for the first-Stokes 1240 nm in a low-Q Raman cavity. The slope efficiency tended towards 76% when the pump was far above the SRS threshold. The system has great potential in power scaling for the Stokes generation owing to the high slope efficiency and to the superior thermal properties of diamond.

Efficient generation of second Stokes was achieved by four-wave-mixing seeding of single-pass generation, making the cavity design easier with mirror coatings not required to have reflectivities at the second Stokes wavelength and not requiring any intracavity dispersion management. We generated 1.0 W output power at 1485 nm with 21% overall conversion efficiency. The importance of reflectivity losses by the end faces of the Raman crystal contributing towards the total loss in the system and hence its effect on the efficiency of lasing was demonstrated by comparing the laser activity of two diamond crystal of same length but different end face reflectivities for Stokes wavelengths. Prospects of pulse compression in synchronously pumped systems was discussed and evaluated in terms of the present system.

The ring laser design is a convenient design for enabling separate investigation of forwards and backwards operation. Pure forwards and backwards operation for the first Stokes was demonstrated by introducing an optical isolator into the cavity. We did not observe pulse compression of the backward Stokes pulses. Efficient compression in backward Raman lasers may require greater pump depletion, so operating further above the laser threshold.

2.5 References for Chapter 2

- [1] C. Ramaswamy, Raman Effect in Diamond, *Nature*, 125 (1930) 704.
- [2] R. Robertson, J. Fox, Infra-red Spectrum of Diamond by Infra-red Spectrometer and Raman Methods, *Nature*, 125 (1930) 704.
- [3] S. Bhagavantam, Relation of Raman Effect to Crystal Structure and Properties of Diamond, (1930).
- [4] F. Robertson, *Martin Phil. Trans. Roy. Soc.*, 232 (1934) 482.
- [5] P. Nayar, The lattice and electronic spectrum of diamond, *Proceedings of the Indian Academy of Sciences-Section A*, Springer, 1942, pp. 293-309.
- [6] R. Mildren, J. Rabeau, *Optical engineering of diamond*, John Wiley & Sons, 2013.
- [7] A. McQuillan, W. Clements, B. Stoicheff, Stimulated Raman emission in diamond: Spectrum, gain, and angular distribution of intensity, *Physical Review A*, 1 (1970) 628.
- [8] G. Eckhardt, D. Bortfeld, M. Geller, Stimulated emission of Stokes and anti-Stokes Raman lines from diamond, calcite and α -sulphur single crystals, *Applied Physics Letters*, 3 (1963) 137-138.
- [9] P. Černý, H. Jelínková, Near-quantum-limit efficiency of picosecond stimulated Raman scattering in BaWO₄ crystal, *Optics Letters*, 27 (2002) 360-362.
- [10] R.P. Mildren, J.E. Butler, J.R. Rabeau, CVD-diamond external cavity Raman laser at 573 nm, *Optics Express*, 16 (2008) 18950-18955.
- [11] R.P. Mildren, A. Sabella, Highly efficient diamond Raman laser, *Optics Letters*, 34 (2009) 2811-2813.
- [12] D.J. Spence, E. Granados, R.P. Mildren, Mode-locked picosecond diamond Raman laser, *Optics Letters*, 35 (2010) 556-558.
- [13] E. Granados, D.J. Spence, R.P. Mildren, Deep ultraviolet diamond Raman laser, *Optics Express*, 19 (2011) 10857-10863.
- [14] A. Sabella, J.A. Piper, R.P. Mildren, 1240 nm diamond Raman laser operating near the quantum limit, *Optics Letters*, 35 (2010) 3874-3876.
- [15] E. Granados, H.M. Pask, D.J. Spence, Synchronously pumped continuous-wave mode-locked yellow Raman laser at 559 nm, *Optics Express*, 17 (2009) 569-574.

- [16] E. Granados, H.M. Pask, E. Esposito, G. McConnell, D.J. Spence, Multi-wavelength, all-solid-state, continuous wave mode locked picosecond Raman laser, *Optics Express*, 18 (2010) 5289-5294.
- [17] Q. Fu, G. Mak, H. Van Driel, High-power, 62-fs infrared optical parametric oscillator synchronously pumped by a 76-MHz Ti:sapphire laser, *Optics Letters*, 17 (1992) 1006-1008.
- [18] E. Granados, D.J. Spence, Pulse compression in synchronously pumped mode locked Raman lasers, *Optics Express*, 18 (2010) 20422-20427.
- [19] D.J. Spence, E. Granados, H.M. Pask, R.P. Mildren, KGW and diamond picosecond visible Raman lasers, *Advanced Solid-State Photonics*, Optical Society of America, 2010, pp. ATuA20.
- [20] W.A. Reed, A.J. Stentz, T.A. Strasser, Article comprising a cascaded raman fiber laser, Google Patents, 1998.
- [21] B. Min, T.J. Kippenberg, K.J. Vahala, Compact, fiber-compatible, cascaded Raman laser, *Optics Letters*, 28 (2003) 1507-1509.
- [22] Y.-G. Han, C.-S. Kim, J.U. Kang, U.-C. Paek, Y. Chung, Multiwavelength Raman fiber-ring laser based on tunable cascaded long-period fiber gratings, *Photonics Technology Letters*, IEEE, 15 (2003) 383-385.
- [23] F. Koch, P. Reeves-Hall, S. Chernikov, J. Taylor, CW, multiple wavelength, room temperature, Raman fiber ring laser with external 19 channel, 10 GHz pulse generation in a single electro-absorption modulator, *Optical Fiber Communication Conference and Exhibit*, 2001. OFC 2001, pp. WDD7-WDD7.
- [24] Z. Chu, U.N. Singh, T.D. Wilkerson, Multiple Stokes wavelength generation in H₂, D₂, and CH₄ for lidar aerosol measurements, *Applied Optics*, 30 (1991) 4350-4357.
- [25] Y. Feng, S. Huang, A. Shirakawa, K.-i. Ueda, Multiple-color cw visible lasers by frequency sum-mixing in a cascading Raman fiber laser, *Optics Express*, 12 (2004) 1843-1847.
- [26] Y. Feng, L.R. Taylor, D.B. Calia, 25 W Raman-fiber-amplifier-based 589 nm laser for laser guide star, *Optics Express*, 17 (2009) 19021-19026.

- [27] A. Kaminskii, M. Bettinelli, J. Dong, D. Jaque, K. Ueda, Nanosecond Nd³⁺:LuVO₄ self-Raman laser, *Laser Physics Letters*, 6 (2009) 374.
- [28] R.T. White, T.M. Monro, Cascaded Raman shifting of high-peak-power nanosecond pulses in As₂S₃ and As₂Se₃ optical fibers, *Optics Letters*, 36 (2011) 2351-2353.
- [29] T.T. Basiev, M.E. Doroshenko, L.I. Ivleva, S.N. Smetanin, M. Jelínek, V. Kubeček, H. Jelínková, Four-wave-mixing generation of SRS components in BaWO₄ and SrWO₄ crystals under picosecond excitation, *Quantum Electronics*, 43 (2013) 616.
- [30] A. Gouveia-Neto, A. Gomes, J. Taylor, Femtosecond soliton Raman generation, *IEEE Journal of Quantum Electronics*, 24 (1988) 332-340.
- [31] A. Penzkofer, A. Laubereau, W. Kaiser, High intensity Raman interactions, *Progress in Quantum Electronics*, 6 (1979) 55-140.
- [32] F. Peter, Über Brechungsindizes und Absorptionskonstanten des Diamanten zwischen 644 und 226 μ m, *Zeitschrift für Physik A Hadrons and Nuclei*, 15 (1923) 358-368.
- [33] V. Lisinetskii, S. Rozhok, D. Bus'ko, R. Chulkov, A. Grabtchikov, V. Orlovich, T. Basiev, P. Zverev, Measurements of Raman gain coefficient for barium tungstate crystal, *Laser Physics Letters*, 2 (2005) 396-400.
- [34] T.T. Basiev, S.N. Smetanin, A.S. Shurygin, A.V. Fedin, Parametric coupling of frequency components at stimulated Raman scattering in solids, *Physics-Uspekhi*, 53 (2010) 611.
- [35] L. Schoulepnikoff, V. Mitev, High-gain single-pass stimulated Raman scattering and four-wave mixing in a focused beam geometry: a numerical study, *Pure and Applied Optics: Journal of the European Optical Society Part A*, 6 (1997) 277.
- [36] T. Basiev, S. Smetanin, A. Fedin, A. Shurygin, Four-wave parametric processes in multicascade SRS conversion of neodymium laser radiation into an eye-safe region, *Optics and Spectroscopy*, 107 (2009) 353-358.
- [37] Y.-R. Shen, *Principles of nonlinear optics*, (1984).
- [38] T.B. Tasoltan, A.V. Gavrilov, V.O. Vyacheslav, S.N. Smetanin, A.V. Fedin, High-average-power SRS conversion of radiation in a BaWO₄ crystal, *Quantum Electronics*, 34 (2004) 649.

- [39] I.S. Voronina, L.I. Ivleva, T.T. Basiev, P.G. Zverev, N.M. Polozkov, Active Raman media: $\text{SrWO}_4\text{:Nd}^{3+}$, $\text{BaWO}_4\text{:Nd}^{3+}$ Growth and characterization, *Journal of Optoelectronics and Advanced Materials*, 5 (2003) 887-892.
- [40] P.G. Zverev, T.T. Basiev, V.V. Osiko, A.M. Kulkov, V.N. Voitsekhovskii, V.E. Yakobson, Physical, chemical and optical properties of barium nitrate Raman crystal, *Optical Materials*, 11 (1999) 315-334.
- [41] R.L. Carman, F. Shimizu, C. Wang, N. Bloembergen, Theory of Stokes pulse shapes in transient stimulated Raman scattering, *Physical Review A*, 2 (1970) 60.
- [42] J. Murray, J. Goldhar, D. Eimerl, A. Szöke, Raman pulse compression of excimer lasers for application to laser fusion, *Quantum Electronics, IEEE Journal of*, 15 (1979) 342-368.
- [43] S. Morozov, L. Piskunova, M. Sushchik, G. Freĭdman, Formation and amplification of quasisoliton pulses in head-on stimulated scattering, *Soviet Journal of Quantum Electronics*, 8 (1978) 576.
- [44] D. Chunaev, A.Y. Karasik, Temporal characteristics of picosecond stimulated Raman scattering in oxide crystals, *Laser Physics*, 16 (2006) 1668-1671.
- [45] M. Maier, W. Kaiser, J. Giordmaine, Intense light bursts in the stimulated Raman effect, *Physical Review Letters*, 17 (1966) 1275.
- [46] A.J. Glass, 7.4-Design considerations for Raman lasers, *Quantum Electronics, IEEE Journal of*, 3 (1967) 516-520.
- [47] A.M. Zaitsev, *Optical properties of diamond: a data handbook*, Springer Science & Business Media, 2013.

3

Multiwavelength ultrafast LiNbO₃ Raman laser

This chapter introduces a multiwavelength ultrafast Raman laser based on lithium niobate which utilizes stimulated Raman scattering (SRS) as well as stimulated polariton scattering (SPS) in a synchronously pumped cavity, using different scattering frequencies to switchably or simultaneously convert the pump light to a set of new wavelengths.

3.1 Lithium niobate crystal and tunability of Raman medium

Non-centrosymmetric crystals like LiNbO₃ can have both Raman active and infrared active transverse optical modes called A₁(TO) modes. Lithium niobate (LiNbO₃), a negative uniaxial crystal, has been one of the best materials for frequency conversion due to its large $\chi^{(2)}$ and $\chi^{(3)}$ nonlinear coefficients [1] and its transparency over a wide wavelength range [2] as can be seen from figure 3.1. It belongs to space group R3c

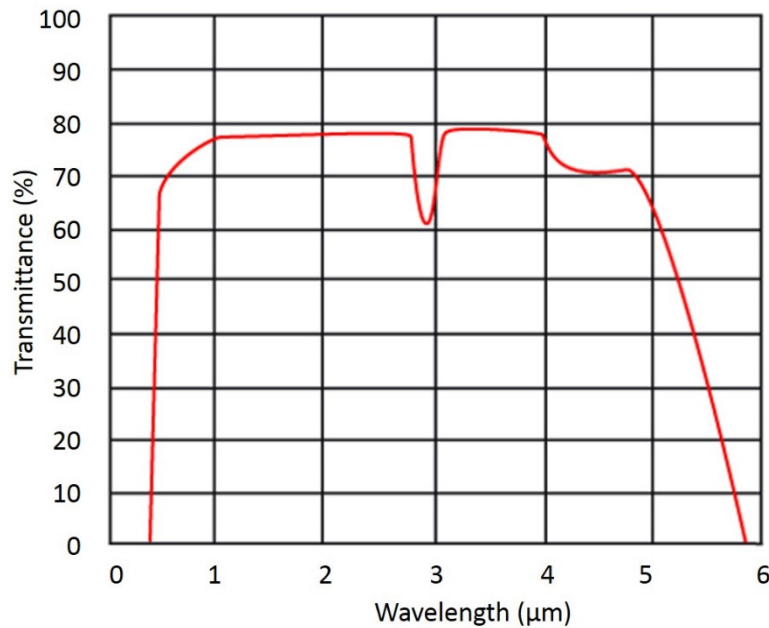


Fig. 3.1 Transparency of coated and uncoated lithium niobate crystal [2].

and has a perovskite-type structure below the Curie temperature (1210°C). Oxygen atom planes are arranged in distorted hexagonal closed-packed arrangement along with the interstices filled alternatively by lithium ions, niobium atoms and vacancies. The unit cell of lithium niobate is depicted in figure 3.2. In a perfect crystal, each Li or Nb atom is surrounded by a distorted octahedron of O^{2-} ions [3] whereas in a real crystal the stoichiometry depends on the method of manufacturing.

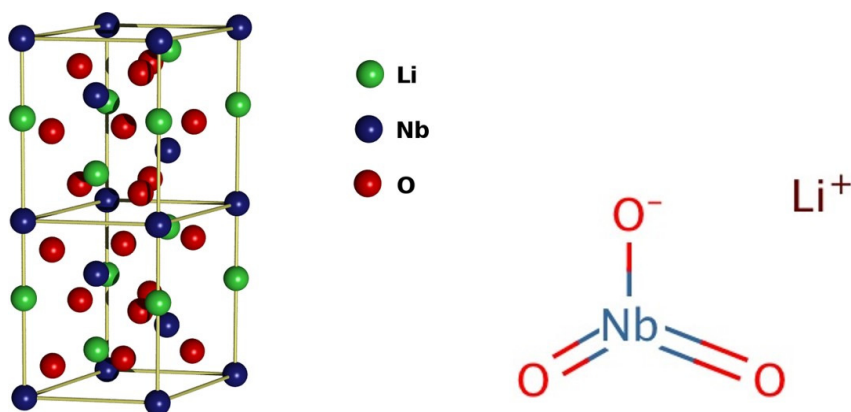


Fig. 3.2 Structure of lithium niobate crystal with polar bonds.

From the Bhagavantham method, the irreducible representation of optical modes in lithium niobate are found to be as a sum of $4A_1$, $5A_2$ and 9 E modes [4, 5] of which

A₁ and E modes are both infrared and Raman active while A₂ modes are Raman inactive. Johnston *et. al.* observe that long range electrostatic fields in the ionic crystal lift the degeneracy between longitudinal and transverse optical phonons, thereby doubling the number of observed modes [6, 7]. A typical Raman spectrum of lithium niobate taken by Scott *et. al.* is shown in figure 3.3 , with neon reference lines, taken using a Renishaw Raman microscope [6]. Even though the Bhagavantham method predicts 26 phonon modes in lithium niobate, the actual number of peaks that would be observed in the Raman spectrum will depend on the relative orientation of the crystal with respect to the spectrometer and the polarisation direction of the incident and scattered light.

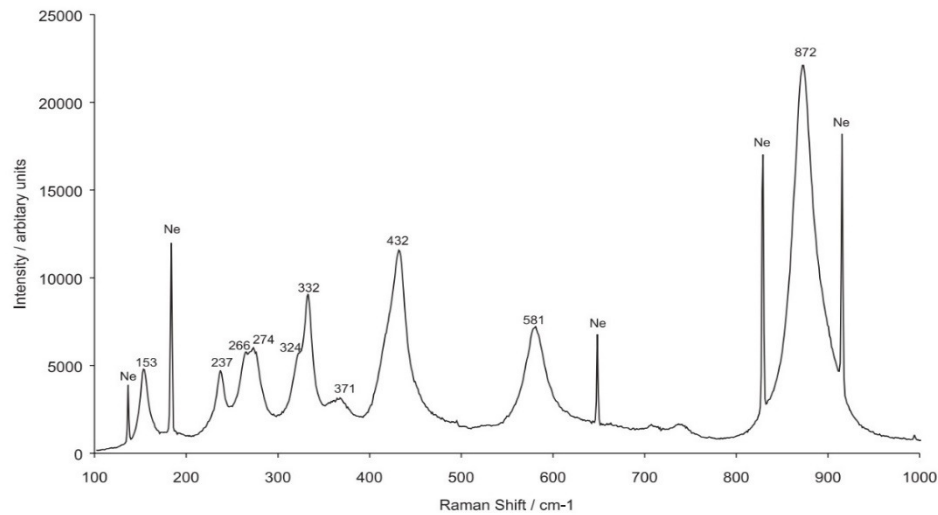


Fig. 3.3 A typical lithium niobate Raman spectrum with neon reference lines from [6].

LiNbO₃ is uniaxial with the optic axis conventionally the z-axis. When we talk about a crystal cut it generally refers to the axis along which our beam will propagate. Hence x-cut crystal has the laser beam propagating along the x-axis. Given in figure 3.4 is the reflection Raman spectra taken by Helen M. Pask (Macquarie University, Sydney Australia) using a Renishaw In Via Raman spectrometer at Sydney University. It shows backscattered Raman spectra of x-cut lithium niobate crystal for two orientations relative to the excitation laser polarisation, with a 514 nm excitation and a resolution of 2 cm⁻¹. It can be clearly seen that the orientation of the pump polarisation with respect to the optic axis determines the family of Raman lines.

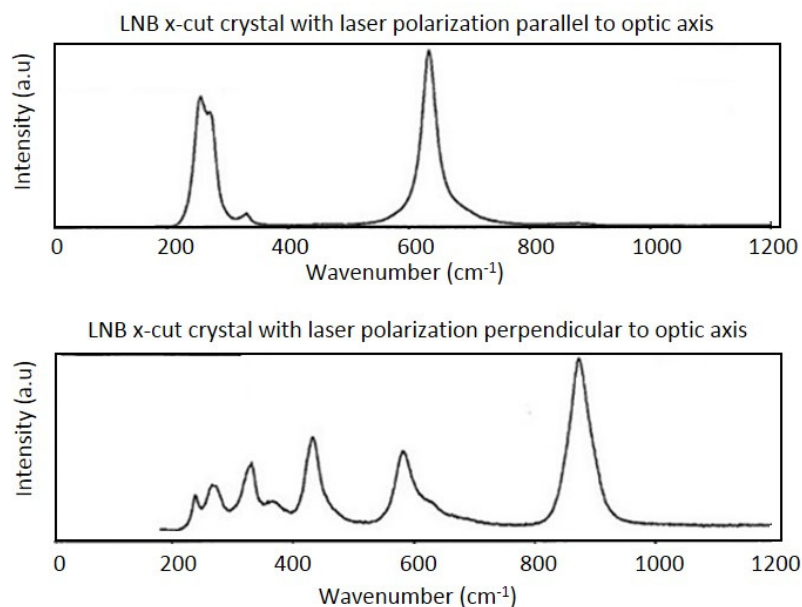


Fig. 3.4 Backward Raman spectra of lithium niobate for different orientations of the x-cut crystal relative to the excitation laser polarisation. Taken by Helen M. Pask.

The Raman spectrum of a lithium niobate crystal also depends upon its composition. Two types of crystals are available in the market - stoichiometric and congruent crystals. Stoichiometric are those ones which contain equal portions of lithium and niobate (composition $R=[\text{Li}]/[\text{Nb}]=1$) while the congruent ones are those with lower concentration of lithium ions (composition $R=[\text{Li}]/[\text{Nb}]<1$). Ridah *et. al.* presents a composition dependence study of the Raman spectrum along with various scattering configurations in [8]. They observe significant differences in the shape and the number of Raman peaks between the recorded spectra of congruent and nearly stoichiometric crystals of lithium niobate. They also summarise the complete list of transverse and longitudinal optical modes for different compositions and different orientations. Temperature also seems to be a dependency factor for Raman spectra for lithium niobate which was studied by Sidorov *et. al.* in [9].

Lithium niobate is subjected to a refractive index change on laser irradiation, usually termed as a photorefractive effect or optical distortion effect [10, 11]. This refractive index changing effect forms a major hindrance for application of lithium niobate for frequency conversion, electro-optical modulation etc. [12, 13]. Doping the crystal

with non-photorefractive cations like Mg²⁺, Zn²⁺, In²⁺ etc which do not change their state in the crystal structure upon illumination, is one of the methods employed for reduction of the photorefractive effect. Sidorov *et. al.* presents an extensive study of the effect of different compositions of Li and Nb as well as doping of different non-photorefractive cations on the Raman spectra in [14]. The photorefractive effect can manifest in the appearance of Raman lines which are crystallographically forbidden for given scattering geometry [14]. Our lithium niobate crystal has 5 % molar doping of magnesium ions to reduce the photorefractive effect.

The high nonlinear coefficients of lithium niobate facilitates efficient frequency doubling, sum frequency generation, difference frequency generation and use in optical parametric oscillators. For example Michael *et. al.* in [15] reported efficient frequency-doubling of single-frequency 1029 nm light to green light at 514.5 nm using a single-pass configuration. Furuya *et. al.* generated continuous-wave 3 W green-light at 542 nm in bulk periodically poled MgO:LiNbO₃ using single-pass frequency doubling of a Yb-doped fiber laser operating at 1084 nm [16]. Lithium niobate has also found application in generating infrared wavelengths. Ebrahimzadeh *et. al.* generated tunable high-repetition-rate optical pulses in the mid-infrared using synchronously pumped parametric oscillation in periodically poled LiNbO₃ crystal [17].

Lithium niobate with its exciting nonlinear properties also finds immense application as a Raman active material for the generation of wavelengths in the infrared and terahertz regions. The pioneering initial studies in lithium niobate were carried out by Barker and Loudon [18, 19] and Pantell and Puthoff [20, 21] in which they discovered the possibility of generating tunable radiation. Yarborough *et. al.* in [21] reports for the first time tunable stimulated optical emission from lithium niobate without a resonator where the A₁ symmetry 248 cm⁻¹ polariton mode was excited with a q-switched ruby laser and the signal frequency was tuned by varying the angle of incidence of the laser beam relative to the normal of the crystal surface. In the next section we discuss this effect in detail.

3.2 Tunable wavelength generation from lithium niobate

In Raman and parametric scattering processes, passing of a laser (pump frequency) through a media generates new frequencies (signal and idler frequencies). Both the processes obey the conservation of energy with the sum of signal and idler frequencies equal to the pump frequency. In non-polar materials, $\chi^{(3)}$ Raman scattering generates an idler wave that is purely mechanical vibration in nature, corresponding to a vibrational resonance of the nonlinear material. $\chi^{(2)}$ parametric scattering generates idler frequencies which are purely electromagnetic in nature. Thus parametric scattering results in optical signal and idler frequencies, while Raman scattering produces only optical signal frequency termed as the Stokes waves [22]. The Raman process is non-tunable as it depends on the fixed vibrational energy levels of the medium. Parametric scattering is tunable, determined by the wavevector phase matching.

When the Raman medium is polar, a dipole moment at the vibrational frequency is generated by optical vibration of the lattice. Such materials then become capable of absorbing and emitting electromagnetic radiation associated with that vibration. Since the frequencies and wave vectors of the transverse optical vibrational modes of the medium are identical to that of the associated electromagnetic waves, they strongly couple each other generating mixed phonon-photon excitations. The dispersion relationship (dependence of frequency on the wavevector) is strongly

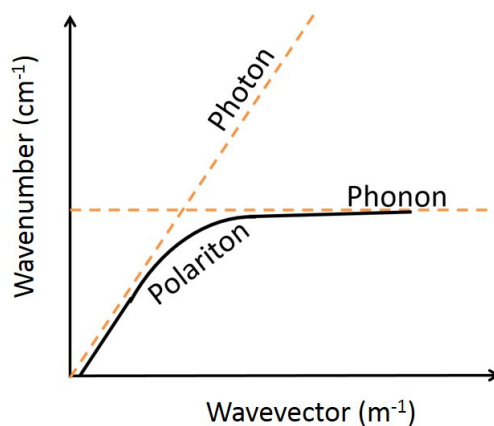


Fig. 3.5 Dispersion curve of polar materials.

affected by this coupling. The quanta associated with these coupled modes, which show both photon and phonon behaviour, are termed as polaritons [23].

Stimulated polariton scattering (SPS) is then an inelastic process that involves both $\chi^{(2)}$ and $\chi^{(3)}$ interactions. Unlike stimulated Raman scattering (SRS), in SPS the frequency is a function of the angle between the pump and Stokes fields. The dispersion curve of these new mixed modes of polaritons are photon-like at smaller wave vectors with most of the energy in the lattice electromagnetic in nature, whereas the modes evolve to phonon-like at higher wave vectors with most of the energy in the lattice mechanical in nature. This is schematically shown in figure 3.5. With this dispersion curve we can tune the exacted polariton frequency by altering the wavevector. By controlling the signal wave vector which in turn decides the idler frequency according to the dispersion curve tunability is obtained. A change in the scattering angle alters the wavevector of the polaritons participating in the scattering process thereby altering the scattered light colour. This concept of generating tunable radiations from crystal which are both Raman active and Infrared active, was first proposed independently by Loudon [18] and Pantell and Puthoff [20, 21, 24].

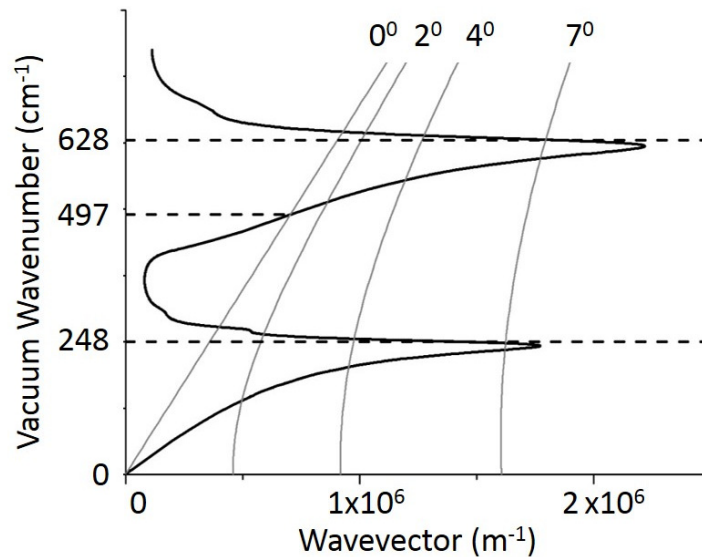


Fig. 3.6. Dispersion curve of lithium niobate calculated using data from [19] with phase matching curves for small angle scattering of a 1064 nm pump laser.

Lithium niobate has two strong vibrational modes with wavenumbers 248 cm^{-1} and 628 cm^{-1} that are both Raman and infrared active [19]. The dispersion curve of lithium niobate with 1064 nm pumping, shown in figure 3.6, has been reconstructed from data in [19]. Conservation of energy and momentum would only allow generation of those frequencies that lie on the dispersion curve as well as on the phase matching curves. The phase-matching curves show which polariton wavevector is required to phase match the scattering process for a given polariton frequency and scattering angle. The scattered frequency is determined by the intersection of the phase matching curves and the polariton dispersion curve as shown in figure 3.6.

For lithium niobate, the polariton associated with the 248 cm^{-1} vibrational mode generates THz radiation for angles of a few degrees between the pump and Stokes fields and for angles $\gtrsim 7^\circ$ the polariton is predominantly vibrational in nature and tends to a resonant frequency of 248 cm^{-1} . Small angle scattering of polaritons associated with 248 cm^{-1} resulting in THz radiation is one of the common methods used for THz wave generation from polar crystals [25]. The polariton associated with the 628 cm^{-1} vibrational mode has a resonant frequency of 497 cm^{-1} for co-propagating pump and Stokes (0° scattering); for angles $\gtrsim 7^\circ$ the polariton is predominantly vibrational in nature and tends to a resonant frequency of 628 cm^{-1} .

This kind of tunable radiation generation from crystals which are both infrared and Raman active was first proposed by Loudon [18], Pantell and Puthoff [24]. SPS was first observed in lithium niobate by Kurtz *et. al.* [26], when pumped by a q-switched ruby laser resulting in forward Stokes output shifted by 497 cm^{-1} and backward Stokes shifted by 631 cm^{-1} . They observed strong dependence of the lattice mode frequency on the wave vector. Changing the angle of the pump laser with respect to the cavity resulted in change of polariton wave vector causing generation of different infrared frequencies.

The pump and the Stokes fields can interact over a range of angle from 0 to 180 degrees depending upon the cavity engineering and each angle would correspond to

different Stokes and idler frequencies. They couple out of the cavity at different angles depending upon their offset from the co-propagating direction. We are going to build a collinearly pumped ring Raman laser. The unique geometry of our laser cavity allowed only near-collinear Stokes generation i.e. our laser cavity resonated only Stokes wavelengths that were collinear with the pump, including for forward scattered and backward scattered waves. The Stokes fields generated at zero degrees (i.e. forward scattered) would co-propagate with the pump fields and will be termed as clockwise fields and those generated at 180 degrees (i.e. backward scattered) will be termed as counter-clockwise fields throughout this thesis. This terminology for directions refer to the sense of rotation in the section of the bow-tie cavity containing the crystal. The experimental setup is explained in detail in the coming section. The clockwise fields are represented in orange colour and the counter-clockwise fields are represented in red colour throughout this thesis for better representation and understanding. Figure 3.7 shows schematically the Stokes generation as mentioned above. The figure also shows the Polariton scattering at small angles which is responsible for closely spaced higher order Stokes and will be discussed in detail later.

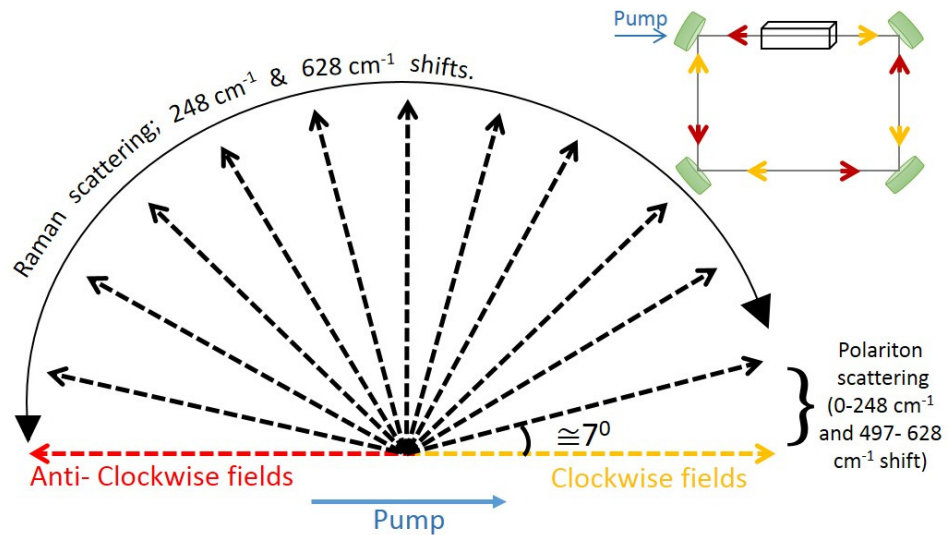


Fig. 3.7. Artistic representation of possible Stokes generation from lithium niobate in our experimental setup with representation of clockwise and counter-clockwise directions along with colour coding.

3.3 Experimental setup

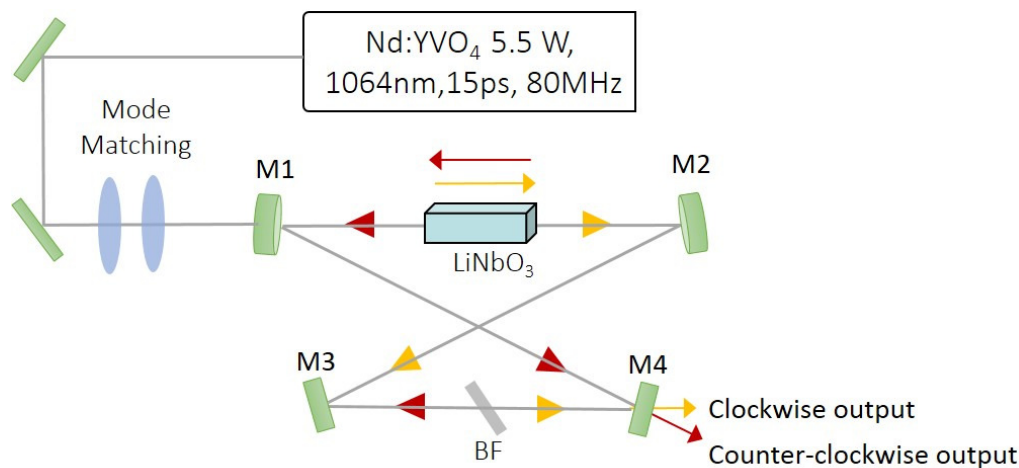


Fig. 3.8 Optical schematic of the lithium niobate Raman laser. With M1 as the input coupler and M4 as the output coupler. BF represents a birefringent filter which will be explained later. The yellow and orange arrows represent clockwise and counter-clockwise Stokes fields as explained before.

The experimental setup comprised a synchronously-pumped ring resonator as shown in figure 3.8. Red and yellow arrows are used to indicate the direction of clockwise and anti-clockwise generated Stokes beams. We used a 20 mm x -cut 5-mol %MgO-doped LiNbO₃ rectangular crystal (HC-Photonics Corp.) with antireflection-coated end faces ($R < 0.2\%$ from 1064 to 1085 nm and $R < 0.5\%$ from 1120 to 1180 nm). The folding angles at the cavity mirrors were kept as small as possible, approximately to 5 degrees, so as to minimize astigmatism. The crystal was pumped by a CW mode-locked Nd:YVO₄ laser (Spectra Physics Vanguard 2000-HM532) that generated up to 5.5 W average power at 1064 nm with pulse duration of 15 ps, repetition rate of 80 MHz, and a beam quality factor of M^2 of 1.1.

For controlling the laser power being coupled into the cavity, a half wave plate (HWP) and a polariser beam splitter (PBS) cube was employed, avoiding the change of operating characteristics as it was done in the diamond Raman laser reported in Chapter 2 of this thesis. Two concave mirrors (M1 and M2, ROC = 100 mm) and two flat mirrors (M3 and M4) made up the bow-tie shaped cavity. A separation of approximately 110 mm between M1 and M2, produced a resonator mode at the

center the crystal with a mode size of 22 μm . A pair of plano-convex lenses ($f_1 = 500\text{ mm}$, $f_2 = 150\text{ mm}$) were used for mode matching the pump beam to the cavity mode. The pump laser propagated along the x-axis of the crystal with pump polarisation parallel to z-axis of the crystal to access the highest nonlinear coefficients. To achieve synchronous pumping, the Raman cavity was length-matched with the pump laser, the cavity length being tuned by changing the position of M4 with a high-precision translation stage. Aspects of laser optimization by cavity detuning is well explained in the previous chapter as well as in [27].

3.4 Multiwavelength accessibility of our system

The pump wavelength incident into the Raman laser cavity can undergo two stages of conversion: first is the pump light getting converted to a Stokes field in the cavity, and the second that the cavity enhanced Stokes field can get shifted again (cascaded)

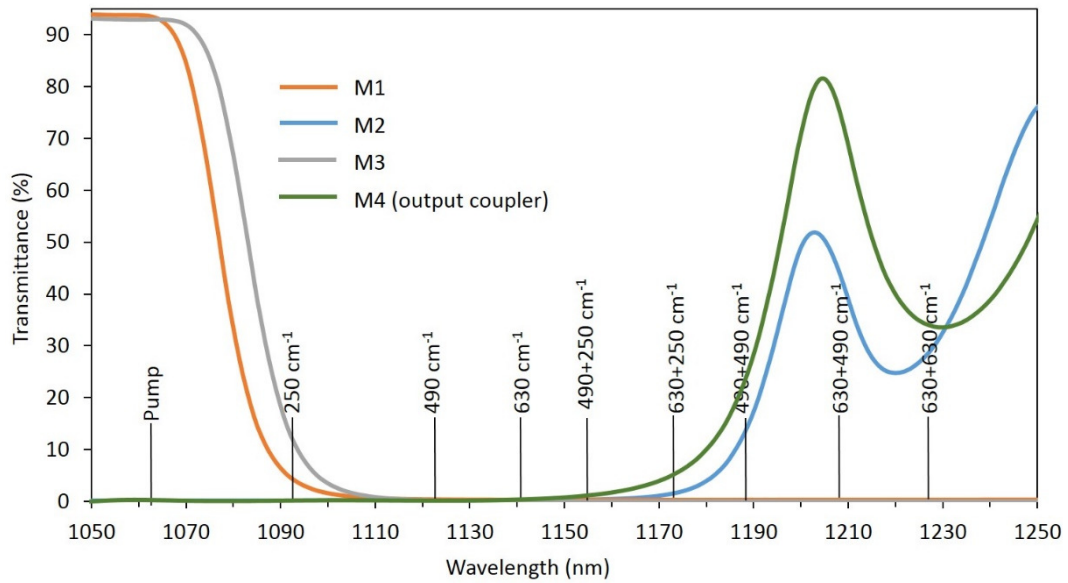


Fig. 3.9 Transmittance curves of cavity mirrors used in this experiment with the shifts and their combinations marked at their respective wavelengths.

by any of the possible SRS or SPS shifts mentioned above. Which of the shifts can couple the pump into the cavity and which of the shifts can cascade over the cavity enhanced Stokes, is determined by the reflectivities of the cavity mirrors.

The pump coupled into the cavity would in principle be either scattered forwards (497 cm^{-1} and few cm^{-1} shifts near to zero) or backwards (248 cm^{-1} and 628 cm^{-1}) generating clockwise and counter-clockwise Stokes fields respectively. The cavity was able to resonate wavelengths between 1110 nm and 1180 nm , as determined by the transmission of the cavity mirrors. Figure 3.9 shows the transmission curves of the mirrors used in the cavity measured using Carry 5000 UV-Vis-NIR spectrometer (*Agilent Technologies*). The input coupler M1 had a high reflectivity from 1110 nm to 1180 nm and the output coupler M4 started transmitting only after 1160 nm .

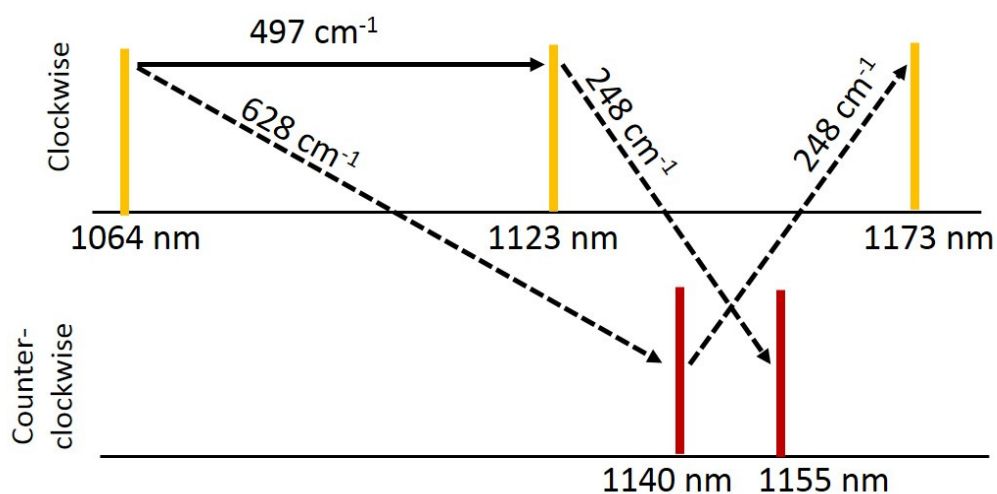


Fig. 3.10 Predicted Stokes and second Stokes in our system. Yellow lines represent clockwise fields, and red lines represent counter-clockwise field. Solid arrow represent forward scattering, and the dashed lines backward scattering.

Fig. 3.10 is a pictorial representation of all the possible wavelengths that can be generated in our system, showing clockwise (orange) and counter-clockwise (red) fields, and forward (solid arrows) and backward (dashed arrows) scattering processes. THz (polariton) and 248 cm^{-1} shifts associated with forward- and backward-scattering on the 248 cm^{-1} mode are not large enough to reach a strongly resonated wavelength. However, both the forwards- 497 cm^{-1} and backwards- 628 cm^{-1} shifts associated with the 628 cm^{-1} mode generate wavelengths supported by the cavity. The 1123 nm Stokes field generated by the

forwards-497 cm⁻¹ shift propagates clockwise in the ring cavity while the 1140 nm Stokes field generated by the backwards-628 cm⁻¹ shift propagates counter-clockwise in the ring cavity. These directions refer to the sense of rotation in the section of the bow-tie cavity containing the crystal.

These 1123 nm and 1140 nm intracavity fields can become sufficiently intense to themselves cascade to produce new wavelengths. The output coupler M4 increases in transmission rapidly for wavelengths greater than 1180 nm. Further cascading was supported on the near-forwards-THz shift or the backwards-248 cm⁻¹ shift, but cascading on 497 cm⁻¹ or 628 cm⁻¹ generates wavelengths greater than 1180 nm, not strongly resonated by the cavity mirrors. The THz shift couples power into closely-spaced Stokes wavelengths co-propagating with the generating field, and we will discuss this effect in the next chapter. The backwards-248 cm⁻¹ shift couples power from a field in one direction to a field in the counter-propagating direction. Here the clockwise 1123 nm field cascades to a counter-clockwise 1155 nm field, and the counter-clockwise 1140 nm field cascades to a clockwise 1174 nm field.

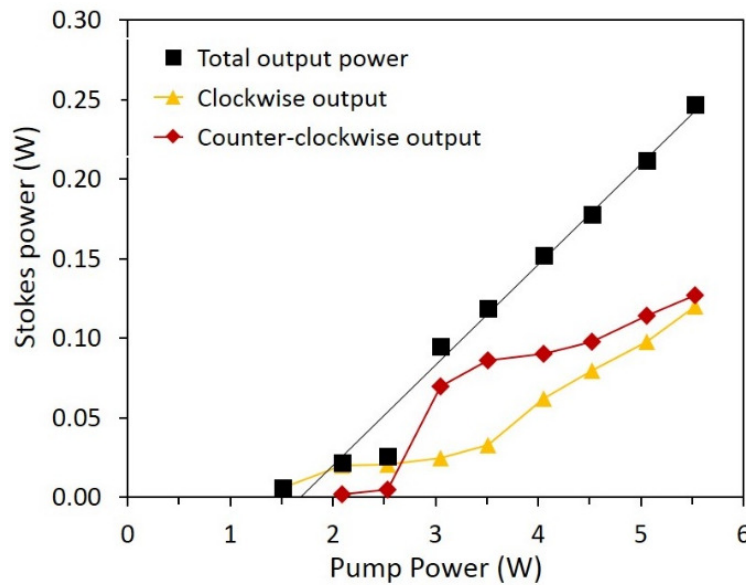


Fig. 3.11 Power transfer measurement for the laser optimised for threshold of clockwise generated Stokes output, measure though M4. The black curve is the sum of clockwise and counter-clockwise output powers.

To understand the multiple Stokes generation in our system, we studied the power transfer of the laser by measuring the output power in both clockwise and counter-

clockwise directions at the output coupler. Figure 3.11 shows the power transfer measurements of output power in clockwise direction (orange) and counter-clockwise direction (red) at different pump powers along with the total output power (black).

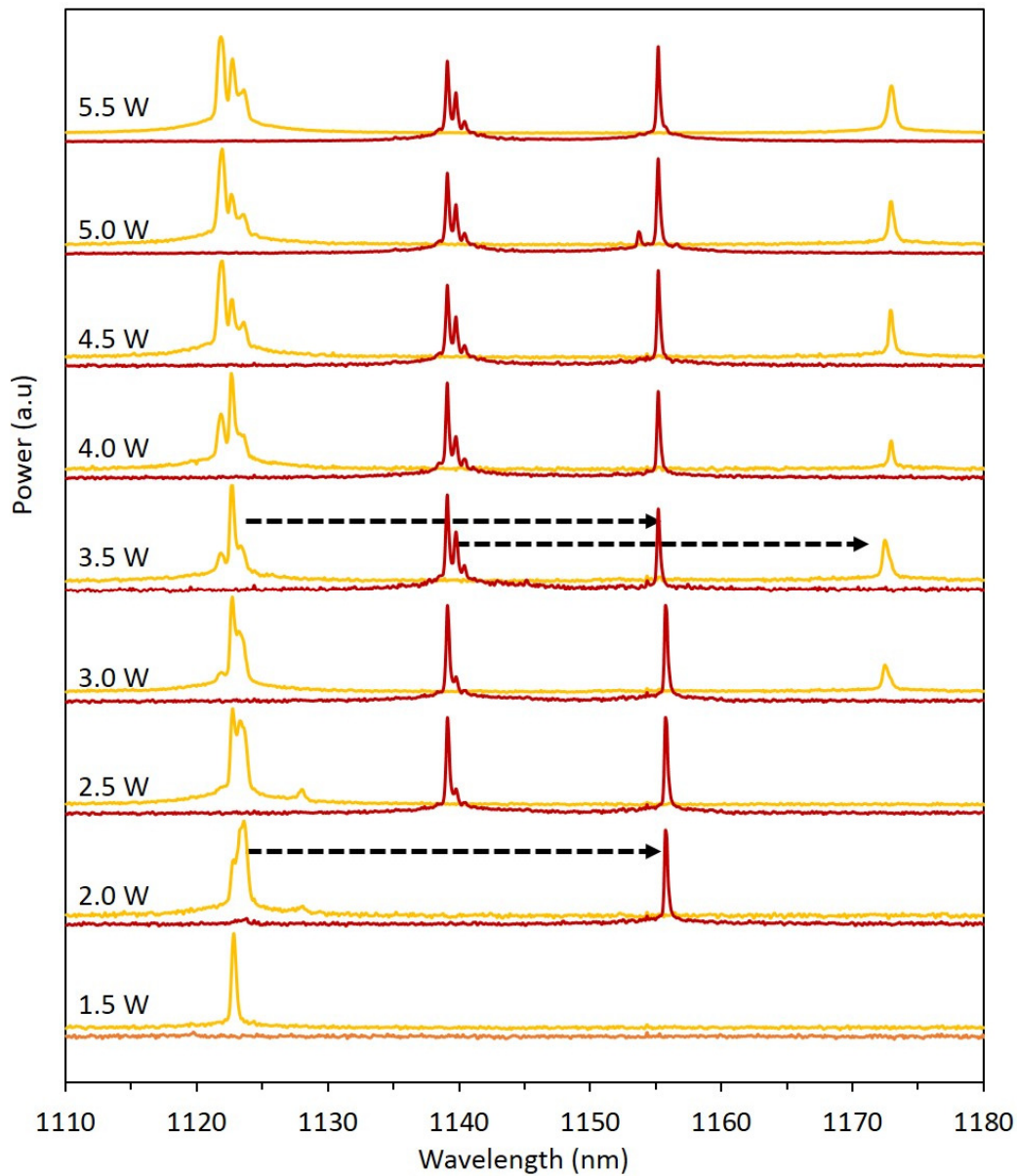


Fig. 3.12 Spectra of clockwise (orange) and counter-clockwise (red) laser output at different pump powers, shown on an arbitrary scale. The dotted arrows represent backward Raman shift (248 cm^{-1}) cascading over forward polariton (497 cm^{-1}) and backward Raman (628 cm^{-1}) shifts generating counter-clockwise and clockwise Stokes fields respectively.

The measured powers for clockwise and counter-clockwise propagating beams do not increase linearly due to competition effects, but the total output power was approximately linear with pump power with slope efficiency of 6.5 % as shown in figure 3.11. The laser had a threshold of 1.5 W. The spectrum of both clockwise and counter-clockwise generated Stokes fields were also recorded outside mirror M4 for each pump power and are depicted in figure 3.12, measured using an Ocean-optics NIR-512 spectrometer (detecting range 850 to 1700 nm with resolution of 3 nm). As mentioned before the orange and red spectrum represents the spectrum of clockwise and counter-clockwise generated Stokes fields respectively. The dashed-arrows represent cascading of cavity enhanced Stokes fields; where one observes cascading of clockwise fields into counter-clockwise fields and vice-versa.

The system lased first at 1123 nm (497 cm^{-1} shift of the pump) for pump powers over 1.5 W. For pump powers over 2.5 W, this field cascaded to generate 1155 nm (248 cm^{-1} backward shift). For pump powers greater than 3 W, we observed the 1140 nm field (628 cm^{-1} shift of the pump) along with cascading to 1174 nm (248 cm^{-1} backward shift). At maximum pump power of 5.5 W, we thus observed 1123 nm and 1174 nm clockwise fields and 1140 nm and 1155 nm counter-clockwise fields. The appearance of 1123 nm owing to the forward 497 cm^{-1} shift before 1140 nm owing to the 628 cm^{-1} shift is not surprising in our laser. The predicted gain is 1.5 times higher for the forward shift [26]; the increased overlap time for the forward scattered Stokes is also a significant factor.

The difference in Raman spectra with different orientation of the pump polarisation as discussed in the beginning of this chapter, was also observed in our experiments. Figure 3.13 shows the spectrum of our lithium niobate Raman laser with the excitation laser polarisation perpendicular to the optic axis (a) and parallel to optic axis (b) as above with different Stokes wavelengths appearing in each case. The lasing threshold was significantly higher for excitation polarisation perpendicular to the optic axis as expected for lithium niobate [28]. Hence in our experiments we always oriented the lithium niobate crystal with the pump laser polarisation parallel to the optic axis.

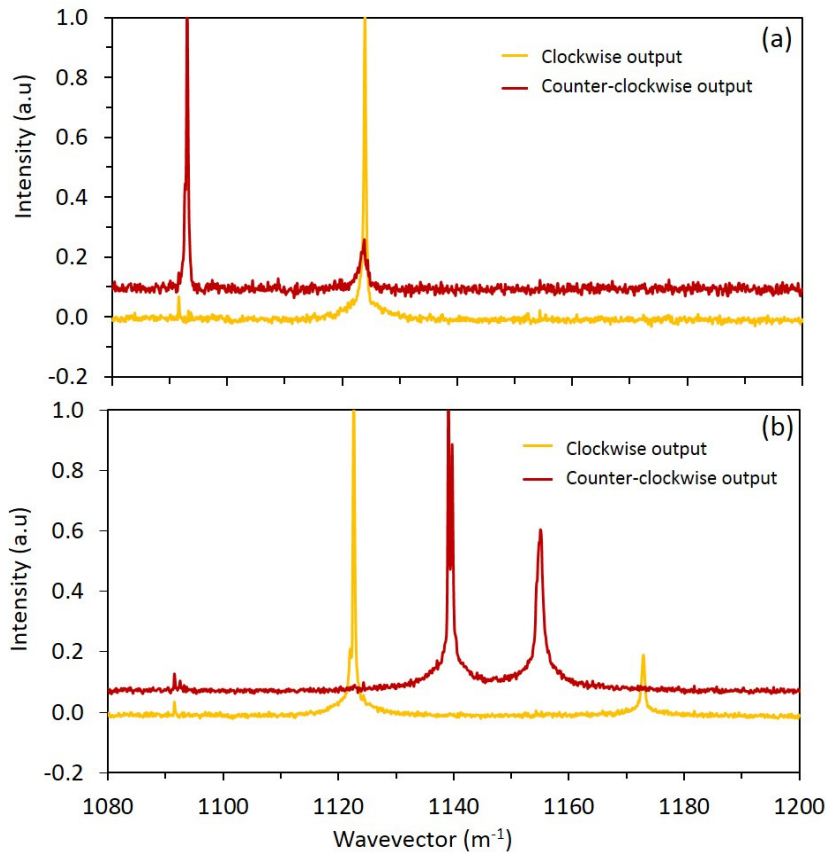


Fig. 3.13 Spectrum of lithium niobate Raman laser with excitation polarisation (a) perpendicular and (b) parallel to the optic axis.

As discussed above the system generated four wavelengths uncontrollably due to their appearance with increase of pump power. A system generating multiple wavelengths would be attractive only if we could control the multiple wavelength conversion.

3.5 Spectrally controlled laser based on a single vibrational mode

The lithium niobate Raman laser presented above was successful in generating four different wavelengths from a single pump using the two strong vibrational modes of lithium niobate by using SRS and SPS. In addition to forward and backward Stokes fields being generated in clockwise and counter-clockwise directions, those fields cascaded to generate additional fields in the reverse directions. A multiwavelength generating system becomes attractive only when its wavelength generation has a

controllable nature. We were motivated to introduce a birefringent filter into the cavity of the laser which would control the laser generation by adjusting the free spectral range (FSR) of the filter. We hoped to suppress either the 1123 nm or the 1140 nm input coupling shifts as well as suppressing (controlling) the cascading process. Thus by adjusting the birefringent filter we could select between pure 1123 nm and pure 1140 nm wavelengths.

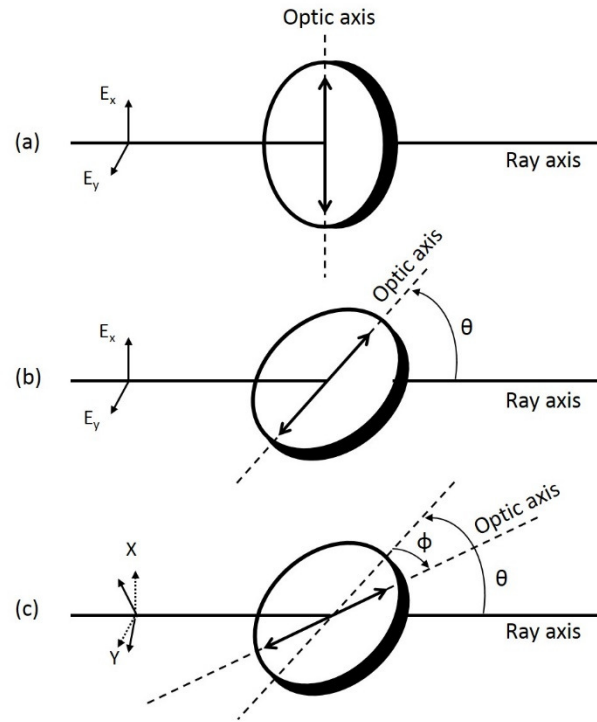


Fig. 3.14 Orientations of birefringent filter which could change the FSR. The optic axis lying in the plane of the plate is aligned with the x -axis. (a) Has the optics axis aligned perpendicular to transmitted light, (b) has the optic axis at Brewster angle to the transmitted light and (c) involves rotation of the birefringent filter in the Brewster plane. Figure taken from [29].

Birefringent filters are an efficient method for narrowing the emission spectra of tunable lasers [29]. In [30], Kobtsev *et. al.* presents a review on the use of birefringent filters for primary narrowing of laser emission spectra. A birefringent filter acts as a single-stage filter in the cavity of laser by manipulating the polarisation of the lasing wavelength exploiting the birefringence of an optically anisotropic crystalline plate. If the optic axis of the birefringent filter is at an angle to the incident polarisation, we get a cyclic modulation of the laser polarisation as the beam propagates through the

crystal. The polarisation rotation is wavelength dependent and for wavelengths that undergo integer cycles, the polarisation remains unchanged. If we add a polariser, we have a combination that is low loss for these wavelengths which undergo integer cycles and high loss for all other wavelengths. The thickness and orientation of birefringent plate is chosen so that there will be one frequency within the gain curve of the laser medium for which the polarisation will remain unaffected [29, 30]. The laser can be tuned by rotating the birefringent filter which would alter the frequency of minimum loss.

Figure 3.14, depicts the manner in which a birefringent filter would affect the transmitted radiation with different orientation in a laser cavity. The ray axis represents the direction of laser in whose path the birefringent filter is introduced and the optic axis of the filter lies in the plane of the filter. Figure 3.14 (a) has the filter placed perpendicular to the incident laser. The plate can be rotated by an angle $90^\circ - \theta$ about the y -axis so that the optic axis of the plate makes an angle θ with the ray axis. Figure 3.14 (c) shows a further rotation of the filter about its own axis by an angle ϕ . If $(90^\circ - \theta)$ is set equal to Brewster angle, the birefringent filter acts as a filter and polariser, rejecting s -polarised light at the exit of the crystal.

A proper analysis of polarisation based on Jones matrices as done in [29] reveals that the rotation of a birefringent filter in the Brewster plane as depicted above would result in varying intensity transmission which is a function of the incident wavelength, the thickness of the filter and the angle of rotation in the Brewster plane. The transmission is given by:

$$I_{TM} = 1 - \sin^2(2\phi) \frac{n_o^4 - n_o^2 \cos^2 \theta}{(n_o^4 - \cos^2 \phi \cos^2 \theta)^2} * \sin^2 \left(2\pi t \bar{\nu} \left\{ \frac{n_e \left[1 + \frac{\cos^2 \theta \cos^2 \phi}{n_e^2} - \frac{\cos^2 \theta \cos^2 \phi}{n_o^2} \right]}{\sqrt{\left[1 - \frac{\cos^2 \theta \sin^2 \phi}{n_e^2} - \frac{\cos^2 \theta \cos^2 \phi}{n_o^2} \right]}} - \frac{n_o}{\sqrt{\left[1 - \frac{\cos^2 \theta}{n_o^2} \right]}} \right\} \right) \quad (3.1)$$

where θ and ϕ are the angles as explained above, n_o and n_e are the ordinary and the extraordinary refractive indices and t is the thickness of the filter. The transmission becomes unity for all λ when $\phi = (m\pi)/2$, where m is an integer. The other condition for getting the intensity to be unity would be to have the bracketted quantity to be equal to integral multiples of π .

$$2t\bar{\nu} \left\{ \frac{n_e \left[1 + \frac{\cos^2 \theta \cos^2 \phi}{n_e^2} - \frac{\cos^2 \theta \cos^2 \phi}{n_o^2} \right]}{\sqrt{\left[1 - \frac{\cos^2 \theta \sin^2 \phi}{n_e^2} - \frac{\cos^2 \theta \cos^2 \phi}{n_o^2} \right]}} - \frac{n_o}{\sqrt{\left[1 - \frac{\cos^2 \theta}{n_o^2} \right]}} \right\} = m \quad (3.2)$$

The above quantity is a function of wavelength (or wavenumber), thickness and angle of rotation ϕ . Each different m gives us a different transmitted wavelength. The differentiation of the above function with respect to wavenumber would give us the free spectral range (FSR), the spacing between successive transmitted wavelengths.

$$FSR = \frac{d\bar{\nu}}{dm} = \frac{1}{dm/d\bar{\nu}} \quad (3.3)$$

$$FSR = \frac{1}{2t \left\{ \frac{n_e \left[1 + \frac{\cos^2 \theta \cos^2 \phi}{n_e^2} - \frac{\cos^2 \theta \cos^2 \phi}{n_o^2} \right]}{\sqrt{\left[1 - \frac{\cos^2 \theta \sin^2 \phi}{n_e^2} - \frac{\cos^2 \theta \cos^2 \phi}{n_o^2} \right]}} - \frac{n_o}{\sqrt{\left[1 - \frac{\cos^2 \theta}{n_o^2} \right]}} \right\}} \quad (3.4)$$

Thus a plot of FSR versus ϕ and λ would allow us to select the thickness and orientation of the birefringent filter that would help to tune our laser according to the wavelengths required and those we wish to suppress. Birefringent filters with different thickness and rotation of the optic axis in the Brewster plane provide the flexibility to allow and/or suppress a number of desired wavelengths. Fig 3.15 gives an idea of the change of transmission spectrum and location of transmission peaks on changing the rotation angle ϕ and thickness of the birefringent filter. Changing ϕ

tunes the position of the peaks, although the selectivity decreases if ϕ is too far away from 45° . A change of thickness t , changes the FSR. The transmission equation given by equation (3.1) can be used to find the appropriate thickness and rotation angle ϕ which would allow lossless transmission of any required wavelength.

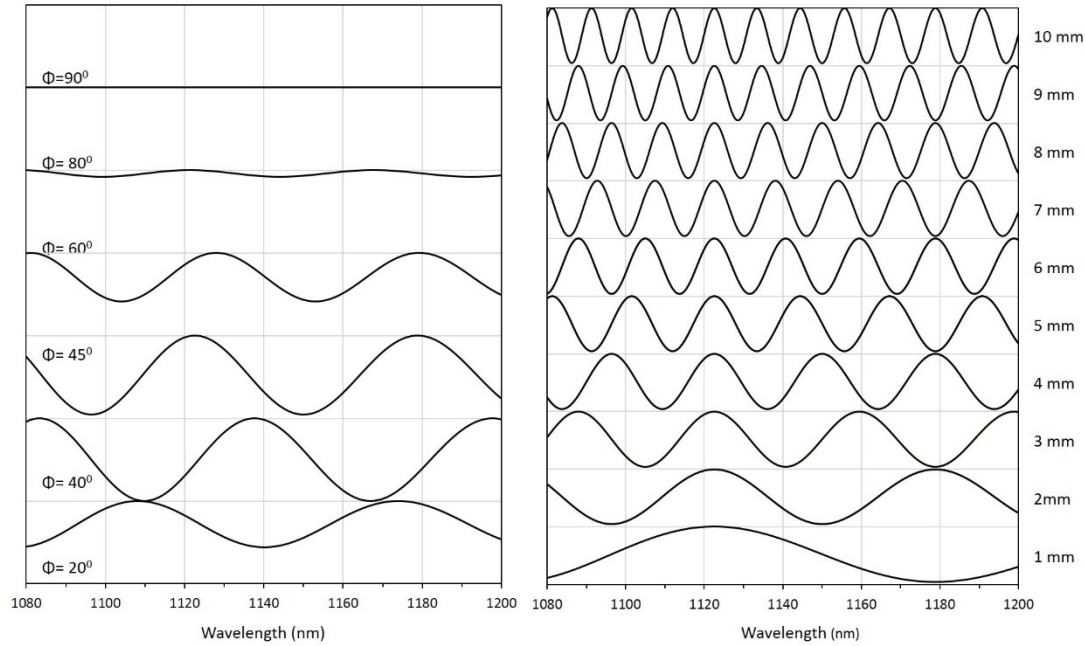


Fig. 3.15 Left: Variation of transmission of birefringent filter with change in rotation angle for a 2 mm thick MgF₂ birefringent filter. Right: Variation of transmission of birefringent filter with change in thickness, oriented at $\phi = 45^\circ$.

Thus to selectively control the wavelengths oscillating in the laser, we introduced a 2-mm-thick magnesium fluoride birefringent filter (BF) into the cavity, as shown in figure 3.8. Rotation of a 2 mm thick magnesium fluoride plate oriented at Brewster angle to the laser beam varied both the location of the transmission peaks as well as the free spectral range. For this filter, the free spectral range varied from 68 nm to 49 nm in this wavelength region as the angle of the optic axis with respect to the laser polarisation was varied between 25° and 72° .

Figure 3.16 shows the predicted transmission curves of a 2 mm thick magnesium fluoride birefringent filter. The black dashed curves in figure 3.16 are the

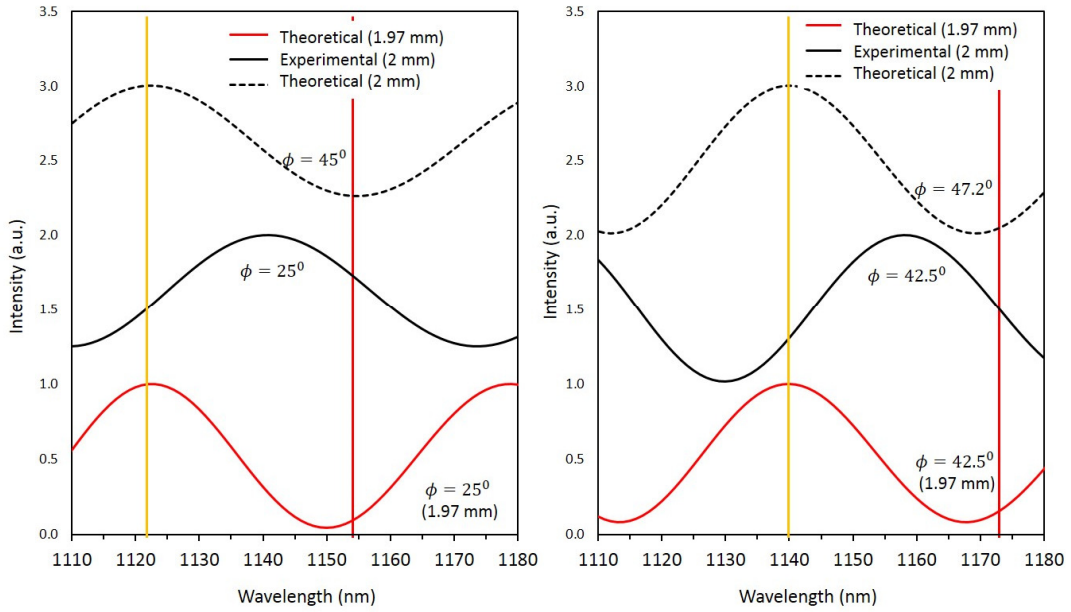


Fig. 3.16 Left: Transmission spectra of birefringent filters, predicted by theory and experimentally observed. The black dashed-curve is the theoretical transmission curve for pure forward and backward operation. The solid-curve is the transmission curve at the observed ϕ values for 2 mm birefringent filter. The red solid-curve represent the transmission curve of 1.97 mm birefringent filter at observed ϕ values. Left: For pure forward 1123 nm operation. Right: For pure 1140 nm operation. Also the cascaded wavelengths (1155 nm and 1174 nm can be seen to be prevented from lasing by the birefringent filter.

transmission spectrum with rotation angle $\phi = 45^\circ$ and $\phi = 47.2^\circ$ which would allow pure clockwise and pure counter-clockwise lasing according to equation (3.1). The experiment however showed in fact that we achieved pure clockwise and pure counter-clockwise lasing at $\phi = 25^\circ$ and $\phi = 42.5^\circ$ whose predicted transmission curves do not seem promising, shown by black solid graphs in figure 3.16. The difference in the predicted and experimentally observed is because the transmission curves have a very high dependence on the thickness of the birefringent filter, a change of 0.03 mm in thickness moved the maximum transmsission peak by approximately 10 nm. Thus we may conclude that the thickness of the birefringent filter that was used was not perfectly 2 mm and this was confirmed by measuring using a vernier calippers. The red solid graph represents the transmission curve for a 1.97 mm birefringent filter at the experimentally observed ϕ values (25° and 42.5°)

which seemed to give better prediction of pure 1123 nm and pure 1140 nm operation according to equation (3.1). The conclusion is that the prediction of ϕ is very sensitive to t (and n_o and n_e) and either the etalon thickness or the dispersion data is somewhat incorrect.

Laser behaviour with birefringent filter

At rotation angle $\phi = 25^\circ$, the laser gave pure clockwise output at 1123 nm with at a threshold of 2.6 W and a slope efficiency of 20 %. For a rotation angle $\phi = 42.5^\circ$, we achieved pure counter-clockwise output at 1140 nm with a threshold of 3.3 W and a slope efficiency of 15 % as shown in figure 3.17. While the uncontrolled multispectral laser (of section 3.4) generated a total of 0.25 W of power in the clockwise direction, the spectrally controlled laser generated single wavelength output with much greater output power of 0.45 W in the clockwise direction.

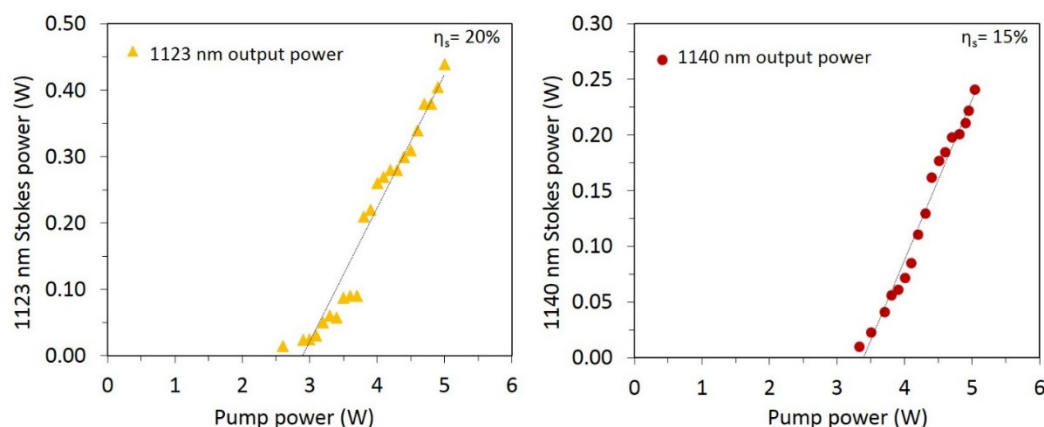


Fig. 3.17 Power transfer measurements for the spectrally controlled laser. Left: 1123 nm operation. Right: 1140 nm operation.

There was an increase in the threshold for the clockwise and counter-clockwise generation in the spectrally controlled laser. The clockwise generation had a threshold of 1.51 W for the uncontrolled laser while the controlled laser had a threshold of 2.06 W. Similarly the counter-clockwise generation had a threshold of 2.09 W for the uncontrolled laser while the controlled laser had a threshold of 3.33 W. The increased threshold can be attributed to losses induced by the

birefringent filter. Also The fact that birefringent filter induces different losses for different wavelengths thereby allowing selective lasing is clearly observed in the transmission curves of figure 3.16. Substantially higher maximum output power generation by the spectrally controlled laser, despite the additional losses induced by the birefringent filter, indicates an increased depletion of the pump pulses. This greater depletion of pump pulses can be attributed to constraining the cavity power to a single Stokes wavelength. Since the forward Stokes was cascaded into backward

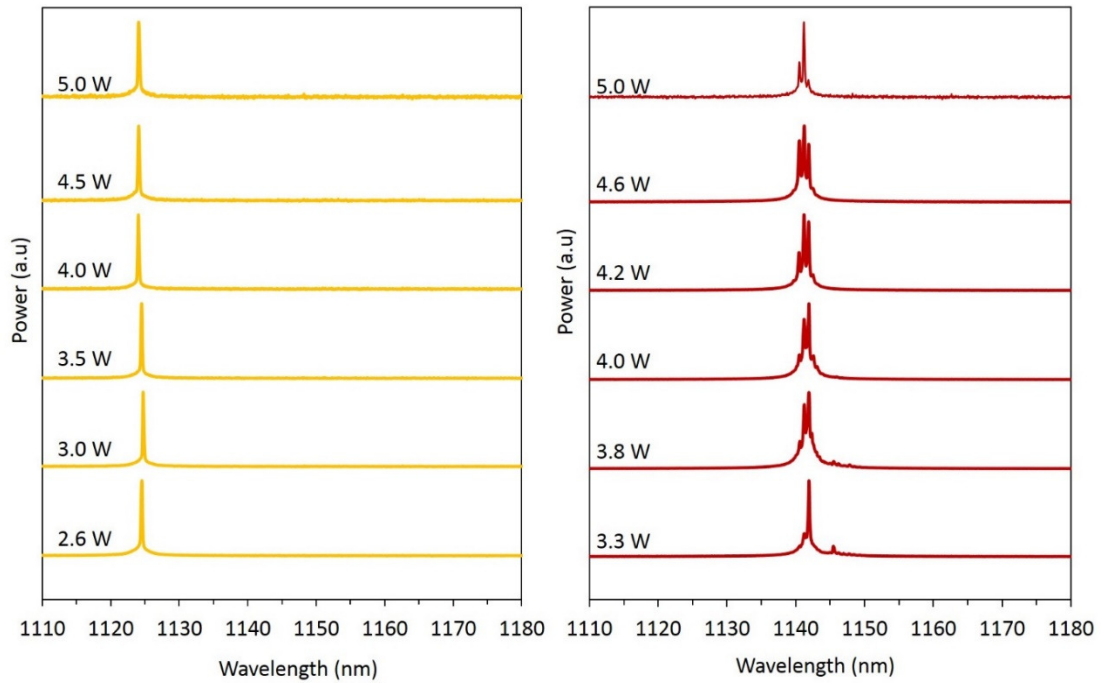


Fig. 3.18 Spectra at clockwise and counter-clockwise directions for the spectrally controlled laser with pump powers mentioned near respective spectra. Left: 1123 nm operation with $\phi = 25^\circ$. Right: 1140 nm operation with $\phi = 42.5^\circ$.

Stokes and vice-versa, constraining the laser to single Stokes generation made available the pump power for unidirectional operation causing better pump depletion.

The spectra of the Stokes generated at clockwise and counter-clockwise directions are shown in figure 3.18 recorded for different pump powers shown next to their respective spectrum. It can be clearly seen that the spectrally controlled laser

generated pure forwards Stokes (1123 nm) in the clockwise direction and pure backward Stokes (1140 nm) in the counter-clockwise direction. For the pure-1123 nm and pure-1140 nm cases, not only was the competing shift for 1064 nm suppressed, but also the cascading of the intracavity field by the 250 cm^{-1} shift was suppressed. We can see from figure 3.16 that the birefringent filter induced substantial losses for these cascaded wavelengths.

The pulse duration of the pure clockwise output was measured with an autocorrelator (FROG, MesaPhotonics) to be 22 ps at the maximum output power while the pulse duration measurement for counter-clockwise output was greater than 30 ps (measurement restricted by the instrument).

3.5.1 Controlled cascaded multiple wavelength generation

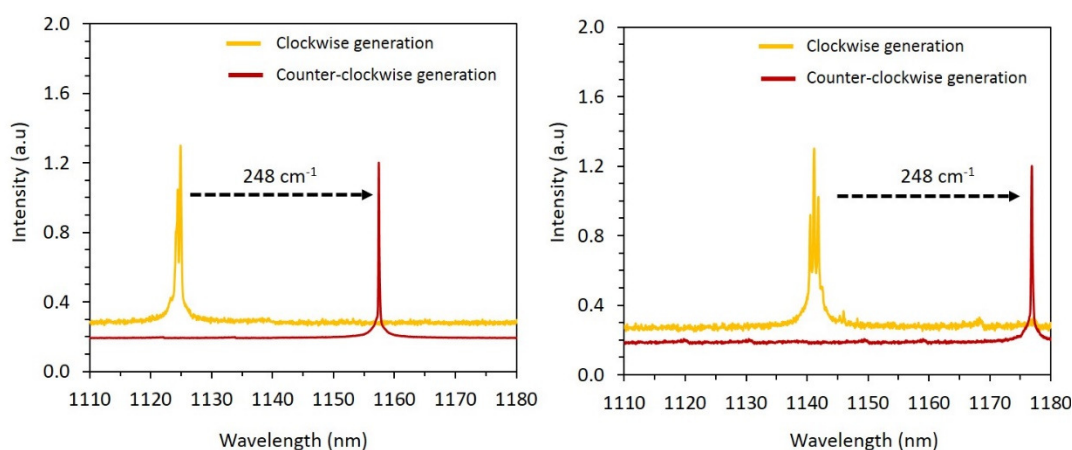


Fig. 3.19 Controlled cascaded Stokes generation in the spectrally controlled laser. Left: Pure forward Stokes generation in the clockwise direction and its cascading into counter clockwise direction. Right: Pure backward Stokes generation in the counter-clockwise direction and its cascading into clockwise direction. The dashed arrow represents backward shift.

With alternative orientations of the birefringent filter we could choose to allow cascading of the fields. A 72° rotation of birefringent filter generated 1123 nm and 1155 nm fields only; a 65° rotation generated 1140 nm and 1174 nm fields only. Figure 3.19 gives the spectrum of the above mentioned cases. The backwards- 248 cm^{-1} shift couples power from a field in one direction to a field in the

counter-propagating direction. Here with the tuning of birefringent filter we generate the clockwise 1123 nm field cascading to a counter-clockwise 1155 nm field; or alternatively the counter-clockwise 1140 nm field cascading to a clockwise 1174 nm field.

The transmission spectra a 1.97 mm thick birefringent filter for the cases are presented in figure 3.20. As seen from the figure, at a rotation of 72° the birefringent filter incurred losses for 1140 nm generation making available all the pump power for 1123 nm generation. The filter has high transmission for 1155 nm also which resulted in cascading of the cavity enhanced 1123 nm field. Similarly for a rotation of 65° , the filter applies loss for 1123 nm preventing its generation. At the same time the filter provides minimum loss transmission for 1140 nm generation and its cascaded Stokes of 1173 nm.

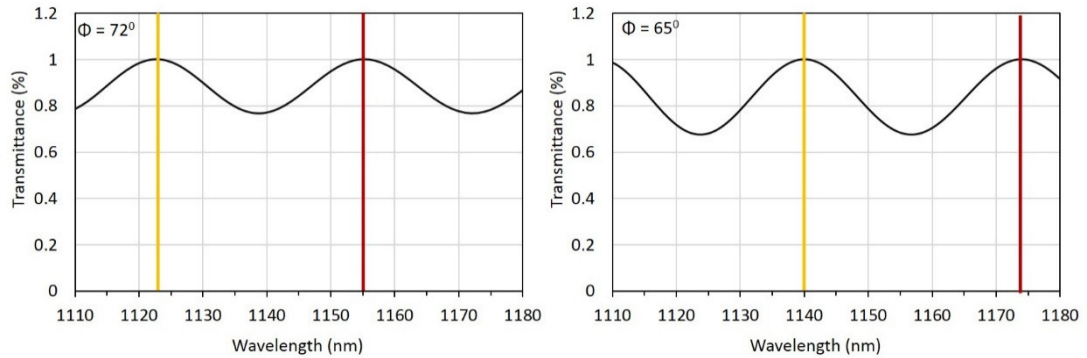


Fig. 3.20 Transmission curves of 1.97 mm MgF₂ birefringent filter for controlled cascaded Stokes generation. Left: $\phi = 72^\circ$ for 1123 nm and its cascaded 1155 nm generation. Right: $\phi = 65^\circ$ for 1140 nm and its cascaded 1173 nm generation.

These results thus demonstrate a spectrally controllable laser based on lithium niobate which can simultaneously convert the pump light into switchable and selectable Stokes of first order and second order.

It can be noted that in figure 3.12, there is evidence of a number of small shifts occurring on the 1123 nm and 1140 nm spectral lines, and this is also seen in the 1140 nm spectrum in figure 3.18. This shifting is due to stimulated polariton scattering (SPS) at near- 0° on the 248 cm^{-1} shift, corresponding to few-nm shifts. The

corresponding idler wavelengths are in the THz range (e.g. 0.2 THz for a 1 nm shift) presenting us with an excellent opportunity for terahertz wave generation. This method of cascading the cavity-enhanced Stokes fields as a simple and effective way to generate THz output from picosecond lasers is discussed in detail in the next chapter of this thesis.

3.6 Chapter Summary

We have developed a multiwavelength lithium niobate Raman laser which utilizes SRS and SPS in a synchronously pumped cavity. Lithium niobate, being a polar material, enable both Raman and Polariton scattering of the two strong vibrational modes with wavenumbers 628 cm^{-1} and 248 cm^{-1} . Polaritons, generated by coupling between optical and vibrational waves, take part in scattering the pump photons with the scattered frequency depending upon the angle between the pump and the Stokes fields and is determined by the phase matching curves.

The unique geometry of our laser system allowed only collinear generation of Stokes fields including forward and backward directions and generated wavelengths between 1110 nm and 1180 nm determined by the finesse of the cavity.

Forward scattering having a small wavevector mismatch between the pump and scattered waves generated polariton scattering and backward scattering having large wavevector mismatch resulted in Raman scattering. The polariton associated with the 248 cm^{-1} vibrational mode generated THz radiation for angles of a few degrees between the pump and Stokes fields and for angles $\gtrsim 7^\circ$ the polariton is predominantly vibrational in nature and tends to a resonant frequency of 248 cm^{-1} . The polariton associated with the 628 cm^{-1} vibrational mode has a resonant frequency of 497 cm^{-1} for co-propagating pump and Stokes; for angles $\gtrsim 7^\circ$ the polariton is predominantly vibrational in nature and tends to a resonant frequency of 628 cm^{-1} .

Due to the finesse of the cavity mirrors, cascading of the cavity enhanced first Stokes was supported. Or in other words, the cavity Stokes fields when become sufficiently

enhanced in intensity, were cascaded over generating second order Stokes wavelengths. The finesse of the cavity mirrors supported cascading by only backward Raman shift by 248 cm^{-1} . Thus we could observe four different wavelengths (1123 nm, 1140 nm, 1155 nm and 1173 nm) being generated by the system at maximum pump power.

In order to make the laser generate the multiple wavelengths in a controllable and selectable manner, a birefringent filter was used. The birefringent filter could introduce wavelength dependent losses providing us the flexibility of choosing the wavelength. This resulted in a spectrally controlled laser which could generate single wavelengths as well as pairs of them by controlled tuning of the birefringent filter. Thus we demonstrated controllable generation of four different output wavelengths from lithium niobate ultrafast Raman laser.

We could see that stimulated polariton scattering at small angles on the cavity enhanced Stokes fields, generated closely spaced Stokes lines. Also the idler frequencies involved in these small angle shifts fall in the terahertz regime of wavelength making an excellent possibility of terahertz wave generation from picosecond lasers with nanojoule scale energies. This would form the ground for the next chapter of this thesis.

3.7 References for Chapter 3.

- [1] V.G. Dmitriev, G.G. Gurzadyan, D.N. Nikogosyan, Handbook of nonlinear optical crystals, Springer, 2013.
- [2] G. Brodie, Y. Qiu, S. Cochran, G.C. Spalding, M.P. MacDonald, Optically transparent piezoelectric transducer for ultrasonic particle manipulation, IEEE Transactions on ultrasonics, ferroelectrics, and frequency control, 61 (2014) 389-391.
- [3] R.S. Weis, T.K. Gaylord, Lithium niobate: Summary of physical properties and crystal structure, Applied Physics A, 37 (1985) 191-203.
- [4] Y. Repelin, E. Husson, F. Bennani, C. Proust, Raman spectroscopy of lithium niobate and lithium tantalate. Force field calculations, Journal of Physics and Chemistry of Solids, 60 (1999) 819-825.
- [5] S. Bhagavantam, T. Venkatarayudu, Raman effect in relation to crystal structure, Proceedings Mathematical Sciences, 9 (1939) 224-258.
- [6] J.G. Scott, S. Mailis, C.L. Sones, R.W. Eason, A Raman study of single-crystal congruent lithium niobate following electric-field repoling, Applied Physics A, 79 (2004) 691-696.
- [7] W. Johnston Jr, I. Kaminow, Temperature Dependence of Raman and Rayleigh Scattering in LiNbO_3 and LiTaO_3 , Physical Review, 168 (1968) 1045.
- [8] A. Ridah, P. Bourson, M. Fontana, G. Malovichko, The composition dependence of the Raman spectrum and new assignment of the phonons in, Journal of Physics: Condensed Matter, 9 (1997) 9687.
- [9] N.V. Sidorov, A.A. Kruk, A.A. Yanichev, M.N. Palatnikov, B.N. Mavrin, Temperature investigations of Raman spectra of stoichiometric and congruent lithium niobate crystals, Optics and Spectroscopy, 117 (2014) 560-571.
- [10] I.S. Kuz'minov, Electrooptical and nonlinear optical lithium niobate crystals, Moscow Izdatel Nauka, 1 (1987).
- [11] N. Sidorov, T. Volk, B. Mavrin, V. Kalinnikov, Lithium Niobate: Defects, Photorefractive, Vibrational Spectrum, Polaritons, Science, Moscow, 255 (2003).
- [12] A. Blistanov, Crystals of quantum and nonlinear optics, Izdatelstvo MISIS, Moscow, (2000).

- [13] A. Rauber, Chemistry and physics of lithium niobate, *Current topics in materials science*, 1 (1978) 481-601.
- [14] N.V.e. Sidorov, P.G.e. Chufyrev, M.N. Palatnikov, N.N. Mel'nik, Y.A. Zheleznov, V.Y. Khomich, Manifestation of a photorefractive effect in Raman spectra of lithium niobate crystals of different compositions, *Quantum Electronics*, 34 (2004) 1177.
- [15] M.G. Pullen, J.J. Chapman, D. Kielpinski, Efficient generation of > 2 W of green light by single-pass frequency doubling in PPMgLN, *Applied Optics*, 47 (2008) 1397-1400.
- [16] H. Furuya, A. Morikawa, K. Mizuuchi, K. Yamamoto, High-beam-quality continuous wave 3 W green-light generation in bulk periodically poled MgO:LiNbO₃, *Japanese Journal of Applied Physics*, 45 (2006) 6704.
- [17] M. Ebrahimzadeh, P.J. Phillips, S. Das, Low-threshold mid-infrared optical parametric oscillation in periodically poled LiNbO₃ synchronously pumped by a Ti:sapphire laser, *Applied Physics B*, 72 (2001) 793-801.
- [18] R. Loudon, Theory of stimulated Raman scattering from lattice vibrations, *Proceedings of the Physical Society*, 82 (1963) 393.
- [19] A. Barker Jr, R. Loudon, Dielectric Properties and Optical Phonons in LiNbO₃, *Physical Review*, 158 (1967) 433.
- [20] H. Puthoff, R. Pantell, B. Huth, M. Chacon, Near-Forward Raman Scattering in LiNbO₃, *Journal of Applied Physics*, 39 (1968) 2144-2146.
- [21] J. Yarborough, S. Sussman, H. Purhoff, R. Pantell, B. Johnson, Efficient, tunable optical emission from LiNbO₃ without a resonator, *Applied Physics Letters*, 15 (1969) 102-105.
- [22] S.S. Sussman, Tunable light scattering from transverse optical modes in lithium niobate, in, DTIC Document, 1970.
- [23] J. Hopfield, Theory of the contribution of excitons to the complex dielectric constant of crystals, *Physical Review*, 112 (1958) 1555.
- [24] R. Pantell, H. Puthoff, Proposal to the Office of Naval Research for Continuation of Microwave Research under Contract Nonr 225(48), NR 373-361 for period 1

January 1965-31 December 1965, Microwave Laboratory Proposal, Stanford University, 1964.

[25] A.J. Lee, H.M. Pask, Continuous wave, frequency-tunable terahertz laser radiation generated via stimulated polariton scattering, *Optics Letters*, 39 (2014) 442-445.

[26] S. Kurtz, J. Giordmaine, Stimulated Raman scattering by polaritons, *Physical Review Letters*, 22 (1969) 192.

[27] D.J. Spence, E. Granados, R.P. Mildren, Mode-locked picosecond diamond Raman laser, *Optics Letters*, 35 (2010) 556-558.

[28] Y.N. Polivanov, Raman scattering of light by polaritons, *Soviet Physics Uspekhi*, 21 (1978) 805.

[29] D. Preuss, J. Gole, Three-stage birefringent filter tuning smoothly over the visible region: theoretical treatment and experimental design, *Applied Optics*, 19 (1980) 702-710.

[30] S. Kobtsev, N. Svetsitskaya, Application of birefringent filters in continuous-wave tunable lasers: a review, *Optics and Spectroscopy*, 73 (1992) 114-123.

4

Terahertz wave generation from an ultrafast Raman laser

In this chapter we present a terahertz wave generator based on cascading of cavity enhanced Stokes fields by Stimulated Polariton Scattering (SPS) in a lithium niobate crystal pumped by a picosecond laser with nanojoule scale energy. This is an extension of the laser presented in chapter 3. We first present some background on terahertz technology before presenting our observations.

4.1 Terahertz waves

Terahertz waves are the range of frequencies that fall between the frequencies most easily generated by optic and electronic technologies ranging from millimeter waves to far infrared with typically referred frequencies from 0.3 THz to 30 THz as seen in figure 4.1, taken from [1]. Since the wavelengths of terahertz radiation range from

1 mm, they are sometimes referred to as submillimeter waves. The name “terahertz” radiation was most commonly used and increasingly accepted for this frequency range following the use by J. W. Fleming [2].

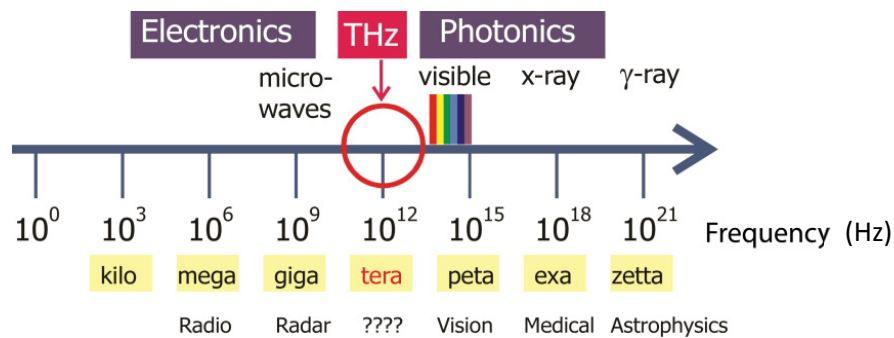


Fig. 4.1 THz radiation in the electromagnetic spectrum [1].

One of the earliest studies on terahertz radiation was likely done in the early 20th Century by Heinrich Rubens at the present Technical University of Berlin, whose research work was mainly concentrated on the extension of the infrared (IR) spectral region to longer wavelengths into what soon became called the far infrared (FIR) [3]. Some of his initial experiments were using prisms of rock salt, sylvine and fluorite extending the spectrum to nearly 20 μm . He and his colleagues employed method called ‘reststrahlen filter arrangement’ to extend the wavelength beyond 50 μm (6 THz) [3]. Over the century, generation of terahertz radiation has become a hot topic of research involving finding and developing new sources and methods of detection. Even though terahertz radiation has been long studied in astronomy and analytical science fields, it is the recent technological advancement in the fields of photonics and nanotechnology that has taken the application to a wider arena. Some of the arising fields of application for terahertz radiation include information and communications technology (ICT); biology and medical sciences; non-destructive evaluation; homeland security; quality control of food and agricultural products; global environmental monitoring; and ultrafast computing. There are many applications in the field of defence and security as well. Particularly in medical imaging applications terahertz waves have the advantage of low photon-energy and non-ionizing nature, unlike X-rays, making it safe for tissues and DNA. Both imaging

as well as spectroscopic systems have been developed, and there is continuous demand for improvement of performance and capabilities of detectors and sources.

With the immense applications needing terahertz radiation, a great amount of research is focused on possible terahertz sources. The available sources can be divided into three major types: optical terahertz generation, terahertz quantum cascade lasers (QCL) and solid-state electronic devices. Figure 4.2 summarises the different terahertz emission power across the frequency range [4] including IMPATT (impact ionization avalanche transit-time diode) [5], MMIC (microwave monolithic integrated circuit) [6] and TUNET (tunnel injection transit sources) [7].

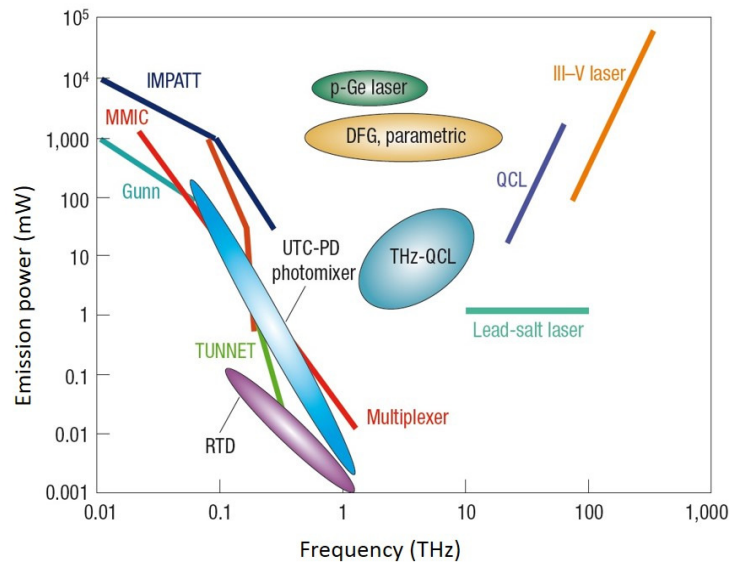


Fig. 4.2 THz emission power as a function of frequencies [4]. IMPATT stands for impact ionization avalanche transit-time diode, MMIC denotes microwave monolithic integrated circuit, TUNET stands for tunnel injection transit sources. Lines represent conventional sources, ovals represent relatively recent sources.

Terahertz generation by optical methods can be generally categorized into two types: One involving ultrafast photocurrent generation in photoconductive switch or semiconductors, and the other involving nonlinear processes like optical rectification [8] mostly done using femtosecond lasers, difference frequency generation [9] or parametric scattering [10, 11] from nonlinear media like GaAs, GaSe, Gap, ZnTe, CdTe and LiNbO₃. Extensive reviews about terahertz wave generation and applications can be found in [1, 4, 12-15]

Tunable terahertz sources are of great importance with a wide range of applications such as material science, gas tracing, material testing etc. Novel tunable sources with high temporal and spatial coherence already exist in sub-THz region, such as the backward-wave oscillator (BWO). Scarcity of tunable terahertz sources above 1 THz, where the effectiveness of BWO sources reduces, have made it a hot topic of research for new source development.

4.2 Parametric generation of terahertz waves by polaritons

A few decades ago, research work was first carried out on the creation of tunable coherent far-infrared radiation based on optical phenomenon [13, 16, 17]. Figure 4.2 gives a graphical representation of different terahertz sources at different frequencies. Pantell and Puthoff and others have reported efficient tunable terahertz generation [18-20] based upon tunable scattering from materials which are both Raman and infrared active. In such systems, an input pump photon excites the lattice vibrations generating a signal photon with frequency shifted from the pump frequency by the lattice vibration. The lattice vibrations generate idler frequencies due to the vibration of the polar lattice. The photon and phonon wave fields couple and behave as a new mixed photon-phonon mode. Efficient generation of terahertz waves traces its origin from parametric scattering of these mixed mode called polaritons and is widely observed in polar crystals like LiNbO_3 , LiTaO_3 , and GaP which are both infrared-active and Raman-active. Thus polariton scattering involves both second and third order nonlinear processes modifying the dispersion relationship.

The modified dispersion relationship allows tunability of the idler wave generated (in the terahertz frequency range for parametric scattering) by changing the angle of interaction between the pump and the signal frequencies. The terahertz wave generator presented in this chapter is thus a step in the direction of generating tunable terahertz frequencies from nanojoule scale picosecond lasers.

In the last three decades, lithium niobate has been extensively studied for terahertz wave generation due to its large nonlinear coefficient ($d_{33} = 25.5 \text{ pmV}^{-1}$ for $\lambda = 1064 \text{ nm}$) and its transparency over a wide range of wavelengths (0.4 to

5.5 μm) [21]. Lithium niobate is known to have four A_1 symmetry modes which are both infrared and Raman active out of which the lowest mode ($\omega_o = 248 \text{ cm}^{-1}$) is useful for efficient terahertz generation, due to its large parametric gain as well as smallest absorption coefficient [22].

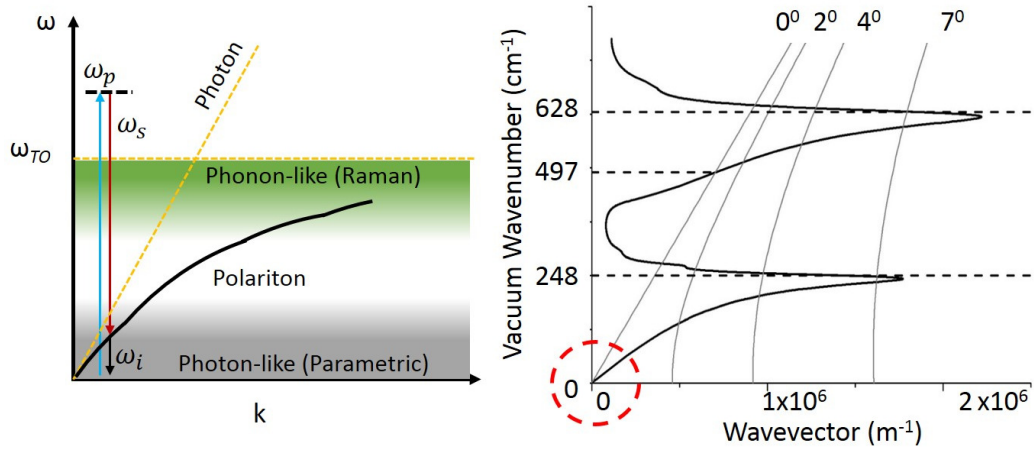


Fig. 4.3 Left: Dispersion curve of an infrared active optical vibrational mode of a crystal in the region below the vibrational resonant frequency showing the photon, polariton and phonon nature. Right: Dispersion curve of lithium niobate with phase matching curves for small angle scattering of 1064 nm pump laser. Dashed red circle denotes small angle scattering.

Figure 4.3 shows the modification of the dispersion curve of a polar crystal as well as the dispersion curve of lithium niobate for a pump of 1064 nm. The polar nature modifies the dispersion curve resulting in an angular dependence for the scattered frequencies determined by the angle of interaction between the pump and the Stokes fields. The scattering is also subjected to energy (ω) and momentum (k) conservation requiring satisfaction of phase matching conditions. Hence only those frequencies corresponding to the intersection of the dispersion curve and the phase matching curves take part in the scattering process.

The small angle scattering off the lowest vibrational modes are photon like in nature, as seen in figure 4.3 (Left) and undergo parametric scattering, a $\chi^{(2)}$ interaction. Small angle scattering on the 248 cm^{-1} modes result in coupling the pump frequency

into closely-spaced Stokes fields along with the generation of idler frequencies in the terahertz frequency range. For example shifting the pump frequency over a range of 1 cm^{-1} to 100 cm^{-1} can generate terahertz frequencies from 0.2 to 3 THz.

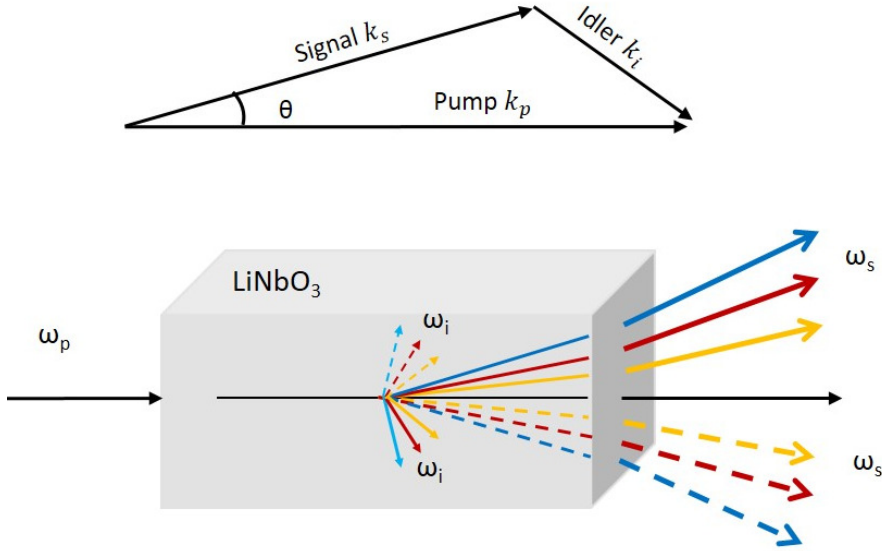


Fig. 4.4 Top: Wave-vector triangle for non-collinear phase matching condition. Bottom: Signal (Stokes) and Idler (terahertz) generation with dashed and solid lines forming separate pairs. A cross-sectional view.

Thus due to angle-dispersive characteristics of the signal (Stokes) and idler (terahertz) waves, broadband tunable generation of terahertz waves is possible depending upon the phase-matching angle between the pump and the signal. Figure 4.4 gives a pictorial representation of the frequencies that take part in the parametric scattering of polariton at small angles.

The top of figure 4.4 represents the wave-vector triangle for non-collinear phase matching. Parametric scattering collinear with the pump laser, has the idler frequency and the gain approaching zero. Hence the Stokes fields need to be generated at small angles to the pump laser as depicted in the bottom of figure 4.4 which is a cross-sectional view of a single pass terahertz generator (TPG). Each pair of Signal and idler frequencies generated at different small angles are represented with different colours. Note that the conservation laws allow Stokes and idler

frequencies to be generated on both sides of the pump beam which is depicted by solid and dashed arrows forming separate pairs. This generation of signal-idler pairs is possible symmetrically about the pump laser direction, but one plane is preferred determined by the optic axis direction and pump laser polarisation, discussed later in this chapter.

4.3 Theory of Terahertz Parametric Generation (TPG)

A single pass terahertz convertor called a terahertz parametric generator (TPG) discussed above is analogous to an optical parametric generator (OPG) for a pure $\chi^{(2)}$ process. A terahertz parametric generator usually generates broadband (linewidth typically about 1 THz) terahertz waves by a single-pass pumping [13]. Several applications such as tomographic imaging, interferometric spectroscopy, and diffuse reflection spectroscopy, prefer broadband sources over narrower linewidth sources (terahertz parametric oscillators, injection-seeded TPG etc.). Also many industrial applications such as transmission imaging for materials or food inspection have wide application for TPGs.

The parametric gain coefficients of the idler (terahertz) and the signal (Stokes) waves can be obtained by solving the classical coupled-wave equations that describe this process. Assuming steady-state with no pump depletion, the coupled equations are obtained as [22-24]:

$$\left(\nabla^2 + \frac{\omega_s^2}{c^2} (\varepsilon_s + \chi_R |E_p|^2) \right) E_s = -\frac{\omega_s^2}{c^2} \chi_p E_p E_i^* \quad (4.1)$$

$$\left(\nabla^2 + \frac{\omega_i^2}{c^2} \varepsilon_i \right) E_i = -\frac{\omega_i^2}{c^2} \chi_p E_p E_s^* \quad (4.2)$$

where ω_s, ω_i denotes the signal (Stokes) and the idler (terahertz) frequencies respectively, $\varepsilon_s, \varepsilon_i$ represents the signal (Stokes) and the idler (terahertz) permittivity in lithium niobate and c , the velocity of light in vacuum. The effective nonlinear susceptibilities of parametric and Raman processes are represented by χ_p and χ_R . The analytical expressions for the signal (Stokes) and the idler (terahertz) can be

obtained by solving equations (4.1) and (4.2) using the plane wave approach to give gains for signal (g_s) and idler (g_i) [22-24].

$$g_i = g_s \cos \phi = \frac{\alpha_i}{2} \left\{ \left[1 + 16 \cos \phi \left(\frac{g_o}{\alpha_i} \right)^2 \right]^{(1/2)} - 1 \right\} \quad (4.3)$$

where ϕ is the phase matching angle between the pump and the terahertz wave. g_o is the low-loss limit and α_i is the absorption coefficient in the terahertz region given by:

$$g_o = \sqrt{\frac{\pi \omega_i \omega_s I_p}{2 c^3 n_i n_s n_p}} \cdot (\chi_p) \quad (4.4)$$

$$\alpha_i = 2[Im k_i] = \frac{2\omega}{c} Im \left(\varepsilon_\infty + \frac{S_o \omega_o^2}{\omega_o^2 - \omega_i^2 - i \omega_i \Gamma_o} \right)^{\frac{1}{2}} \quad (4.5)$$

Observations by J. Shikata *et. al.* [25, 26] have found terahertz generation can be increased to a great extent by cooling the crystal which could enhance the parametric gain g_i and reduce the absorption loss α_i at terahertz frequencies. Figure 4.5 shows the gain coefficient of parametric terahertz wave generation in the terahertz frequency range of 1 to 3 THz from [13]. The parametric gain is enhanced with increasing pump intensity as well as with cooling of the crystal.

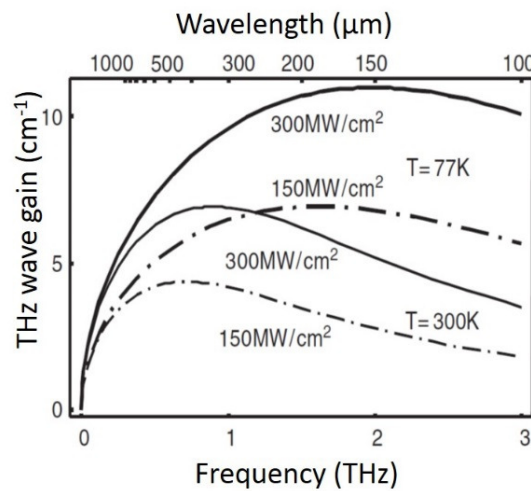


Fig. 4.5 The gain coefficient of terahertz generation in lithium niobate pumped by 1064 nm which gets enhanced on cooling [13]. The solid and dashed graphs represent gain at different pump intensities at a single temperature.

4.4 Terahertz Parametric Oscillators and extraction of terahertz waves

Enhanced generation of a coherent terahertz wave can be achieved by introducing an optical cavity around the generating crystal to resonate the signal and so form a terahertz parametric oscillator (TPO). Tunable terahertz waves are generated by changing the angle between the pump beam and the signal. A basic configuration (external cavity) of a TPO is shown in figure 4.6 where a resonator is provided for the signal waves generated. On rotating the resonator with respect to the pump beam, a tunable terahertz wave is generated. The change of angle results in different signal wave generation and hence different terahertz wave generation. An array of silicon prisms are used to couple out the generated terahertz waves as the lithium niobate has large refractive index for terahertz waves causing it to undergo total internal reflection without the prisms.

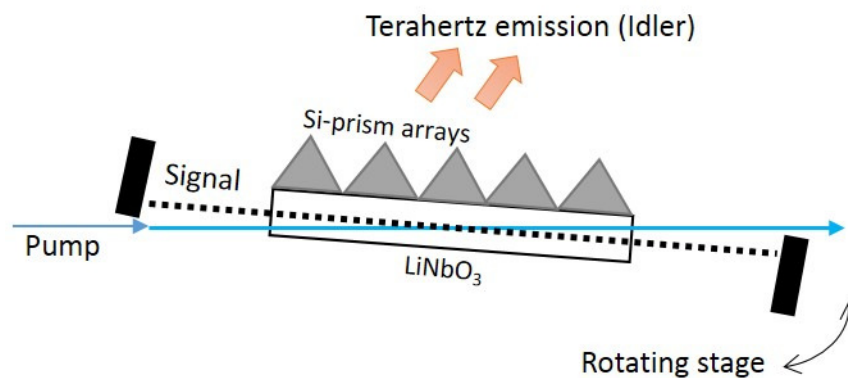


Fig. 4.6 A typical terahertz parametric oscillator configuration with resonator for the signal fields. The mirrors and the crystal are installed on a stage turning which the angle of interaction of pump and signal beams are changed.

A series of smaller silicon prisms have been found to be more efficient than a single silicon prism owing to significant absorption of silicon in the terahertz region. Kawase *et. al.* observed a six-fold increase in the coupling efficiency and a 40 % reduction in the far-field diameter when a series of prism were used compared to using single prism output coupling. The surface of the crystal and the base of the silicon prisms are polished to achieve a close contact allowing maximum coupling of the terahertz waves through the interface. The pumped region inside the lithium

niobate crystal must be as close as possible to the silicon array, because of the large absorption coefficient of lithium niobate crystals in the terahertz range. The prisms were attached to the crystal by using few drops of ethanol which provided good contact.

Lithium niobate crystals with a “cut-end” configuration [27] are also employed to couple out the terahertz so that the problem of total internal reflection is avoided. In such a configuration, the lithium niobate crystal has a cut at the corner and the generated terahertz waves emerge approximately normal to the exit surface. Using a grating surface for the crystal is yet another efficient method of coupling out the terahertz waves [28, 29]. The surface of the crystal is precisely machined to have a grating which acts as a coupler to prevent total internal reflection.

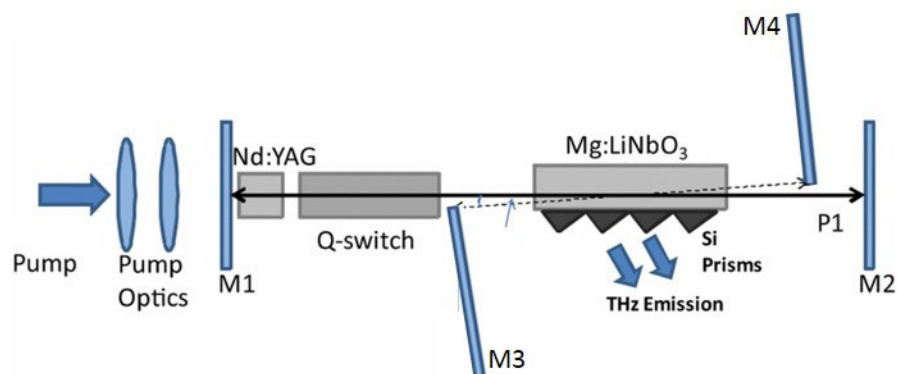


Fig. 4.7 Schematic of an intracavity terahertz parametric oscillator with terahertz generating material placed inside the pump laser cavity, from [31].

One can also place the terahertz cavity inside the cavity of the pump laser to demonstrate an intracavity TPO. Edwards *et. al.* reported such intracavity TPOs in [30]. Recently Andrew *et. al.* also demonstrated intracavity terahertz generation in both continuous and pulsed (ns) pumping schemes in [31] and [32] respectively. The intracavity configuration includes a separate, angle-tunable, cavity around the terahertz generator crystal inside the cavity of the pump laser to resonate the near-infrared Stokes fields generated through SPS [32]. A general schematic of the intracavity configuration is shown in figure 4.7.

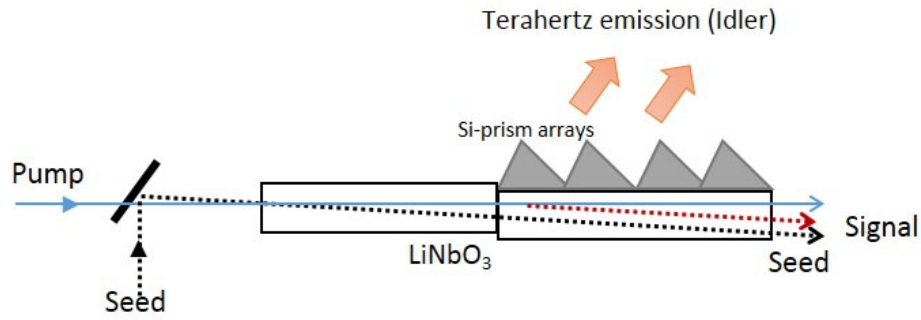


Fig. 4.8 Injection seeded terahertz parametric generator where a signal wavelength is provided in addition to the pump wavelength [33].

For wider tunability of the terahertz waves, injection seeding as seen in figure 4.8 is incorporated in TPGs where in addition to the pump wavelength, an injection seed for the signal waves is provided. By tuning seeding laser, wide tunability is achieved for the generated terahertz waves. Hayashi *et. al.* used a continuous wave tunable diode laser (1066 nm to 1074 nm) as an injection seed for the signal waves and could obtain a wide tunability from 125 μm to 430 μm (0.7 to 2.4 THz) in lithium niobate pumped by a single longitudinal mode Q-switched Nd:YAG laser (1066 nm; 15 ns) [33]. The authors observed that maximum terahertz generation was obtained when two MgO-doped lithium niobate crystals were used instead of one. One crystal acts as the amplifier while the second one generates the terahertz waves.

Kawase *et. al* [13] observed a 300 times higher terahertz generation with the injection seeding than just a conventional TPG. A maximum terahertz wave output of 1.3 nJ was observed with 34 mJ of pump energy and a seed of 50 mW. In addition

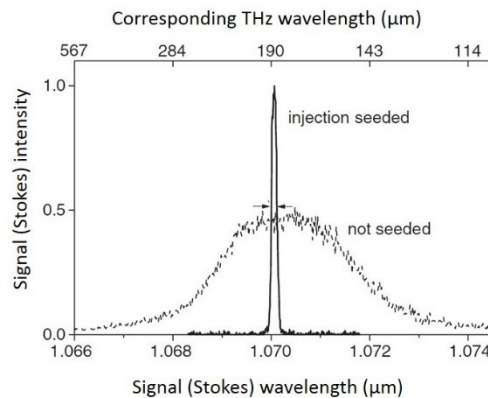


Fig. 4.9 Spectral narrowing for signal (Stokes) beams generated in an injection seeded TPG. [13]

to achieving wider tunability for terahertz generation, injection seeded TPGs produced a narrower spectrum than the non-seeded case as seen in figure 4.9.

4.5 Terahertz generation by Optical Rectification

Optical rectification involves terahertz wave generation in a nonlinear medium via difference frequency generation (DFG) between different frequencies contained within the pulse spectrum of an ultrafast pulse. This method was first demonstrated in a lithium niobate crystal pumped by a picosecond laser [34, 35] and ZnTe, ZnSe, CdS and quartz [34] crystals. Terahertz generation by optical rectification was later demonstrated by femtosecond pump lasers which made it possible to generate much broader bandwidths in the terahertz region [1, 36]. Thin crystals of the order of few millimetres are used for broadband terahertz generation due to constraints like mismatch between pump pulse group velocity and terahertz phase velocities, and absorption of crystals in the terahertz range. The optical-to-terahertz conversion efficiencies observed by the simple rectification method are only of the order 10^{-6} to 10^{-9} [37]. However higher conversion efficiency of $\sim 5 \times 10^{-4}$ was observed in lithium niobate by tilting the intensity front of a 800 nm femtosecond pump pulse to match the polariton phase velocity to the pump group velocity generating near single-cycle terahertz pulses with an average energy of 100 μJ [38].

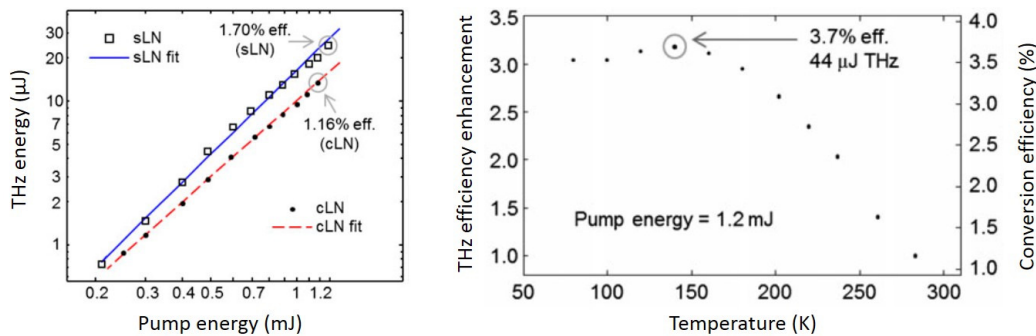


Fig. 4.10 Left: Pump energy conversion of stoichiometric and congruent lithium niobate crystals at room temperature. Right: Enhanced optical to terahertz conversion efficiency on cooling of congruent lithium niobate crystals, taken from [39].

Recently, using this technique, a highly efficient terahertz generator based on an optical rectifier was reported by Huang *et. al.* [39] in lithium niobate pumped by a femtosecond laser. At room temperature the stoichiometric lithium niobate crystal generated terahertz waves with a conversion efficiency of 1.7 % while the congruent lithium niobate crystal had a conversion efficiency of 1.16 %. The conversion efficiency was enhanced in the congruent crystal by cryogenic cooling which gave a conversion efficiency of 3.7 % compared to 1.16 % at room temperature as seen in figure 4.10. The authors observe that optical-to-THz conversion efficiencies of 10% are potentially achievable enabling the production of multi-millijoule terahertz pulses from a 100 mJ pump source, which has excellent applications such as to drive a compact next-generation linear accelerator and free electron laser.

4.6 Terahertz generation from quasi-phase matched crystals

Traditional collinear phase matching necessitates light propagation through the crystal in a direction where the natural birefringence of the crystal results in the weighted refractive index of input waves being equal to the refractive index of generated waves. If the phase relationship between the input and generated photons is not maintained throughout the crystal, destructive interference between the generated photons reduces the nonlinear conversion efficiency. As the terahertz index in lithium niobate is significantly mismatched to the IR index, alternative phase matching techniques are required. Periodical poled crystals, where the orientation of the nonlinear crystal is inverted at regular intervals, are engineered to attain quasi-phase matching which prevents this destructive interference. In other words, crystals with periodic variation of the sign of the $\chi^{(2)}$ nonlinear coefficient conserves the k vector in optical-to-terahertz conversion via quasi-phase matching allowing collinear generation. By choosing the correct periodicity, high conversion efficiency can be achieved. Quasi-phase-matching by propagation through periodically poled material [40-46] has achieved efficiencies of up to 0.045 %.

Miyamoto *et. al.* [47] used two periodically poled stoichiometric lithium tantalate crystals (PPSLT) pumped by a picosecond Nd:YVO₄ bounce laser with pulse width of

6.4 ps to generate dual frequencies close to $1.5\ \mu\text{m}$, by controlling the size and temperature of the crystals. These generated dual frequencies were made to undergo difference frequency generation by collinear phase matching in a 4'-dimethylamino-N-methyl-4-stilbazolium-tosylate (DST) crystal to generate terahertz waves tunable in the range 2.1 to 7.1 THz with a maximum peak power of 180 mW.

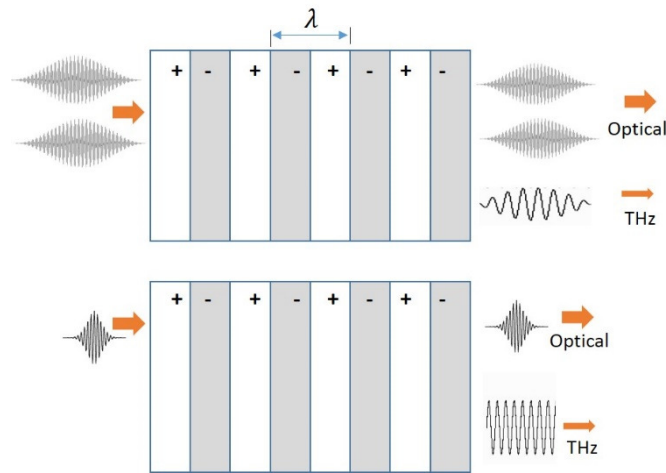


Fig. 4.11 Schematic illustration of collinear terahertz generation in quasi-phase-matched crystals. *Top*: Difference frequency generation with picosecond pulses. *Bottom*: Optical rectification geometry with femtosecond pulses.

Periodically poled lithium niobate crystals are also used in the optical rectification configuration to achieve enhanced conversion efficiencies. Optical rectification in quasi phase matched crystals was first demonstrated in PPLN pumped by a femtosecond laser obtaining a narrowband terahertz generation with $\sim 10^{-5}$ conversion efficiency [48]. The PPLN crystals have also been employed in surface emitting configurations using optical rectification (OR) of femtosecond pulses [49] as well as difference frequency generation (DFG) by picosecond pulses [50] as depicted in figure 4.11.

4.7 Terahertz wave generation in enhancement cavities

In conventional TPOs/TPGs, the pump power passes through the medium only once and is then dumped as a waste beam. This dumped beam doesn't contribute further to the parametric process resulting in a very high threshold for terahertz generation.

Enhancement cavities are optical resonators which cause resonant enhancement of optical power. The intracavity power becomes far above the pump power when the cavity length is made equal to an integer multiple of the pump wavelength. The finesse of the cavity determines the maximum enhancement. But to couple laser power into a cavity, the cavity length must be a multiple of the wavelength and controlled to a small fraction of wavelength, commonly known as resonance locking. When cavity enhancement resonators are pumped by mode-locked lasers, the cavity also has to be chosen in such a way that the cavity round-trip time is an integer multiple of the pulse spacing, so that all modes of the pump laser are also cavity modes.

Resonant locking, by controlling the cavity length is achieved by employing fine tuning of the mirror positions using some feedback mechanism. One of the methods used for such resonance locking is called HC stabilization using a quarter-wave plate, polarisation beam splitter, a pair of photodetectors and a differential amplifier [51]. Displacement of one of the cavity mirrors mounted on a piezoelectric transducer is controlled by the error signal generated by the method via a servo loop. This is in contrast to synchronous pumping in which the cavity has a low finesse at the pump wavelength and the pump field is not enhanced. Most of the terahertz parametric oscillators pumped by picosecond mode-locked lasers use the enhancement

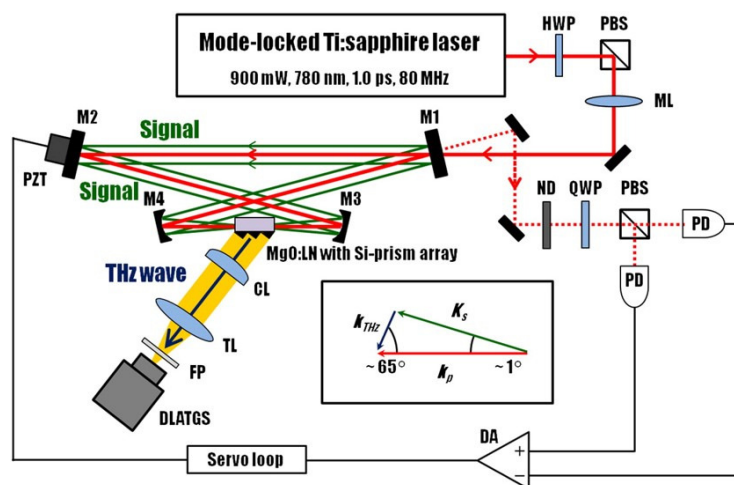


Fig. 4.12 Experimental setup of [11] demonstrating the resonant enhancement cavity design with piezo actuator and complex feedback electronics based on HC stabilisation method.

resonator design to reduce the terahertz generation threshold. Takida *et.al.* reported a resonator enhanced terahertz parametric oscillator pumped by a mode-locked picosecond Ti:sapphire laser (900 mW, 1 ps, 80 MHz) in a lithium niobate crystal [11] in an external enhancement cavity doubly resonant for both pump (780 nm) and signal (781 nm to 784 nm) as shown in figure 4.12. Terahertz output of 170 nW at 0.9 THz was generated. The enhancement cavity here realised the possibility of efficient terahertz generation based on parametric process from a low power pumping source with a pulse energy typically less than 100 nJ per pulse.

The same authors could generate a tunable terahertz source, using the same type of enhancement resonant cavity, using two different shapes of unpoled MgO-doped lithium niobate crystals: a rectangular crystal with silicon prism output coupling and a trapezoid for surface-emitted configuration [10] as shown in figure 4.13. The tunability of terahertz generation was obtained by fine translation of one of the cavity mirrors which resulted in shifting the peak wavelength of the oscillating signal from 781.9 nm to 786.9 nm, corresponding to a tunability in the frequency range of 0.9 THz to 3.3 THz. This tuning range is close to that of conventional nanosecond TPOs [13].

The authors observed that above 2 THz, the THz-wave output of surface-emitting crystal configuration is enhanced several times more than the silicon prism configuration due to suppression of absorption losses in the lithium niobate crystal.

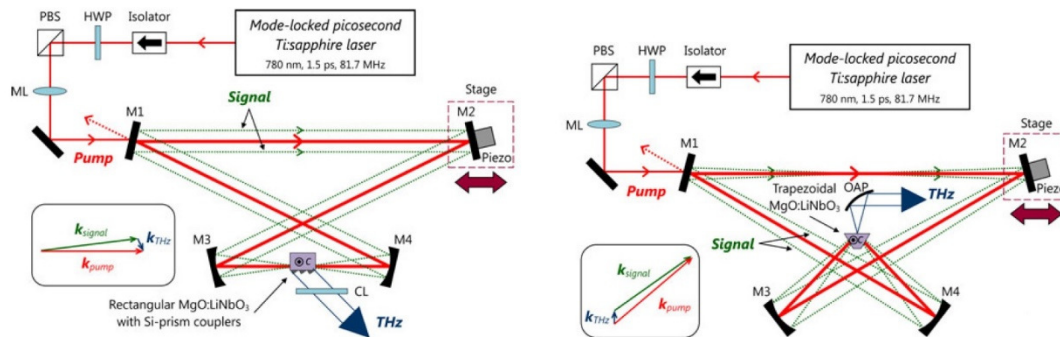


Fig. 4.13 Experimental setup of [10] using (a) silicon prism coupled TPO and (b) surface-emitting ps-TPO. The inset shows the non-collinear phase matching condition. Both the configurations employ a resonant enhancement cavity for the pump employing piezo actuators and complex feedback electronics.

In the silicon prism coupled configuration, a maximum terahertz power of 20 nW at 2 THz was obtained. The terahertz output power decreased rapidly for higher frequencies (> 2 THz) owing to strong absorption of terahertz waves by lithium niobate. The surface emitting configuration however could minimise the absorption generating about 40 nW at 2 THz. Cryogenic cooling [52], as mentioned in 4.4, also has the potential not only to suppress the absorption at higher frequencies, but also enable higher power scaling at lower frequencies.

Hence resonance enhancement cavities form an efficient platform for terahertz generation where the pump and signal (Stokes) frequencies are both resonated, with the cavity length maintained at integral multiples of the pump wavelength and controlled to a small fraction of the wavelength using proper feedback electronics.

4.8 Terahertz wave generation from an ultrafast LiNbO₃ Raman laser

Our synchronously pumped lithium niobate Raman laser could generate switchably and simultaneously four different wavelengths from the Nd:YVO₄ pump laser by utilizing SRS and SPS. The confocal ring cavity used in the setup allowed only collinear generation of Stokes fields including the co-propagating fields generating clockwise Stokes and counter-propagating fields generating counter-clockwise Stokes.

Controlled by the finesse of the mirrors used, the pump power was transferred to a shifted cavity field by either a 497 cm^{-1} shift, associated with forward polariton scattering or by a 628 cm^{-1} shift associated with backward Raman scattering. The 1123 nm Stokes field generated by the forwards- 497 cm^{-1} shift propagated clockwise in the ring cavity while the 1140 nm Stokes field generated by the backwards- 628 cm^{-1} shift propagated counter-clockwise in the ring cavity. Introducing a birefringent filter in the cavity helped to selectively control the wavelengths oscillating in the laser resulting in the realisation of pure forward and pure backward Stokes laser based on lithium niobate crystal.

The polariton associated with the 248 cm^{-1} vibrational mode generates terahertz radiation for angles of a few degrees between the pump and Stokes fields. The terahertz shift couples power into closely-spaced Stokes wavelengths co-propagating

with the generating field. This was clearly observed in the spectra of 1123 nm and 1140 nm generation in the lithium niobate Raman laser. This is shown in figure 4.14.

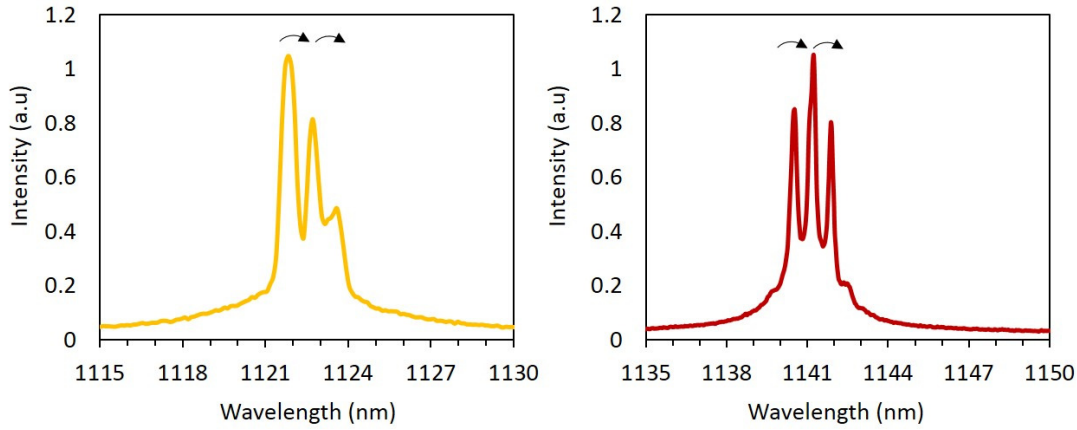


Fig. 4.14 Spectrum of clockwise (left) and counter-clockwise (right) Stokes wavelengths with the Stokes fields being shifted to closely spaced Stokes fields by the polariton (THz) shift.

The polaritons are predominantly photonic in nature at these low frequencies, and the idler waves generated in this parametric scattering fall in the terahertz regime; for example a Stokes fields shifted by 1 nm we get idler waves of 0.2 THz. Note that the coupling of the pump to a cavity-enhanced Stokes field plays the same role as resonant enhancement of the pump itself in resonant TPOs. By using SRS or SPS to couple to a cavity-enhanced field, we avoid the need for precise control of the cavity length that is required for resonant locking. Instead we just need the cavity to be matched sufficiently for synchronous pumping with a tolerance of order of 10 μm . This method of terahertz cascading the cavity-enhanced Stokes fields could be a simple and effective way to generate terahertz output from picosecond lasers with nanojoule scale energies, avoiding the need for resonant enhancement cavities.

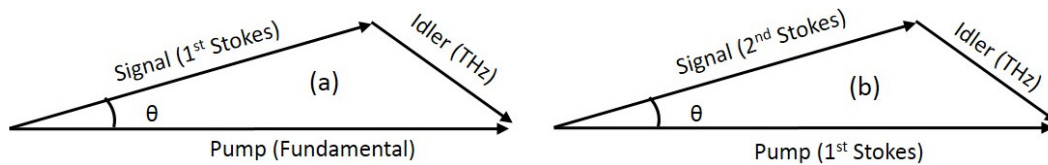


Fig. 4.15 Pump, signal, idler waves: (a) in conventional terahertz generation setups; (b) in our present system.

The conventional parametric scattering of polaritons used for terahertz wave generation involves the pump field getting shifted to near-infrared Stokes field generating terahertz in the process. Unlike that, here the terahertz waves get generated by parametric scattering of cavity enhanced Stokes fields into closely spaced higher order Stokes fields. Thus in our laser system, with regards to the terahertz radiation, the first Stokes becomes the pump, the closely spaced second Stokes fields become the signal and the terahertz itself is the idler as seen in figure 4.15.

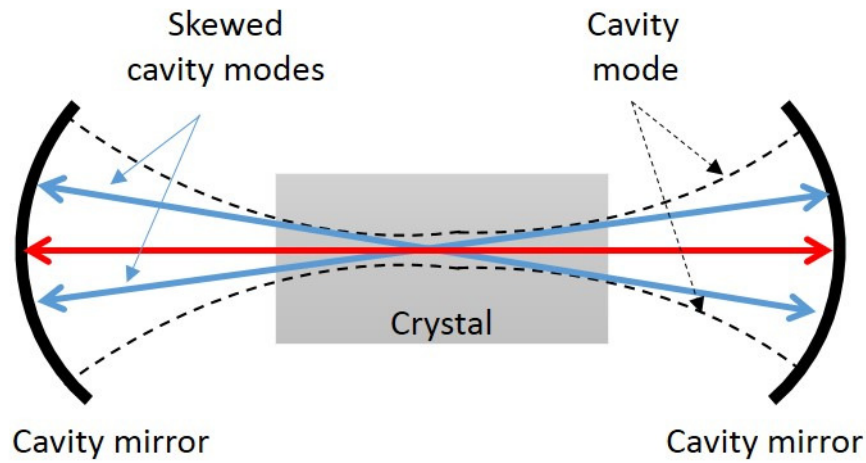


Fig. 4.16 Cavity modes in a confocal geometry with the perfect mode represented in red arrow and skewed modes represented by blue arrows which can also be supported inside the cavity mode represented by dashed lines.

The higher order Stokes fields generated in this case must be generated at a slight angle since as seen in the dispersion curve of figure 4.3 (b), the SPS-gain and wavelength shift go to zero for 0° scattering. In our cavity, as the curved mirror separation approaches the confocal stability limit, the cavity mode becomes large on all mirrors and small inside the crystal. Near this limit cavity can support skewed cavity modes with fairly low loss. The small angled generation of closely-spaced higher-order Stokes fields are supported in such skewed cavity modes. This is shown in figure 4.16 where the dotted boundary represents the cavity mode generated by the mirrors, the red arrows represents perfect modes or modes with minimum loss and the blue lines represent the skewed cavity modes. Figure 4.16 is drawn as a two

mirror cavity for simplicity, but the same argument applies to our four-mirror ring cavity.

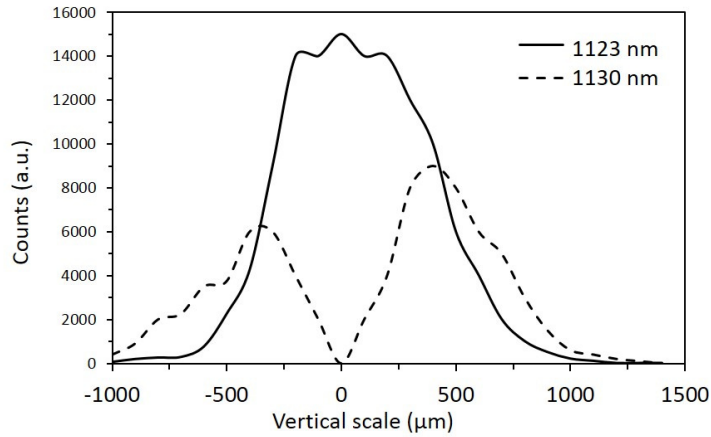


Fig. 4.17 Vertical scanning of the first and second Stokes generated with their respective counts observed in a spectrometer on scanning in the vertical plane.

The angled Stokes fields can be generated symmetrically on both sides of the pump laser propagation direction resulting in a fanned-out higher-order Stokes generation at the output coupler. To observe this, we investigated the spatial shape of the cavity fields leaking through one of the cavity mirrors, by scanning a fibre coupled to a spectrometer across the output beam and plotted the relative intensity of first and second Stokes as a function of position. Figure 4.17 shows the scan measurement. The solid line represents first Stokes and the dashed line represents the closely-spaced higher-order Stokes (second Stokes) measured using an Ocean-optics NIR-512 spectrometer (detecting range 850 to 1700 nm with resolution of 3 nm).

It was found that our bow-tie shaped confocal ring cavity supported the noncollinear generation of higher-order Stokes fields fanned-out about the pump laser axis in the vertical plane. At the same time, a horizontal scan showed higher-order Stokes generation centred on the same position as the pump. This is expected due to the orientation of the crystal. The crystal was oriented with the optic axis parallel to the optical table with the pump laser polarisation also parallel to it as shown in figure 4.18. In such a configuration, the triangular generation of signal and idler is preferred in the vertical plane with highest gain as the polarisation of the signal and Stokes is maintained parallel to each other and the optic axis while in any other

angular generation, the polarisation of the generated signal and idler beams become non-parallel. We thus expect the terahertz radiation to be emitted in a vertical plane above and below the crystal.

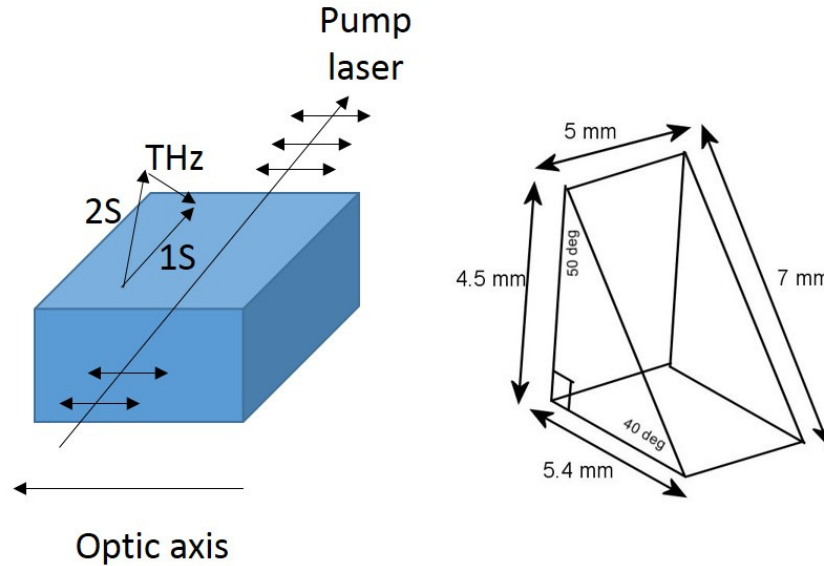


Fig. 4.18 Left: Orientation crystal with respect to the pump polarisation determining the plane of generation of single and idler frequencies. Right: Dimensions of the silicon prisms used in the experiment.

4.9 Measuring the generated terahertz waves

To study and enhance the terahertz generation, the output coupler was changed to a highly reflecting one over the complete generated Stokes fields compared to the 1 % output coupler used in the lithium niobate Raman laser mentioned in chapter 3. As in the previous experimental setup, the cavity had the 2 mm MgF_2 birefringent filter which allowed only 497 cm^{-1} shifting of the pump frequency into the cavity and prevented further cascading on the 248 cm^{-1} shift. This makes available the complete pump power for pure forward operation maximising the enhancement of the Stokes field at 1123 nm . The generated terahertz radiation was coupled-out using the conventional method using silicon prisms as shown in figure 4.19. These prisms were attached to the crystal using few drops of methanol for contact. Presence of only orange arrows denote the absence of backward Stokes fields.

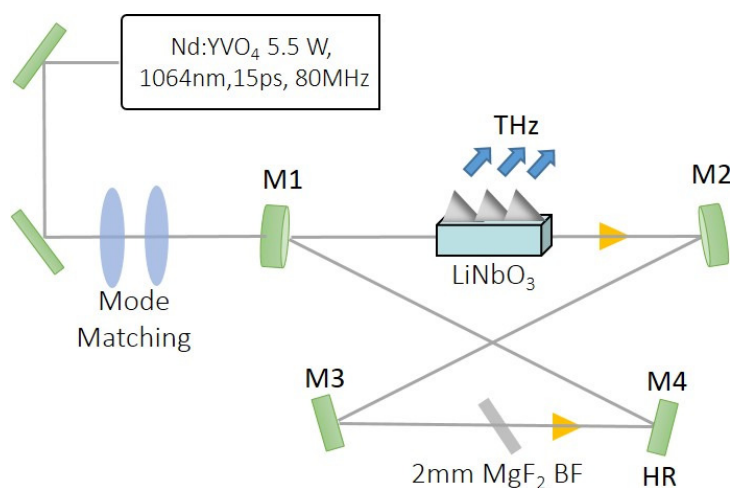


Fig. 4.19 Experimental setup for terahertz generation from lithium niobate Raman laser with silicon prisms for output coupling of terahertz and with high Q for the range of Stokes fields generated.

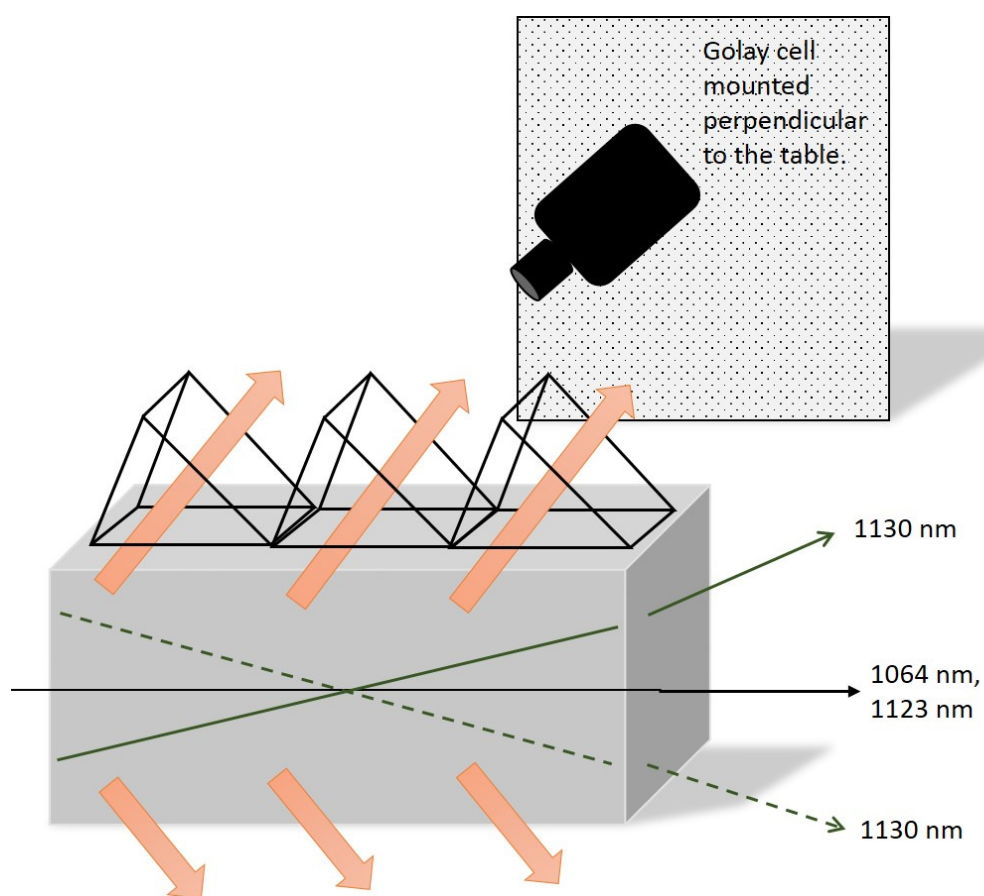


Fig. 4.20 Angled second Stokes generation with terahertz generation output coupled by silicon prisms and measured by a Golay cell which is mounted on a stand mounted perpendicular to the optical table.

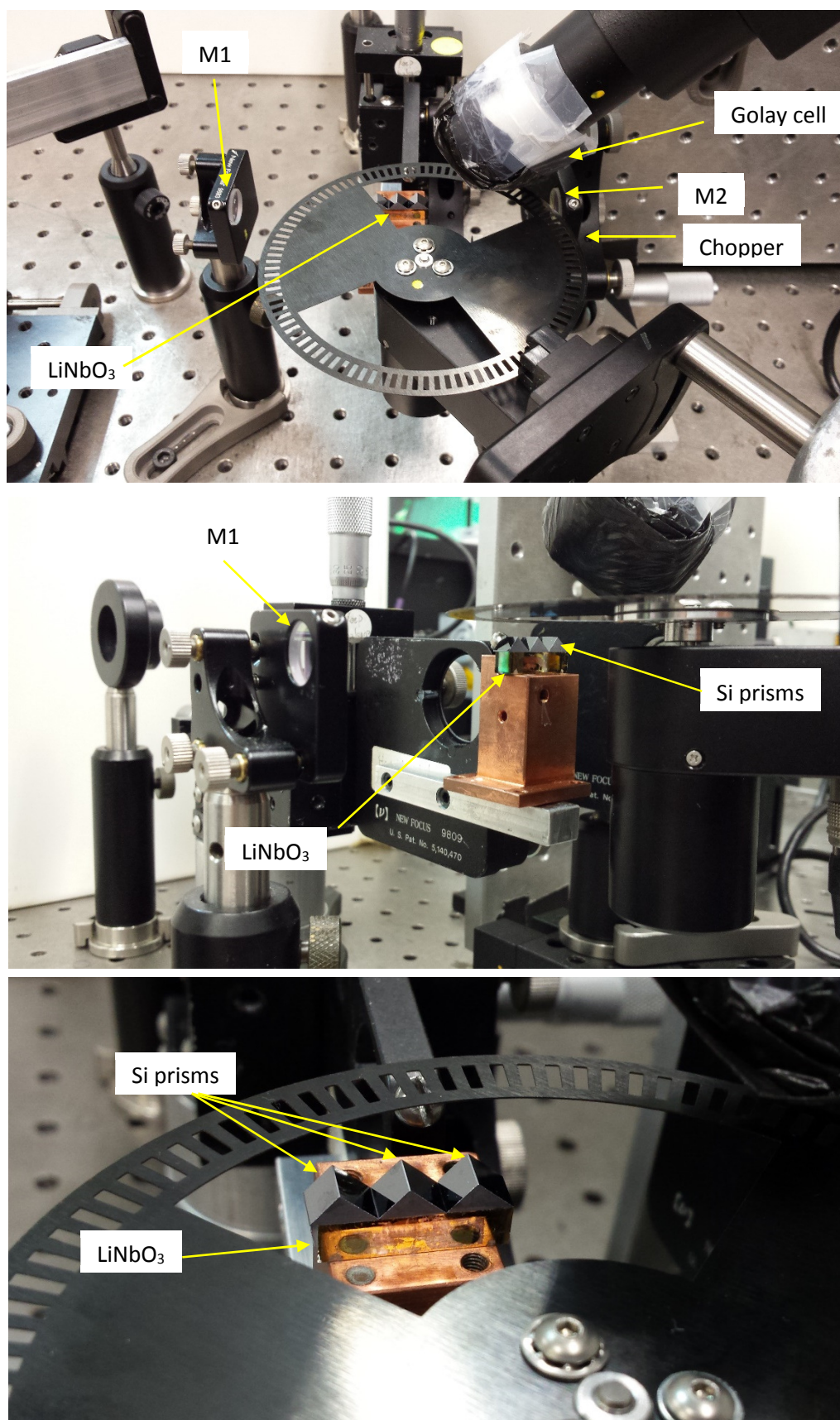


Fig. 4.21 Some pictures of the lithium niobate Raman laser generating terahertz.

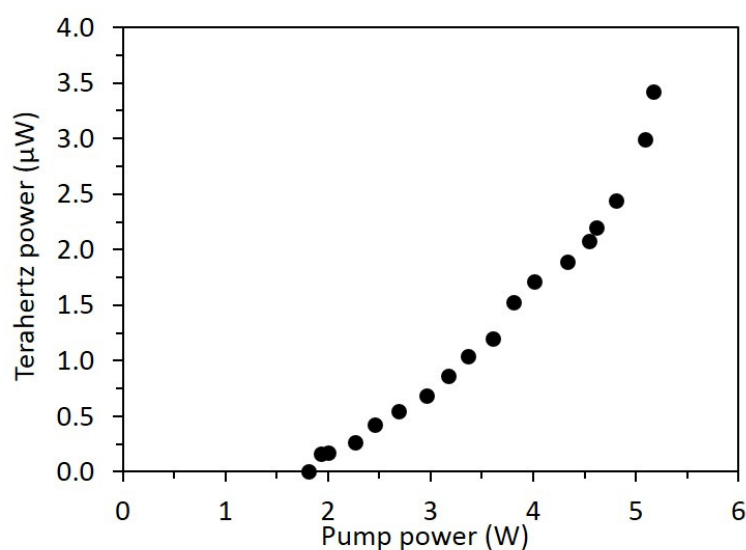


Fig. 4.22 Power transfer measurement of the terahertz waves generated.

Since the second Stokes was generated offset only in the vertical plane, the terahertz generation was also in the vertical plane. Hence the silicon prisms whose dimensions are given in figure 4.18, were mounted on the top of the lithium niobate crystal to output-couple the terahertz radiation as depicted in figure 4.20. Figure 4.21 gives some of the pictures of the experimental setup. The terahertz that is generated in the downward direction unfortunately cannot be collected as it is blocked by the base of the crystal holder. Nevertheless, adjusting the crystal height to make the pump laser traverse near to the upper surface minimised the absorption loss of collected terahertz by the lithium niobate crystal. The generated terahertz radiation was detected using a Golay cell. The power transfer measurements were taken with output spectra at each pump power. Figure 4.23 gives the spectra and figure 4.22 gives the power transfer measurement.

The power transfer measurement show a fairly linear generation with pump power. A maximum of $3.42 \mu\text{W}$ of terahertz radiation was obtained at maximum pump power with a threshold of 1.81 W . From the spectra obtained at different pump powers, it can be seen that the first Stokes gets shifted to closely-spaced higher-order Stokes with a range of shifts depending upon the pump power. The laser system was

controlled by the 1 mm thick MgF_2 birefringent filter alone which has a very broad (~ 100 nm) free spectral range.

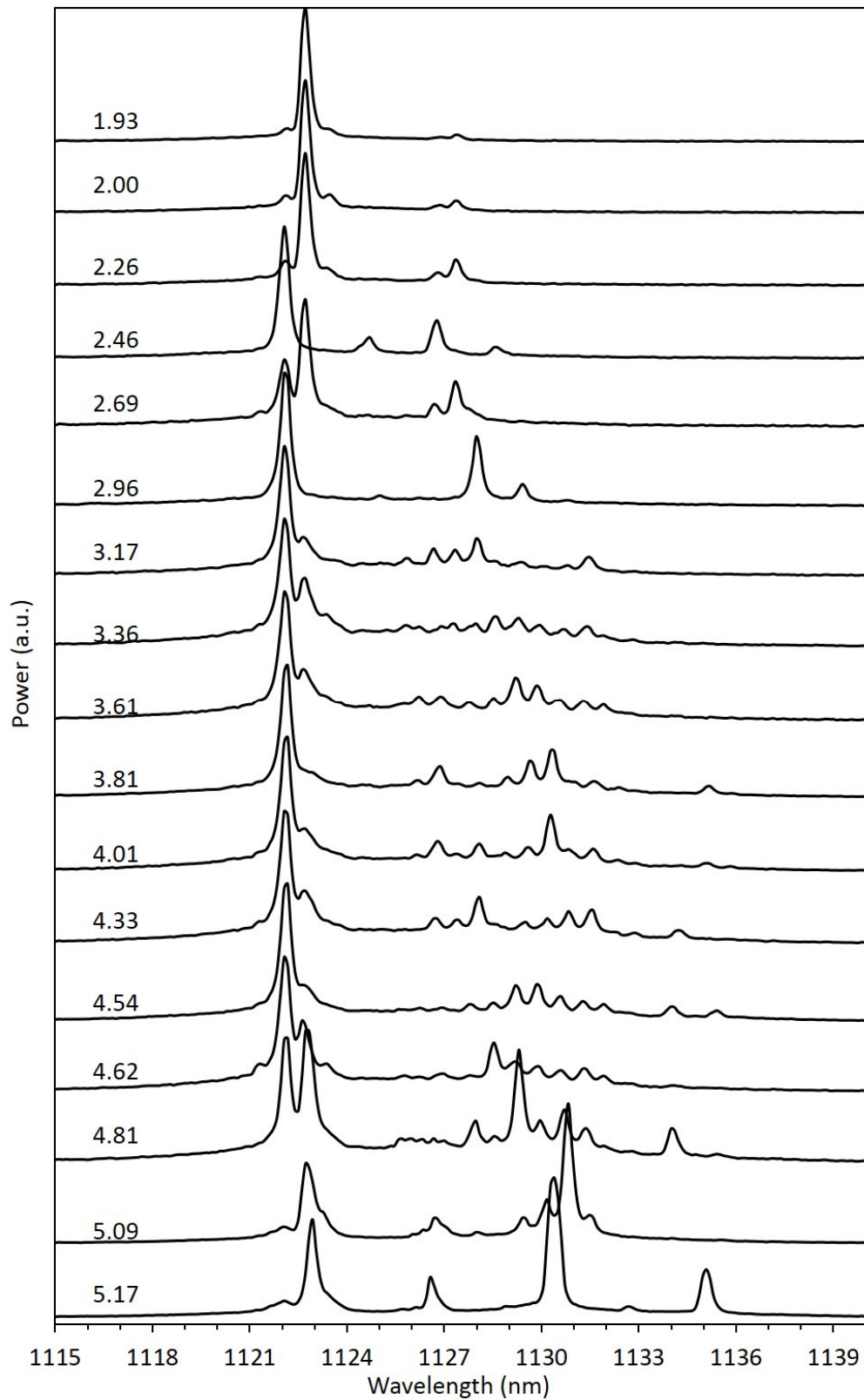


Fig. 4.23 Pure clockwise spectrum at different pump powers in Watts.

This results in the cavity enhanced first Stokes fields undergoing a number of shifts, perhaps even cascaded, each contributing to the terahertz generation. It is difficult to predict the particular shifts that would lase because of the competition between shifts with different gains and different skewed-mode cavities. These can be imagined by referring to figure 4.16 where one can see the possibility of many skewed cavity modes.

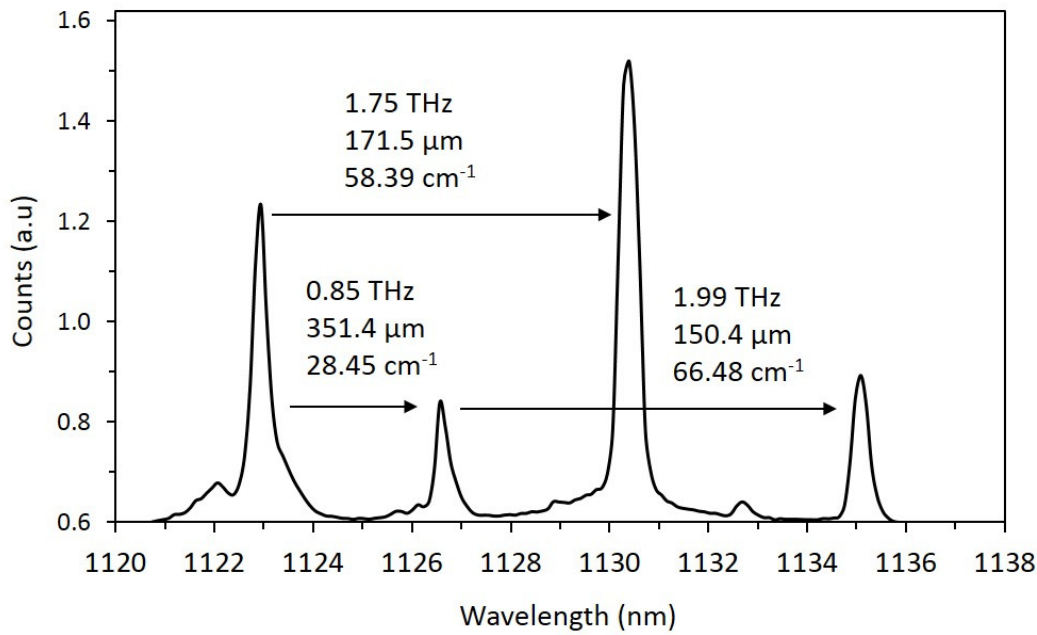


Fig. 4.24 Pure clockwise Stokes spectra at maximum pump power showing the terahertz frequencies with their respective wavelengths and polariton shifts.

At lower pump powers, the spectrum seems to have a ripple-like structure showing that the cavity enhanced first-Stokes field gets cascaded multiple times by low-energy polariton shifts. Since the ripples seem to be not equally spaced, this suggests the participation of multiple low-energy polariton shifts. Thus the terahertz measured by the Golay cell is a summation of many different terahertz wavelengths caused by multiple low-energy polariton shifts. At maximum pump power, we seem to have only three terahertz frequencies being generated: 0.85 THz, 1.99 THz, 1.75 THz frequencies corresponding to 351.44 μm , 150.45 μm and 171.55 μm wavelengths with low-frequency polariton shifts of 28.45 cm^{-1} , 66.48 cm^{-1} and 58.39 cm^{-1} respectively causing this cascading of the cavity enhanced Stokes field.

The spectrum at maximum pump power is shown in figure 4.24 with the generated terahertz frequencies wavelengths. While different orders of generation of these lines is possible, we think that this is the most likely due to the fact that the small peaks appear together. Also it can be seen in figure 4.22 that the power transfer curve peaks at maximum pump power due to the combination of multiple terahertz wave generations. We note that lots of narrow cascaded Stokes line and so narrow terahertz lines is consistent with the laser pulse duration. The terahertz waves are expected to have pulse duration similar to that of the pump pulse duration of ≈ 15 ps. The minimum terahertz bandwidth can be calculated from: $\Delta\tau * \Delta f \sim 0.5$, giving $\Delta f \approx 0.033$ THz.

4.10 Laser control: Single terahertz frequency generation

We would like to be able to control and tune the terahertz output from the laser. This requires us to introduce some control in our system to select specific terahertz frequencies. This selectability can be achieved by introducing an etalon into the cavity to control the Stokes frequencies. Etalons are widely used for laser wavelength tuning, line-width control and as an instrument to measure the line-width. An etalon or a Fabry-Perot interferometer is a pair of reflecting surfaces spaced by micrometres to centimetres, in which a beam of light undergoes multiple reflections resulting in an optical transmission spectrum periodic in frequency. The transmission of an etalon can be derived as [53]:

$$T = \left\{ \frac{(1-R)^2}{1+R^2-2R\cos\delta} \right\} \text{ or } \left\{ \frac{1}{1+\frac{4R}{(1-R)^2}\sin^2\left(\frac{\delta}{2}\right)} \right\} \quad (4.1)$$

where R is the reflectivity of the surfaces and δ is the phase difference between successive reflected beams given by:

$$\delta = \frac{2\pi}{\lambda} 2nd \cos \theta \quad (4.2)$$

with θ being the angle of incidence, n the refractive index between the surfaces and d the thickness of etalon. The wavelengths of maximum transmission are obtained when,

$$\delta = \frac{4\pi nd \cos \theta}{\lambda_m} = 2m\pi \text{ or } \lambda_m = \frac{2nd \cos \theta}{m} \quad (4.3)$$

Hence the frequency of maximum transmission becomes,

$$\nu_m = m \frac{c}{2nd \cos \theta} \quad (4.4)$$

The distance between the frequencies of maximum transmission is defined as the free spectral range (FSR) of the etalon and is given by:

$$FSR = \nu_{m+1} - \nu_m = \frac{c}{2nd \cos \theta} \quad (4.5)$$

Thus the location of transmission peaks is an integral multiple of the FSR, from equations (4.4) and (4.5). The location of the peaks is determined by the optical path length ($nd \cos \theta$) as seen in above equations while the shape of the peaks is determined by the reflectivity (R).

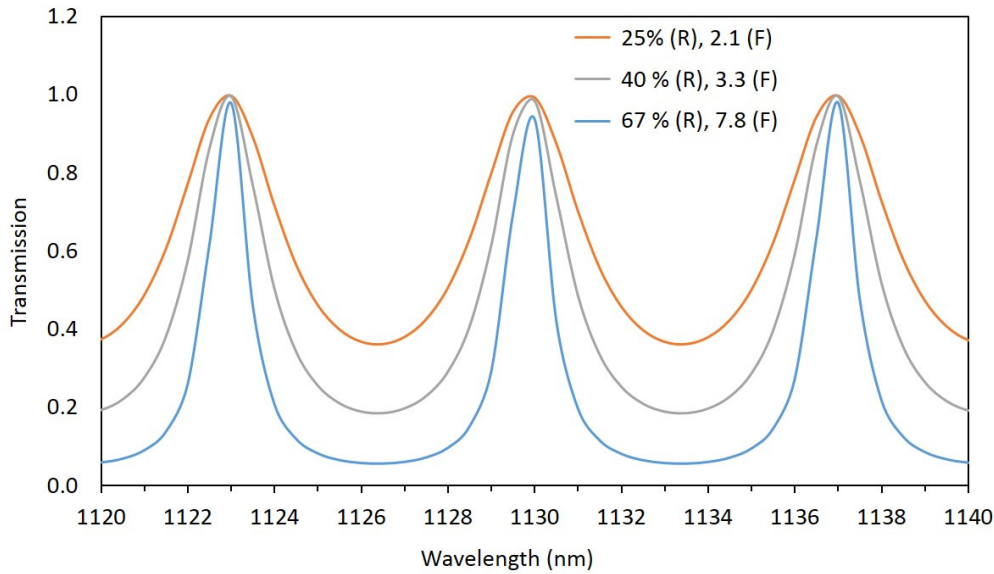


Fig. 4.25 Variance of transmittance of an etalon with different reflectivities for the surfaces.

The higher the reflectivity, the narrower are the peaks as can be seen from figure 4.24 which shows the transmission of a 49.5 μm fused silica etalon with different reflectivities of the surfaces at an angle of 20° . A quantity called finesse, also shown

in the legend of figure 4.25, is used to quantify the shape of the transfer function of the etalon, given by:

$$F = \frac{\pi\sqrt{R}}{(1-R)} \quad (4.6)$$

We propose the use of an etalon to obtain a single frequency tunable terahertz output. Thus by controlling the thickness, reflectivity and angle of incidence, we can induce the required spectral filtering to control the Stokes and so the terahertz output. The etalon must have transmission for 1123 nm and the desired terahertz frequency can be selected by the FSR of the etalon. In other words, the FSR of the etalon becomes equal to the generated terahertz frequency. This generated terahertz frequency then can be tuned by adjusting the angle of the etalon as seen in figure 4.25.

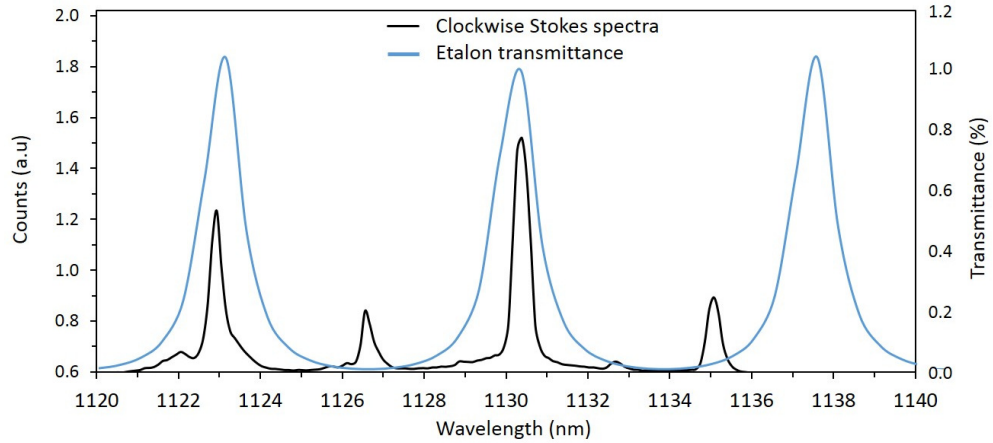


Fig. 4.26 Transmittance curve (blue) of etalon superimposed over the Stokes spectra (black) at maximum pump power in the same wavelength range.

Figure 4.26 shows the superposition of the transmission spectra of a 49.5 μm thick fused silica etalon with 67 % reflective surfaces with an angle of incidence of 20° over the Stokes spectra at maximum pump power. It clearly shows the possibility of suppression of other terahertz frequencies and allowing only the cascading of 1123 nm to 1130.4 nm which would generate a single terahertz frequency of 1.75 THz. The etalon can be rotated to alter the FSR and thereby allow other

terahertz frequencies selectably. The author and colleagues intend to carry out this experiment in near future to make possible selectable, tunable terahertz frequency generation from picosecond Raman lasers via parametric scattering.

4.11 Chapter Summary

In the present chapter we present a terahertz wave generator by parametric scattering of polaritons in an ultrafast lithium niobate Raman laser, pumped by a mode-locked nanojoule energy-scale picosecond laser. Stimulated scattering of polaritons generates a frequency shift which depends upon the angle of interaction between the pump and the Stokes fields. We coupled the pump power into a Stokes field using a forward polariton shift to convert 1064 nm pump to 1123 nm. This cavity enhanced Stokes field cascaded to closely-spaced higher-order Stokes fields by low frequency polariton scattering of the 248 cm^{-1} vibrational mode of the lithium niobate crystal, generating terahertz frequencies. At maximum pump power we could generate three terahertz frequencies viz. 0.85 THz, 1.99 THz and 1.75 THz corresponding to wavelengths of 351.44 μm , 150.45 μm and 171.55 μm respectively. The higher-order closely-spaced Stokes fields were generated at slight angles to the pump and 1123 nm cavity field. The near-confocal cavity supported the lasing of these Stokes fields slightly skewed in alignment.

The fact that we generate cavity enhanced Stokes fields, rather than using a resonant cavity to enhance the pump itself, avoids the need for nm-scale control of the cavity length to maintain the cavity locking. We propose that the multiple terahertz frequencies generated could be controlled by introducing an etalon into the cavity which could tune the generated terahertz radiation. In conclusion, this method of generating terahertz frequencies, presents us with an alternate and simpler approach for terahertz generation from mode-locked picosecond lasers.

4.12 References for Chapter 4

- [1] B. Ferguson, X.-C. Zhang, Materials for terahertz science and technology, *Nature materials*, 1 (2002) 26-33.
- [2] J. Fleming, High-resolution submillimeter-wave Fourier-transform spectrometry of gases, *IEEE Transactions on Microwave Theory Techniques*, 22 (1974) 1023-1025.
- [3] E. Bründermann, H.-W. Hübers, M.F. Kimmitt, *Terahertz Techniques*, Springer, 2012.
- [4] M. Tonouchi, Cutting-edge terahertz technology, *Nature Photonics*, 1 (2007) 97-105.
- [5] M. Mukherjee, N. Mazumder, S.K. Roy, K. Goswami, GaN IMPATT diode: a photo-sensitive high power terahertz source, *Semiconductor Science and Technology*, 22 (2007) 1258.
- [6] W. Deal, X. Mei, K.M. Leong, V. Radisic, S. Sarkozy, R. Lai, THz monolithic integrated circuits using InP high electron mobility transistors, *IEEE Transactions on Terahertz Science and Technology* 1, (2011) 25-32.
- [7] S. Fatholouloumi, E. Dupont, C. Chan, Z. Wasilewski, S. Laframboise, D. Ban, A. Mátyás, C. Jirauschek, Q. Hu, H. Liu, Terahertz quantum cascade lasers operating up to ~ 200 K with optimized oscillator strength and improved injection tunneling, *Optics Express*, 20 (2012) 3866-3876.
- [8] A. Nahata, A.S. Weling, T.F. Heinz, A wideband coherent terahertz spectroscopy system using optical rectification and electro-optic sampling, *Applied Physics Letters*, 69 (1996) 2321-2323.
- [9] M.A. Belkin, F. Capasso, F. Xie, A. Belyanin, M. Fischer, A. Wittmann, J. Faist, Room temperature terahertz quantum cascade laser source based on intracavity difference-frequency generation, *Applied Physics Letters*, 92 (2008) 201101.
- [10] Y. Takida, T. Ohira, Y. Tadokoro, H. Kumagai, S. Nashima, Tunable picosecond terahertz-wave parametric oscillators based on noncollinear pump-enhanced signal-resonant cavity, *Selected Topics in Quantum Electronics, IEEE Journal of*, 19 (2013) 8500307-8500307.

- [11] Y. Takida, S. Maeda, T. Ohira, H. Kumagai, S. Nashima, Noncascading THz-wave parametric oscillator synchronously pumped by mode-locked picosecond Ti:sapphire laser in doubly-resonant external cavity, *Optics Communications*, 284 (2011) 4663-4666.
- [12] G.K. Kitaeva, Terahertz generation by means of optical lasers, *Laser Physics Letters*, 5 (2008) 559.
- [13] K. Kawase, J.-i. Shikata, H. Ito, Terahertz wave parametric source, *Journal of Physics D: Applied Physics*, 35 (2002) R1.
- [14] M. Tonouchi, *Terahertz Technology*, Tokyo, Japan: Ohmsha, (2006).
- [15] P.H. Siegel, Terahertz technology in biology and medicine, *Microwave Symposium Digest, 2004 IEEE MTT-S International*, IEEE, 2004, pp. 1575-1578.
- [16] F. Zernike, P.R. Berman, Generation of far-infrared as a difference frequency, *Physical Review Letters*, 15 (1965) 999-1001.
- [17] J.R. Morris, Y.R. Shen, Theory of far-infrared generation by optical mixing, *Physical Review A*, 15 (1977) 1143-1156.
- [18] J.M. Yarborough, S.S. Sussman, H.E. Puthoff, R.H. Pantell, B.C. Johnson, Efficient, tunable optical emission from LiNbO_3 without a resonator, *Applied Physics Letters*, 15 (1969) 102-105.
- [19] B.C. Johnson, H.E. Puthoff, J. SooHoo, S.S. Sussman, Power and linewidth of tunable stimulated far-infrared emission in LiNbO_3 , *Applied Physics Letters*, 18 (1971) 181-183.
- [20] J.-i. Shikata, K. Kawase, K. Karino, T. Taniuchi, H. Ito, Tunable terahertz-wave parametric oscillators using LiNbO_3 and $\text{MgO}:\text{LiNbO}_3$ crystals, *Microwave Theory and Techniques*, *IEEE Transactions on*, 48 (2000) 653-661.
- [21] I. Shoji, T. Kondo, A. Kitamoto, M. Shirane, R. Ito, Absolute scale of second-order nonlinear-optical coefficients, *Journal Of Optical Society of America B*, 14 (1997) 2268-2294.
- [22] J.-i. Shikata, K. Kawase, K.-i. Karino, T. Taniuchi, H. Ito, Tunable terahertz-wave parametric oscillators using LiNbO_3 and $\text{MgO}:\text{LiNbO}_3$ crystals, *Microwave Theory and Techniques*, *IEEE Transactions on*, 48 (2000) 653-661.
- [23] Y.-R. Shen, *Principles of nonlinear optics*, (1984).

- [24] S.S. Sussman, Tunable light scattering from transverse optical modes in lithium niobate, in, DTIC Document, 1970.
- [25] J.-i. Shikata, M. Sato, T. Taniuchi, H. Ito, K. Kawase, Enhancement of terahertz-wave output from LiNbO₃ optical parametric oscillators by cryogenic cooling, *Optics Letters*, 24 (1999) 202-204.
- [26] J. Shikata, K. Kawase, M. Sato, T. Taniuchi, H. Ito, Characteristics of coherent terahertz wave generation from LiNbO₃ optical parametric oscillator, *Electronics and Communications in Japan (Part II: Electronics)*, 82 (1999) 46-53.
- [27] M. Piestrup, R. Fleming, R. Pantell, Continuously tunable submillimeter wave source, *Applied Physics Letters*, 26 (1975) 418-421.
- [28] K. Kawase, M. Sato, T. Taniuchi, H. Ito, Coherent tunable THz-wave generation from LiNbO₃ with monolithic grating coupler, *Applied Physics Letters*, 68 (1996) 2483-2485.
- [29] K. Kawase, M. Sato, K. Nakamura, T. Taniuchi, H. Ito, Unidirectional radiation of widely tunable THz wave using a prism coupler under noncollinear phase matching condition, *Applied Physics Letters*, 71 (1997) 753-755.
- [30] T. Edwards, D. Walsh, M. Spurr, C. Rae, M. Dunn, P. Browne, Compact source of continuously and widely-tunable terahertz radiation, *Optics Express*, 14 (2006) 1582-1589.
- [31] A.J. Lee, H.M. Pask, Continuous wave, frequency-tunable terahertz laser radiation generated via stimulated polariton scattering, *Optics Letters*, 39 (2014) 442-445.
- [32] A. Lee, Y. He, H. Pask, Frequency-Tunable THz Source Based on Stimulated Polariton Scattering in, *Quantum Electronics, IEEE Journal of*, 49 (2013) 357-364.
- [33] S.i. Hayashi, K. Maki, C. Otani, K. Kawase, Terahertz wave parametric sources, *Topical Problems of Nonlinear Wave Physics, Proceedings of SPIE* 5975, (2006).
- [34] T. Yajima, N. Takeuchi, Far-infrared difference-frequency generation by picosecond laser pulses, *Japanese Journal of Applied Physics*, 9 (1970) 1361.
- [35] K. Yang, P. Richards, Y. Shen, Generation of Far-Infrared Radiation by Picosecond Light Pulses in LiNbO₃, *Applied Physics Letters*, 19 (1971) 320-323.

- [36] L. Xu, X.C. Zhang, D. Auston, Terahertz beam generation by femtosecond optical pulses in electro-optic materials, *Applied Physics Letters*, 61 (1992) 1784-1786.
- [37] P.H. Siegel, Terahertz technology, *IEEE Transactions on microwave theory and techniques*, 50 (2002) 910-928.
- [38] K. Yeh, M. Hoffmann, J. Hebling, K.A. Nelson, Generation of 10 J ultrashort terahertz pulses by optical rectification, *Applied Physics Letters*, 90 (2007) 1-3.
- [39] W.R. Huang, S.-W. Huang, E. Granados, K. Ravi, K.-H. Hong, L.E. Zapata, F.X. Kärtner, Highly efficient terahertz pulse generation by optical rectification in stoichiometric and cryo-cooled congruent lithium niobate, *Journal of Modern Optics*, (2014) 1-8.
- [40] J.A. Fülöp, L. Pálfalvi, M.C. Hoffmann, J. Hebling, Towards generation of mJ-level ultrashort THz pulses by optical rectification, *Optics Express*, 19 (2011) 15090-15097.
- [41] K.L. Vodopyanov, Optical generation of narrow-band terahertz packets in periodically inverted electro-optic crystals: conversion efficiency and optimal laser pulse format, *Optics Express*, 14 (2006) 2263-2276.
- [42] F. Blanchard, L. Razzari, H. Bandulet, G. Sharma, R. Morandotti, J. Kieffer, T. Ozaki, M. Reid, H. Tiedje, H. Haugen, Generation of 1.5 μJ single-cycle terahertz pulses by optical rectification from a large aperture ZnTe crystal, *Optics Express*, 15 (2007) 13212-13220.
- [43] C.P. Hauri, C. Ruchert, C. Vicario, F. Ardana, Strong-field single-cycle THz pulses generated in an organic crystal, *Applied Physics Letters*, 99 (2011) 161116.
- [44] C. Ruchert, C. Vicario, C.P. Hauri, Scaling submillimeter single-cycle transients toward megavolts per centimeter field strength via optical rectification in the organic crystal OH1, *Optics Letters*, 37 (2012) 899-901.
- [45] C. Ruchert, C. Vicario, C.P. Hauri, Spatiotemporal focusing dynamics of intense supercontinuum THz pulses, *Physical Review Letters*, 110 (2013) 123902.
- [46] J. Hebling, K.-L. Yeh, M.C. Hoffmann, B. Bartal, K.A. Nelson, Generation of high-power terahertz pulses by tilted-pulse-front excitation and their application possibilities, *Journal of Optical Society of America B*, 25 (2008) B6-B19.

- [47] K. Miyamoto, A. Lee, T. Saito, T. Akiba, K. Suizu, T. Omatsu, Broadband terahertz light source pumped by a 1 μm picosecond laser, *Applied Physics B*, 110 (2013) 321-326.
- [48] Y.-S. Lee, T. Meade, V. Perlin, H. Winful, T. Norris, A. Galvanauskas, Generation of narrow-band terahertz radiation via optical rectification of femtosecond pulses in periodically poled lithium niobate, *Applied Physics Letters*, 76 (2000) 2505-2507.
- [49] C. Weiss, G. Torosyan, Y. Avetisyan, R. Beigang, Generation of tunable narrow-band surface-emitted terahertz radiation in periodically poled lithium niobate, *Optics Letters*, 26 (2001) 563-565.
- [50] Y. Sasaki, Y. Avetisyan, H. Yokoyama, H. Ito, Surface-emitted terahertz-wave difference-frequency generation in two-dimensional periodically poled lithium niobate, *Optics Letters*, 30 (2005) 2927-2929.
- [51] T.W. Hansch, B. Couillaud, Laser frequency stabilization by polarization spectroscopy of a reflecting reference cavity, *Optics Communications*, 35 (1980) 441-444.
- [52] G. Zhao, M.t. Mors, T. Wenckebach, P. Planken, Terahertz dielectric properties of polystyrene foam, *Journal of Optical Society of America B*, 19 (2002) 1476-1479.
- [53] F.L. Pedrotti, L.S. Pedrotti, Introduction to optics 2nd edition, Introduction to Optics 2nd Edition by Frank L. Pedrotti, SJ, Leno S. Pedrotti New Jersey: Prentice Hall, 1993, 1 (1993).

5

Conclusion and future work

Light has fascinated man from immemorial times. The unending quest of the human mind to know the world around him keeps fuelling this arena of research. This year, 2015 is being celebrated as the international year of light to spread the awareness of the achievements of light science and its applications. I feel happy and contented to submit a thesis on developing ultrafast Raman laser sources in this very year.

The field of solid-state Raman lasers had its inception in 1963 when Eckhardt observed SRS for the first time in crystalline media including diamond [1]. But the real milestone which later paved the way for the development of solid-state Raman lasers was the demonstration of frequency conversion of a neodymium laser by Amman *et. al.* [2]. The science and engineering of solid-state Raman lasers, finding immense applications in very diverse fields, have undergone substantial

developments in the last four decades. Due to the versatility of the Raman process, SRS has been successfully utilized in developing a wide variety of lasers in the CW, quasi-CW and pulsed regimes.

The MQ Photonics Centre, Macquarie University, where the present research was carried out, have a significant history of research into wavelength conversion of ultrafast laser sources using SRS. Ultrafast Raman lasers that could efficiently shift infrared picosecond neodymium lasers into the hard-to-reach yellow spectrum intended for applications in label-free two-photon microscopy have been developed [3]. The extensive research also involved developing a scheme to generate up to three wavelengths from a single source [4]. The centre has been successful in demonstrating picosecond Raman lasers ranging in wavelength from deep ultraviolet to the mid-infrared.

In this context, the research work presented in this thesis forms a small contribution to the ever expanding exciting field of ultrafast Raman laser phenomena. While solid-state Raman lasers based on Q-switched mode-locked lasers have been demonstrated previously [5, 6], development of Raman lasers based on CW-mode-locked lasers started only around seven years back [3, 7]. This motivated us to contribute more into the design and development of efficient CW mode-locked Raman lasers.

The first work that we report in this thesis is the demonstration of a simple and highly efficient picosecond diamond Raman laser operating at both 1240 nm and 1485 nm in diamond pumped by a CW mode-locked laser. Up to 2.75 W output power and 59% conversion efficiency (η_o) were achieved for the first-Stokes 1240 nm in a low-Q Raman cavity. The slope efficiency (η_s) tended towards 76% when the pump was far above the SRS threshold. The system has great potential in power scaling for the Stokes generation owing to the high slope efficiency and the superior thermal properties of diamond. The first-Stokes generation in this work was much more efficient than the synchronously pumped Raman lasers reported previously, e.g. $\eta_o = 25.6\%$, $\eta_s = 42\%$ in [3], $\eta_o = 29\%$, $\eta_s = 41\%$ in [8] and $\eta_o = 10.3\%$, $\eta_s = 25\%$ in [9]. The improvement can mainly be attributed to the ring-cavity configuration for the

present work, as well as superior coatings for both the cavity mirrors and Raman crystal used. Our laser forms the first synchronously pumped solid-state ring Raman laser.

We also could demonstrate efficient generation of second Stokes (1485 nm) even though the cavity mirrors did not resonate the second Stokes fields. The efficient generation was achieved by four wave mixing seeding the single-pass generation of second Stokes, making the cavity design easier with mirror coating not requiring to have reflectivities at the second Stokes wavelength and not requiring any intracavity dispersion management. 1.0 W of 1485 nm was generated with 21 % overall conversion efficiency. Pulse compression was achieved in the Raman laser with the minimum pulse duration of 9 ps for 1240 nm and 6 ps for 1485 nm obtained, compared to 15 ps for the pump laser. Thus we could demonstrate an alternate method of higher order Stokes wavelength generation with the FWM seeding the single-pass generation, in comparison to the standard route of resonated cascaded generation. This resulted in the filing of an Australian patent application titled "*A method and a system for generating a Raman second stokes light to a source light.*" Our laser thus forms a highly efficient method for extending the wavelength accessibility of picosecond lasers. Comparing our work to a recent picosecond pumped Raman generator experiment, we see that our laser achieves efficient operation for 50 nJ pulses, whereas the Raman generator approach required 15 μ J. This highlights the power of our method for converting picosecond oscillators. Extension of this work to other lasers such as picosecond VECSELs laser offers to greatly expand their wavelength reach and may provide interesting sources for many applications.

Backward Stokes generation had been a topic of interest in Raman lasers owing to the possibility of greater pulse shortening when the backward Stokes sweeps through the pump pulse, extracting the power in a short pulse. Our picosecond diamond Raman laser could also generate backward Stokes which was favoured over forward Stokes for positive cavity lengths. We achieve pure backwards operation for all cavity lengths using an isolator. Unfortunately we did not observe pulse compression,

which we attribute to weak depletion of the pump. Power scaling leading to better pump depletion has better pulse compression prospects.

Synchronously pumped laser systems have been modelled theoretically with good consistency with observations by Granados *et. al.* in [10] explaining the pulse compression mechanism happening in the system. The modelling based on the coupled equations presented by Penzkofer in [11] could be modified to model the second Stokes and well and backward Stokes generation to theoretically study the mechanism happening in these cases. This forms part of future endeavours in this work.

Generating multiple wavelengths from a single source can provide flexible coverage of longer wavelength ranges. We presented a multiwavelength ultrafast Raman laser which could generate four wavelengths (1123 nm, 1140 nm, 1155 nm and 1173 nm), based on an MgO doped lithium niobate crystal employing SRS and SPS to switchably or simultaneously convert the pump light. The laser gave different wavelengths for pure forward and pure backward operation unlike the diamond Raman laser that we demonstrated before. This was due to the fact that the forward operation was due to a polariton shift while the backward was caused by a Raman shift. Polar crystals have distinct scattering mechanisms: pure electromagnetic in nature at small angles and pure mechanical at large angles. The collinear geometry of our laser utilized these two aspects.

Tunable frequency generation has been well studied in lithium niobate crystals, starting with Loudon and Puthoff in 1963 while they were investigating crystals which are both infrared active and Raman active. Since then there had been many polariton lasers based on lithium niobate crystals. For the first time we employed both Raman scattering as well as polariton scattering in one laser to generate four different wavelengths, making it a kind of hybrid laser (Raman and polariton). Thus this laser could generate multiple wavelengths which could also be tuned due to the parametric nature of SPS at very low frequencies. The pump was coupled into cavity-enhanced first Stokes fields. These cavity Stokes fields when sufficiently enhanced in intensity, were cascaded by backward Raman shifts generating second

order Stokes wavelengths. The laser generated two first Stokes wavelengths (1123 nm and 1140 nm) which cascaded to generate the second Stokes wavelengths (1173 nm and 1155 nm) respectively.

The laser was refined by introducing control of generated wavelengths making the pump power available exclusively for each wavelength. A birefringent filter was used to make the laser generate the different wavelengths controllably and selectably. This results in a spectrally controlled laser which could generate single wavelengths as well as pairs of them by controlled tuning of the birefringent filter. Thus we could demonstrate a synchronously pumped lithium niobate Raman laser which could generate four different wavelengths switchably and controllably.

Terahertz frequency generation and applications has been a hot topic undergoing exponential progress in recent years. We demonstrated a terahertz wave generator by parametric scattering of polaritons in an ultrafast lithium niobate Raman laser, pumped by mode-locked nanojoule energy-scale picosecond laser. Stimulated scattering of polaritons generates a frequency shift which depends upon the angle of interaction between the pump and the Stokes fields. The Raman shifted Stokes field was coupled into closely-spaced higher-order Stokes fields by low frequency polariton scattering off the 248 cm^{-1} vibrational mode of lithium niobate crystal, generating terahertz frequencies. The large FSR range of the birefringent filter allowed multiple uncontrolled cascading to happen resulting in the generation of multiple terahertz lines. At maximum pump power we could generate three terahertz frequencies viz. 0.85 THz, 1.99 THz and 1.75 THz corresponding to wavelengths of $351\text{ }\mu\text{m}$, $150\text{ }\mu\text{m}$ and $171\text{ }\mu\text{m}$ respectively. The higher-order closely-spaced Stokes fields were generated slightly skewed, supported by the cavity close to the confocal limit with fairly low losses. With a pump pulse duration of 15 ps we could expect to have terahertz frequencies with bandwidth as narrow as 0.033 THz. The generated terahertz also can also be made tunable by tuning the Stokes frequency generated by the polaritons shift utilising the angle dependant nature of SPS. We propose that multiple terahertz frequencies could be controlled by introducing an etalon into the

cavity which could tune the generated terahertz radiation. This forms part of the ongoing future work.

The fact that we generate cavity enhanced Stokes fields rather than using a resonant cavity to enhance the pump itself, avoids the need for nm-scale control of the cavity length to maintain the cavity locking making it much simpler in regard to cavity design. In short, the lithium niobate Raman laser could generate terahertz frequencies with an alternate and simpler approach for terahertz generation from mode-locked picosecond lasers with nanojoule scale energies.

As a matter of future work, lithium niobate Raman laser systems can be modelled which would involve both stimulated Raman scattering as well as stimulated polariton scattering. The laser system is complex enough and a theoretical modelling would help to understand the nuances of the system and to improve the working in regards to power scaling and extending wavelength accessibility. Theoretical modelling would also improve our understanding of generation of terahertz waves from synchronously pumped systems.

Looking back to beginning of the 20th century, it would have been a strenuous task for scientists working in the field of light scattering owing to the absence of many of the light sources and measuring instruments that we often take for granted. But pioneering work in those times carried out by lovers of Science and Nature presented us with interesting truths that have revolutionised our lives. Initial experiments conducted by Raman were based on light from the Sun which was later replaced by a mercury arc lamp, and using a quartz spectrograph the unusual scattering was discovered [12]. We have come a long way from those initial wonderful discovery days, finding newer and exciting applications day after day. I hope that this thesis demonstrating possibilities of wavelength extension, also peeping into the far-infrared in between, forms a humble contribution to this grand phenomenon!

References for Chapter 5:

- [1] G. Eckhardt, D. Bortfeld, M. Geller, Stimulated emission of Stokes and anti-Stokes Raman lines from diamond, calcite and α -sulphur single crystals, *Applied Physics Letters*, 3 (1963) 137-138.
- [2] E. Ammann, C. Decker, 0.9-W Raman oscillator, *Journal of Applied Physics*, 48 (1977) 1973-1975.
- [3] E. Granados, H.M. Pask, D.J. Spence, Synchronously pumped continuous-wave mode-locked yellow Raman laser at 559 nm, *Optics Express*, 17 (2009) 569-574.
- [4] E. Granados, H.M. Pask, E. Esposito, G. McConnell, D.J. Spence, Multi-wavelength, all-solid-state, continuous wave mode locked picosecond Raman laser, *Optics Express*, 18 (2010) 5289-5294.
- [5] P. Straka, J. Nicholson, W. Rudolph, Synchronously pumped H₂ Raman laser, *Optics Communications*, 178 (2000) 175-180.
- [6] D. Chunaev, T. Basiev, V. Konushkin, A. Papashvili, A.Y. Karasik, Synchronously pumped intracavity YLF–Nd–KGW picosecond Raman lasers and LiF:F₂-amplifiers, *Laser Physics Letters*, 5 (2008) 589.
- [7] M. Weitz, C. Theobald, R. Wallenstein, J.A. L'huillier, Passively mode-locked picosecond Nd:YVO₄ self-Raman laser, *Applied Physics Letters*, 92 (2008) 1122.
- [8] D.J. Spence, E. Granados, R.P. Mildren, Mode-locked picosecond diamond Raman laser, *Optics Letters*, 35 (2010) 556-558.
- [9] E. Granados, D.J. Spence, R.P. Mildren, Deep ultraviolet diamond Raman laser, *Optics Express*, 19 (2011) 10857-10863.
- [10] E. Granados, D.J. Spence, Pulse compression in synchronously pumped mode locked Raman lasers, *Optics Express*, 18 (2010) 20422-20427.
- [11] A. Penzkofer, A. Laubereau, W. Kaiser, High intensity Raman interactions, *Progress in Quantum Electronics*, 6 (1979) 55-140.
- [12] R. Singh, CV Raman and the Discovery of the Raman Effect, *Physics in Perspective*, 4 (2002) 399-420.

Publications arising from this thesis

Publications in peer-reviewed journals

- (1) **Aravindan M. Warriar**, Jipeng Lin, Helen M. Pask, Richard P. Mildren, David W. Coutts, David J. Spence, “ *Highly efficient picosecond diamond Raman laser at 1240 nm and 1485 nm*”, Optics Express 22, 3325-3333 (2014).
- (2) **Aravindan M. Warriar**, Jipeng Lin, Helen M. Pask, Andrew J. Lee, David J. Spence, “*Multiwavelength ultrafast LiNbO₃ Raman laser*”, Optics Express 23, 25582-25586 (2015).

Conference paper

- (1) **Aravindan M. Warriar**, Jipeng Lin, Helen M. Pask, Andrew J. Lee, David J. Spence, “*Multiwavelength ultrafast LiNbO₃ Raman laser with cascaded terahertz generation*”, Advanced Solid State Lasers conference ASSL 2015, Adlershof, Germany, Paper AM3A.5

Patent

- (1) David Spence, David Coutts, Richard Mildren, Helen Pask, Jipeng Lin, Aravindan Warriar, “*A method and a system for generating a Raman second Stokes light to a source light*”, (Aust Prov 2013904611, PCT/AU2014/001078, filed on 28 November 2013)

Highly efficient picosecond diamond Raman laser at 1240 and 1485 nm

Aravindan M. Warriar, Jipeng Lin,* Helen M. Pask,
Richard P. Mildren, David W. Coutts, and David J. Spence

MQ Photonics, Department of Physics and Astronomy, Macquarie University, NSW 2109, Australia.

**Jipeng.lin@mq.edu.au*

Abstract: We present a highly efficient picosecond diamond Raman laser synchronously-pumped by a 4.8 W mode-locked laser at 1064 nm. A ring cavity was adopted for efficient operation. With a low-Q cavity for first-Stokes 1240 nm, we have achieved 2.75 W output power at 1240 nm with 59% overall conversion efficiency. The slope efficiency tended towards 76% far above the SRS threshold, approaching the SRS quantum limit for diamond. A high-Q first-Stokes cavity was employed for second-Stokes 1485 nm generation through the combined processes of four-wave mixing and single-pass stimulated Raman scattering. Up to 1.0 W of second-stokes at 1485 nm was obtained, corresponding to 21% overall conversion efficiency. The minimum output pulse duration was compressed relative to the 15 ps pump, producing pulses as short as 9 ps for 1240 nm and 6 ps for 1485 nm respectively.

©2014 Optical Society of America

OCIS codes: (140.3550) Lasers, Raman; (140.7090) Ultrafast lasers; (140.3580) Lasers, solid-state; (140.3560) Lasers, ring.

References and links

1. H. M. Pask, "The design and operation of solid-state Raman lasers," *Prog. Quantum Electron.* **27**, 3-56 (2003).
2. P. Cerny, H. Jelinkova, P. G. Zverev, and T. T. Basiev, "Solid state lasers with Raman frequency conversion," *Prog. Quantum Electron.* **28**, 113-143 (2004).
3. H. M. Pask, P. Dekker, R. P. Mildren, D. J. Spence, and J. A. Piper, "Wavelength-versatile visible and UV sources based on crystalline Raman lasers," *Prog. Quantum Electron.* **32**, 121-158 (2008).
4. B. I. Carman, F. Shimizu, C. S. Wang, and N. Bloembergen, "Theory of Stokes pulse shapes in transient stimulated Raman scattering," *Phys. Rev. A* **2**, 60 (1970).
5. P. Cerny and H. Jelinkova, "Near-quantum-limit efficiency of picosecond stimulated Raman scattering in BaWO₄ crystal," *Opt. Lett.* **27**, 360-362 (2002).
6. M. Weitz, C. Theobald, R. Wallenstein, and J. A. L'huillier, "Passively mode-locked picosecond Nd:YVO₄ self-Raman laser," *Appl. Phys. Lett.* **98**, 091122 (2008).
7. D. S. Chunaev, T. T. Basiev, V. A. Konushkin, A. G. Papashvili, and A. Y. Karasik, "Synchronously pumped intracavity YLF-Nd-KGW picosecond Raman lasers and LiF:F²⁺-amplifiers," *Laser Phys. Lett.* **5**, 589-592 (2008).
8. G. G. Grigoryan and S. B. Sogomonyan, "Synchronously pumped picosecond Raman laser utilizing a LiIO₃ crystal," *Soviet J Quantum Electron.* **19**, 1402 (1989).
9. E. Granados, H. M. Pask, and D. J. Spence, "Synchronously pumped continuous-wave mode-locked yellow Raman laser at 559 nm," *Opt. Expr.* **17**, 569-574 (2009).
10. D. J. Spence, E. Granados, and R. P. Mildren, "Mode-locked picosecond diamond Raman laser," *Opt. Lett.* **35**, 556-558 (2010).
11. E. Granados, D. J. Spence, and R. P. Mildren, "Deep ultraviolet diamond Raman laser," *Opt. Expr.* **19**, 10857-10863 (2011).
12. E. Granados, H. M. Pask, E. Esposito, G. McConnell, and D. J. Spence, "Multi-wavelength, all-solid-state, continuous-wave mode-locked picosecond Raman laser," *Opt. Expr.* **18**, 5289-5294 (2010).
13. R. P. Mildren, "Intrinsic optical properties of diamond," in *Optical Engineering of Diamond*, 2013, pp. 1-34.
14. T. T. Basiev, A. A. Sobol, P. G. Zverev, V. V. Osiko, and R. C. Powell, "Comparative spontaneous Raman spectroscopy of crystals for Raman lasers," *Appl. Opt.* **38**, 594-598 (1999).
15. J.-P. M. Feve, K. E. Shortoff, M. J. Bohn, and J. K. Brasseur, "High average power diamond Raman

- laser,” *Opt. Expr.* **19**, 913–22, 2011.
16. A. McKay, H. Liu, O. Kitzler, and R. P. Mildren, “An efficient 14.5 W diamond Raman laser at high pulse repetition rate with first (1240 nm) and second (1485 nm) Stokes output,” *Laser Phys. Lett.* **10**, 105801, 2013.
 17. R. P. Mildren, A. Sabella, O. Kitzler, D. J. Spence, and A. M. McKay, “Diamond Raman laser design and performance,” in *Optical Engineering of Diamond*, 2013, pp. 239–276.
 18. A. Sabella, J. A. Piper, and R. P. Mildren, “1240 nm diamond Raman laser operating near the quantum limit,” *Opt. Lett.* **35**, 3874–3876 (2010).
 19. Q. Fu, G. Mak, and H. M. Driel, “High-power, 62-fs infrared optical parametric oscillator synchronously pumped by a 76-MHz Ti:sapphire laser,” *Opt. Lett.* **17**, 1006–1008 (1992).
 20. E. Granados and D. J. Spence, “Pulse compression in synchronously pumped mode locked Raman lasers,” *Opt. Expr.* **18**, 20422–20427 (2010).
 21. Tasoltan T Basiev, Maxim E Doroshenko, Lyudmila I Ivleva, Sergei N Smetanin, M Jelínek, V Kubeček and H Jelínková, “Four-wave-mixing generation of SRS components in BaWO₄ and SrWO₄ crystals under picosecond excitation,” *Prog. Quantum Electron.* **43**, 616–620 (2013).
 22. R. L. Carman, F. Shimizu, C. S. Wang, and N. Bloembergen, “Theory of Stokes pulse shapes in transient stimulated Raman scattering,” *Physics Review A* **2**, 60–72 (1970).
 23. J. R. Murray, J. Goldhar, D. Eimerl, and A. Szoke, “Raman pulse compression of excimer lasers for application to laser fusion,” *IEEE J. of Quantum. Electro.* **15**, 342–368 (1979).
 24. S. F. Morozov, L. V. Piskunova, M. M. Sushchik and G. I. Freidman, “Formation and amplification of quasi-soliton pulses in head-on stimulated scattering,” *Sov. J. Quantum Electron.* **8**, 576 (1978).
 25. D. S. Chunaev and A. Y. Karasik, “Temporal characteristics of picosecond stimulated Raman scattering in oxide crystals,” *Laser Phys.* **16**, 1668–1671 (2006).

1. Introduction

Raman lasers that utilise stimulated Raman scattering (SRS) are practical devices that can frequency-shift the output of a conventional laser to a hard-to-reach spectral region [1, 2]. The cascading nature of SRS also allows the first-Stokes line to be shifted to second- or higher Stokes fields. The wavelength range can be further extended by combining other nonlinear process such as second-harmonic generation (SHG) or sum-frequency generation (SFG), enabling wavelength-versatile output from a single laser source [3]. Recently, there has been progress in translating these wavelength conversion versatilities to the picosecond domain.

Picosecond Raman lasers are attractive sources for many nonlinear optical applications that require non-standard wavelengths. For picosecond operation where the pump laser pulse duration is similar or shorter than the Raman transition dephasing time T_2 (typically T_2 is of the order of 1–10 ps for crystalline Raman materials), the system operates in the so-called transient regime, in contrast to the steady-state regime for CW and nanosecond operation; in general, Raman gain in the transient regime is smaller for a given peak intensity than that in the steady-state regime [4].

Picosecond Raman lasers can be simple single- or double-pass converters, which require high pump pulse energy of the order of hundreds of μJ or even mJ to reach the SRS threshold [5]. The SRS threshold can be significantly reduced by placing the Raman material within the cavity of the pump laser, such as demonstrated in [6, 7]: this exploits the high intracavity pump power, but complicates the ultrafast pulse formation dynamics and may be problematic for sub-picosecond lasers. Alternatively, a separate external Raman cavity can be used, but for ultrafast pulse trains, this requires use of a synchronous pumping scheme. For this, the external cavity length is matched to the pump laser cavity such that an intense circulating intracavity Stokes pulse is maintained at steady-state by amplification by each successive pump pulse in the pulse train. While some studies have used Q-switched mode-locked pump lasers with μJ or mJ pulse energies [8], this method also enables Raman conversion of trains of CW-mode-locked pump pulses having nJ energies, and has been successfully employed to generate picosecond Raman output in the visible [9, 10] and UV [11] regions. Furthermore, the Raman cavity mirror coatings can be designed to cascade the first-Stokes to higher order Stokes fields. In 2010, Granados *et al.* [12] reported a cascaded synchronously-pumped CW mode-locked Raman laser. A 50 mm-long KGW crystal was pumped by a frequency-doubled

Nd:YVO₄ laser that yielded 7 W at 532 nm, with 28 ps pulses in an 80 MHz pulse train. Both first-Stokes (559 nm) and second-Stokes (589 nm) pulses were resonated in the synchronized standing-wave Raman cavity, resulting in 2.5 W output power for 559 nm and 1.4 W for 589 nm, with 35.7% and 20% overall conversion efficiency respectively. It was important to carefully manage the group velocity dispersion of the two Stokes wavelengths using dispersion elements to enable efficient conversion.

In this paper, we report picosecond Raman laser operation by using a synchronous pumping scheme in a ring cavity configuration. Using diamond as the Raman medium, we demonstrate several important features of this type of architecture including a selectable method for uni-directional forwards and backwards operation, and efficient second-Stokes generation in a singly resonant cavity. We show that the second-Stokes output is generated in the forward direction through the combined processes of four-wave mixing (FWM) and single-pass SRS, which enables Raman cavity mirror coatings to be simplified. Up to 1.0 W output power was obtained in the eye-safe region at 1485 nm, corresponding to 21% overall conversion efficiency. Backwards SRS was also observed in the high-Q cavity, and we discuss future prospects for strong pulse-compression.

2. Experimental setup

The optical schematic of experimental setup is shown in Fig. 1. For the Raman crystal we used CVD-grown diamond. Diamond was chosen for its high Raman gain coefficient and large Raman shift of 1332 cm⁻¹ [13, 14]. Even with its relatively long phonon dephasing time of 7.1 ps [13], it is surpassed only by LiNbO₃ for transient gain for few-ps pump pulses [14]. Diamond also has outstanding thermal and mechanical properties that enable efficient Raman conversion for high power operation [15-17]. An 8 mm-long rectangular diamond crystal, with anti-reflective coating at 1240 nm ($R=0.06\%$ per pass for each end-face), was oriented such that the pump beam propagated along the $\langle 110 \rangle$ axis and was polarized along the $\langle 111 \rangle$ axis in order to access the maximum Raman gain of the diamond crystal [18]. The diamond crystal was pumped by a CW mode-locked Nd:YVO₄ laser (*Spectra Physics Vanguard 2000-HM532*) that generated up to 4.8 W average power at 1064 nm with pulse duration of 15 ps, repetition rate of 80 MHz, and beam quality factor M^2 of 1.1. The incident pump power could be attenuated by using a half-waveplate and a polarizer beam-splitting cube without otherwise changing the operating characteristics of the pump laser. Two plano-convex lenses ($f_1 = 500$ mm and $f_2 = 200$ mm) were used to focus the pump beam through the input mirror M1 into the center of the diamond crystal with a focal spot size $\omega_P = 22$ μm .

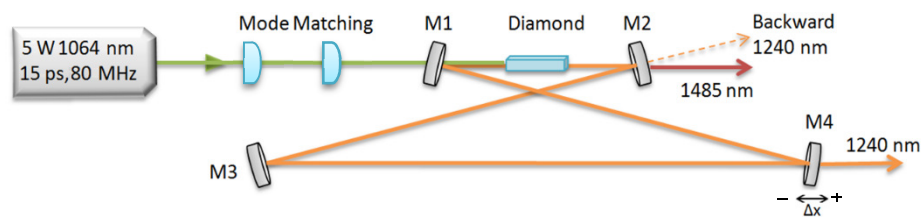


Fig. 1. Optical schematic of the synchronously-pumped diamond Raman laser.

The external diamond Raman laser cavity was a bow-tie shaped ring cavity composed of two curved mirrors (M1 and M2, ROC = 200 mm) and two flat mirrors (M3 and M4). The coating specifications for each mirror are summarized in Table 1. Two different M4 mirrors (M4₁ and M4₂) were used for first-Stokes and second-Stokes operation respectively. For first-Stokes operation, the majority of the output power was obtained from M4₁ ($T = 8.3\%$ at 1240 nm) while M2 ($T = 0.4\%$ at 1240 nm) also leaked a small amount output power. For

second-Stokes operation, M4₂ (R > 99.99% at 1240 nm) was used to increase the intracavity intensity of the first-Stokes field, while M2 operated as the output coupler (OC) for both first- and second-Stokes. A separation of approximately 205 mm between M1 and M2 produced a resonator TEM₀₀ mode at the center of the diamond with a similar mode size ($\omega_0 = 20 \mu\text{m}$) to the focused pump. To optimize the laser performance, the Raman cavity had to be synchronized with the pump laser: the cavity length was tuned by changing the position of M4 with a high precision translation stage. The cavity length detuning Δx was defined so that $\Delta x = 0 \mu\text{m}$ was the length that resulted in the lowest laser threshold, with a positive (negative) Δx corresponding to a longer (shorter) cavity.

Table 1: Summary of mirror coatings.

Mirror	1064 nm	1240 nm	1480 nm
M1, M3	T = 93%	R > 99.99%	T = 90%
M2	--	T = 0.4%	T = 91%
M4 ₁	--	T = 8.3%	--
M4 ₂	--	R > 99.99%	T = 85%

There are several advantages of using a ring cavity over the standing-wave cavity used previously in synchronously-pumped Raman lasers [9-12]. In a standing-wave cavity, the intracavity Stokes field is predominantly amplified when traveling forward together with the pump pulse along the Raman crystal; the return pass through the crystal can provide a small level of additional gain if the (potentially strongly) depleted pump power is also returned from the end mirror, but at the expense of almost doubled round-trip losses. A ring cavity design thus does not strongly reduce the round-trip Raman gain and can almost halve the round-trip losses compared to a standing-wave cavity. This is especially important in the present case where our cavity losses are mostly accounted for by scattering and surface losses associated with the Raman crystal. The synchronously pumped ring Raman laser will ordinarily provide unidirectional operation without requiring an intracavity optical diode, owing to enhanced temporal overlap of the pump and co-propagating Stokes pulses through the Raman crystal; this is discussed in more detail below. Finally, an external ring cavity gives no back-reflections to the pump laser system, avoiding the potential need for an isolator between the cavity and the pump laser. These advantages for ring cavities are of course in common with $\chi^{(2)}$ optical parametric oscillators (OPOs), e.g. [19], which share the similarity of being a gain system with no energy storage in the gain media.

We have in previous work [10, 11] used Brewster-cut diamond crystals. The advantage of this is that with the Brewster crystal the cavity astigmatism can be completely compensated, and surface losses can be extremely low; the disadvantage is that the threshold of the laser is increased by a factor of 2.4 by the elongation of the cavity waist in the tangential plane. In the present work using a plane-cut crystal, the cavity folding angle was kept as small as possible, approximately 5 degrees, to minimise astigmatism and AR coatings limited the surface losses to 0.06% per face.

3. Low-Q first-Stokes (1240 nm) cavity

To generate first-Stokes output, we built a low-Q first-Stokes cavity using M4₁ as the output coupler (OC). The first-Stokes intracavity field was unidirectional, lasing in the “forward” direction defined as that co-propagating with the incident pump beam. Note that in contrast to OPOs, synchronous Raman lasers can lase in the backwards direction, as the underlying Raman gain coefficient is the same for forwards- and backwards-SRS in crystals. Geometric factors will in general favor forward operation: the overlap time for a 15 ps pump pulse and any point moving with the Stokes pulse envelope is 64 ps for a forward Stokes pulse (corresponding to the full 8-mm crystal length) but only 7.5 ps for a backwards Stokes pulse (corresponding to the collision time of the pulses). We see then the geometry will strongly

favor forwards operation unless the crystal length is significantly shortened. This is discussed again below where we nevertheless observe backward Stokes oscillation.

Fig. 2 shows the first-Stokes threshold, output power and pulse duration as a function of cavity length detuning Δx , where the output power and pulse duration were measured at the maximum pump power of 4.8 W. Changing Δx results in a very slight change in the cavity alignment, minimised in our geometry where the cavity has a very small folding angle; we re-optimised the cavity alignment at each Δx to minimise this effect. First-Stokes output was obtained within a detuning range of $\Delta x = -400$ to $+45 \mu\text{m}$. The minimum SRS threshold was 1.53 W at $\Delta x = 0 \mu\text{m}$ (by definition), where the maximum output power of 2.75 W at 1240 nm was also obtained. Power transfer data for $\Delta x = 0 \mu\text{m}$ is plotted in Fig. 3. We have achieved an overall conversion efficiency $\eta_o = 59\%$. Far above the SRS threshold (above 3.5 W pump power), the residual pump power started to clamp and the slope efficiency η_s tended towards a limit of 76%; this is not far below the quantum limit of 86% for diamond indicating a very efficient laser. The beam quality factor M^2 for the 1240 nm output was measured to be 1.55 at the maximum output power.

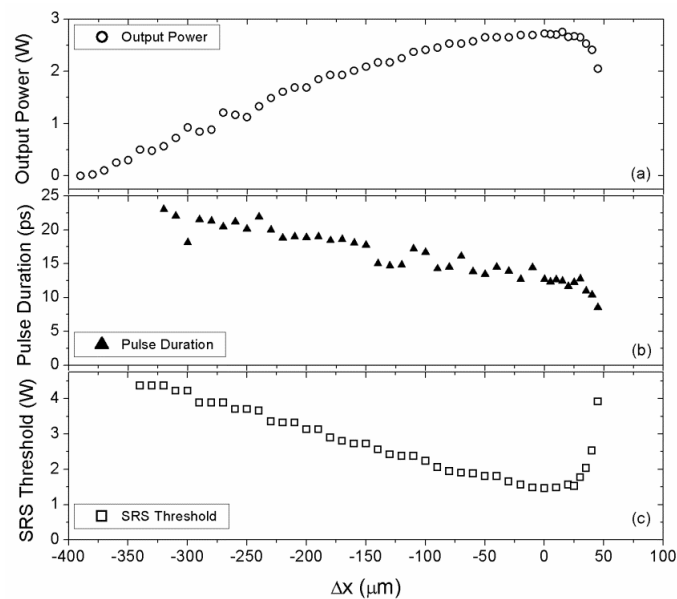


Fig. 2. Maximum output power (a), pulse duration (b) and SRS threshold (c) of the 1240 nm laser output as a function of cavity length detuning Δx . The maximum output power and pulse duration data were measured for an incident pump power of 4.8 W.

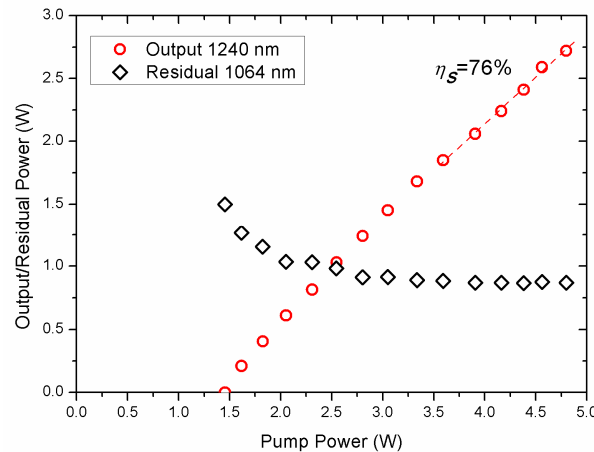


Fig. 3. Power transfer diagram of 1240 nm laser output and residual pump power at $\Delta x = 0 \mu\text{m}$.

The first-Stokes generation in this work was much more efficient than the synchronously-pumped Raman lasers reported previously, e.g. $\eta_o=25.6\%$, $\eta_s=42\%$ in [9], $\eta_o=29\%$, $\eta_s=41\%$ in [10] and $\eta_o=10.3\%$, $\eta_s=25\%$ in [11]. The improvement is mainly attributed to the ring-cavity configuration for the present work, as well as superior coatings for both the cavity mirrors and Raman crystal used in this work. To indicate the significance of intracavity losses affecting the laser performance, we used another diamond having similar length (10 mm) and orientation but higher end-face reflectivity ($R = 0.4\%$ per end-face, compared to $R = 0.06\%$), and obtained a reduced output power at 1240 nm of 2.1 W and $\eta_o = 43.8\%$ (compared to 2.75 W and $\eta_o = 59\%$).

The pulse duration of the first-Stokes output was measured with an autocorrelator assuming that the pulses were Gaussian in time, and the measurement results are shown in Fig. 2 (b). The minimum pulse duration of 9 ps at 1240 nm was obtained at $\Delta x = +45 \mu\text{m}$. The effect of pulse-compression in this work was however much less prominent compared to previous reports [9-11]. Compression relies on the group delay difference between the pump and Stokes pulses transiting the crystal [20], which is relatively low in the current experiment: the diamond crystal is shorter than the KGW crystal employed in [9], and provides less dispersion compared to that for visible- or UV-pumped lasers reported in refs [10, 11].

4. High-Q first-Stokes (1240 nm) cavity

We also operated the laser with a different output coupler M4₂ that had a HR coating at 1240 nm. With this setup, the round trip loss at 1240 nm from the mirrors was dominated by the 0.4% transmission through M2, and the intracavity intensity of the first-Stokes field, monitored through the power leaking from M2, was significantly increased. We observed forward generation of second-Stokes at 1485 nm, as well as backward generation of first-Stokes at 1240 nm in certain detuning regions. The performances of the second-Stokes and backward first-Stokes are discussed separately in the following subsections.

4.1 Second-Stokes (1485 nm) output

We found that this laser could efficiently generate second-Stokes output, despite the fact that the second-Stokes radiation was extremely weakly resonated, with only 0.02% of the second-Stokes power at the exit of the crystal circulated for the next round trip. The laser performance as a function of Δx is summarized in Fig. 4, showing that the second-Stokes 1485 nm was operating in a narrower Δx region (from $-105 \mu\text{m}$ to $+22 \mu\text{m}$) compared to the first-Stokes described in the previous section. The maximum 1485 nm output power was 1.0 W at $\Delta x = 0 \mu\text{m}$ with 4.8 W pump power, corresponding to $\sim 21\%$ overall conversion

efficiency. The 1485 nm output pulse duration was around 10 ps for most of the negative Δx cavity detuning range and dropped steeply for positive detuning. The shortest pulse duration was 6 ps at $\Delta x = +20 \mu\text{m}$. The measured beam quality factor M^2 was ~ 2.2 for the maximum output power.

We also observed a small collinear output at 935 nm corresponding to the anti-Stokes wavelength. To further investigate the behaviour of this laser, we measured the second-Stokes, anti-Stokes and first-Stokes power coupled from M2 as well as residual pump power as a function of pump power, shown in Fig. 5. The presence of anti-Stokes generation points to parametric four-wave-mixing, where two pump photons create a Stokes and anti-Stokes pair. With a strong pump field, and a collinear resonated Stokes field, this process can be strong. In the collinear geometry, the parametric process is not phase matched, and the wave vector mismatch can be written $\Delta k_{AS} = 2k_P - \Delta k_S - \Delta k_{AS}$ where k_P , k_S , k_{AS} are the wave vectors of the pump, Stokes, and anti-Stokes fields. For diamond, with a pump wavelength of 1064 nm, $\Delta k_{AS} = 8065 \text{ m}^{-1}$ [14], corresponding to a dephasing length of $390 \mu\text{m}$. Along the 8-mm-long diamond crystal then, the anti-Stokes will be created and back-converted several times as the nonlinear polarization at the anti-Stokes frequency comes in and out of phase with the propagating anti-stokes wave; the anti-Stokes output that we see is a result of generation over just part of a dephasing length at the exit of the crystal. Note that phase-matched generation of Stokes and anti-Stokes beams that are both non-collinear with the pump beam is negligible in this case, owing to the presence of the strong collinear Stokes beam.

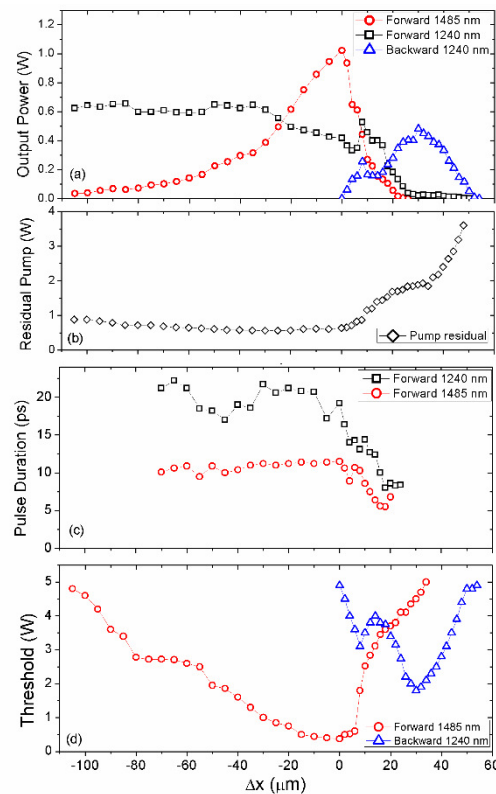


Fig. 4. (a) Maximum output power, (c) pulse duration, and (d) threshold of the 1485 nm laser output as a function of cavity length detuning Δx . The leaking forward 1240 nm (a) and residual pump power (b) was also characterized. Backward 1240 nm was obtained in the region $\Delta x = 0$ to $+55 \mu\text{m}$. The maximum output power, residual pump power and pulse duration were measured for an incidence pump power of 4.8 W.

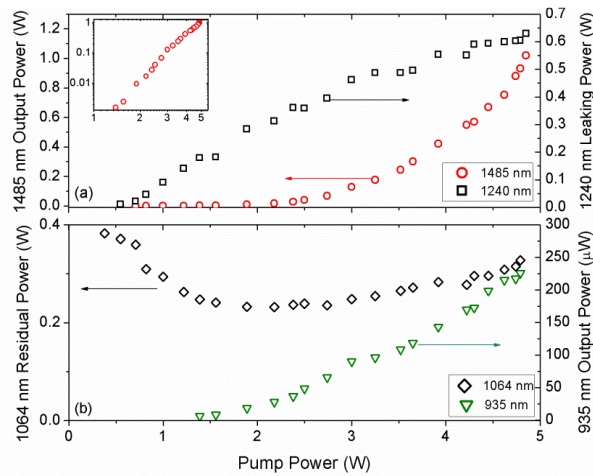


Fig. 5. (a) Second-Stokes (1485 nm) output power and first-Stokes (1240 nm) leaking power, (b) residual fundamental (1064 nm) power and anti-Stokes (935 nm) output power as a function of pump power at $\Delta x = 0 \mu\text{m}$. The inset in (a) shows the second-Stokes output power vs. pump power on a log-log plot. The anti-Stokes power below 1.4 W pump power was not measured owing to the limited sensitivity of the power meter used in the experiment.

Parametric generation of the second Stokes also occurs via phase-mismatched FWM, where the second-Stokes wave vector mismatch $\Delta k_{SS} = 2k_S - \Delta k_P - \Delta k_{SS}$ is 6857 m^{-1} in our case. Second-Stokes generation should be much stronger than for anti-Stokes: the former is proportional to $P_P P_S^2$, whereas the latter is proportional to $P_P^2 P_S$ where P_P and P_S are the pump and Stokes intracavity power, and in this laser the cavity-enhanced Stokes field is substantially the stronger of the two except very close to threshold. In contrast to the anti-Stokes wave, the second-Stokes wave will of course also see SRS gain pumped by the Stokes field. We suggest that the parametric generation of second-Stokes seeds the SRS process, generating the second-Stokes field in a single-pass; the weakly-resonated second-Stokes field is negligible in this case. This interpretation is also supported by the threshold-less behaviour of the second-Stokes, seen clearly in the inset of Fig. 5(a), and in the anti-Stokes. The combination of FWM and single-pass SRS for generating the second-Stokes output represents a practically convenient method for efficient generation. The cavity mirrors are not required to have reflectivity at the second-Stokes wavelength, nor is there a requirement for intracavity dispersion management as was used in [12]. We note that FWM seeding of cascaded Stokes generation has been studied previously in different SRS experiments, for example [21].

4.2 Backwards generation at the first-Stokes (1240 nm)

With the high-Q cavity used for second-Stokes operation, backwards propagating first-Stokes output was also obtained for small positive length detunings of $\Delta x = 0$ to $+55 \mu\text{m}$. The output power and threshold for the backward first-Stokes output as a function of Δx are characterized in Fig. 4(a) and 4(d) respectively. The maximum output power for the backward 1240 nm was 0.45 W at $\Delta x = +27 \mu\text{m}$. The pulse duration along the whole operating region was $> 30 \text{ ps}$, limited by the scanning range of the autocorrelator, much longer than that for the forward first-Stokes. We must explain why backwards operation was observed given our observation above that geometric factors should favour forward operation by a large factor. The answer lies in the complexities of the synchronization effects, acting differently for forwards and backwards operation depending on Δx .

In general, the forward SRS operates best for cavity lengths that are matched, or a little shorter than the pump laser (negative detuning), as shown in Fig. 2 and Fig 4(a). For negative detunings, the steady-state Stokes pulse must be preferentially amplified in its tail to reshape the pulse to cause an effective delay, counteracting the fact that it is advanced on each round trip owing to the cavity length mismatch. Preferential amplification of the tail

is consistent with transient Raman scattering [22], and so large negative detuning can be tolerated [20]. Efficient operation of the forward-Stokes leads to strong depletion of the pump field as shown in Fig. 3 and Fig. 4(b), and so backward-Stokes operation does not reach its threshold. Positive detuning on the other hand require preferential amplification of the leading edge of the Stokes pulse: this is not easily achieved causing forward-Stokes laser output to fall below threshold for significant positive detuning. In this regime, however, the suppressed forward operation appears to enable backward-Stokes operation to achieve threshold.

The pulse forming dynamics for the colliding pump and backwards Stokes fields clearly permits operation for larger positive detuning. In future, we plan to adapt the model procedure described in [20] to quantitatively examine operation in this regime and investigate ways backwards operation can be enhanced. For example, the Raman cavity could be forced to operate in the pure backward direction by introducing an intracavity optical isolator to prevent the forward Stokes field from oscillating. Strong compression in backward SRS amplifiers is well studied in gases, with order-of-magnitude or more compressions possible [23], and potential compression down to pulse durations as short as $0.1T_2$ [24] corresponding to 720 fs for diamond, and 38 fs for LiNbO_3 [25]. Backwards operation in a synchronously pumped ring laser, in which the leading edge of the backward Stokes pulse collides with the undepleted pump pulse on each round trip, thus may provide a promising method for enabling steepened and substantially shortened pulses.

6. Conclusion

In summary, we have demonstrated a highly efficient picosecond diamond Raman laser operating at both 1240 nm and 1485 nm. Up to 2.75 W output power and 59% conversion efficiency were achieved for the first-Stokes 1240 nm in a low-Q Raman cavity. The slope efficiency tended towards 76% when the pump was far above the SRS threshold. The second-Stokes 1485 nm was efficiently generated through FWM and single-pass SRS without being resonated in a high-Q Raman cavity. We have generated 1.0 W output power at 1485 nm with 21% overall conversion efficiency. The ring laser design is a convenient design for enabling separate investigation of forwards and backwards operation. The system has great potential in power scaling for the Stokes generation owing to the high slope efficiency far above the SRS threshold and to the superior thermal properties of diamond.

Acknowledgements

This work was funded by an Australian Research Council Linkage Project LP110200545, in association with M Squared Lasers Ltd. Aravindan Warriar is supported by a Macquarie University iMQRES scholarship.

Multiwavelength ultrafast LiNbO₃ Raman laser

Aravindan M. Warriar,* Jipeng Lin, Helen M. Pask, Andrew J. Lee, David J. Spence.

MQ Photonics Research Centre, Department of Physics and Astronomy, Macquarie University, NSW 2109, Australia

*aravindan.madhava-warrier@students.mq.edu.au

Abstract: We present a multiwavelength ultrafast Raman laser based on lithium niobate which uses polariton scattering in combination with Raman scattering to selectively generate new wavelengths from a nanojoule-scale picosecond pump laser. Pumped by a 1064 nm pump laser, the system generates 1123 nm by stimulated polariton scattering (SPS) and 1140 nm by stimulated Raman scattering (SRS). Cascading of these intracavity fields generates 1155 nm and 1174 nm, as well as generating THz output.

©2015 Optical Society of America

OCIS codes: (140.3550) Lasers, Raman; (240.5420) Polaritons; (190.5890) Scattering stimulated.

References and links

1. Q. Fu, G. Mak, and H. Van Driel, "High-power, 62-fs infrared optical parametric oscillator synchronously pumped by a 76-MHz Ti:sapphire laser," *Opt. Lett.* **17**, 1006-1008 (1992).
2. E. Cheung and J. Liu, "Theory of a synchronously pumped optical parametric oscillator in steady-state operation," *J. Opt. Soc. Am. B* **7**, 1385-1401 (1990).
3. Y. Takida, T. Ohira, Y. Tadokoro, H. Kumagai, and S. Nashima, "Tunable picosecond terahertz-wave parametric oscillators based on noncollinear pump-enhanced signal-resonant cavity," *Sel. Top. Quant. Electron.* **19**, 8500307-8500307 (2013).
4. M. Colles, "Ultrashort Pulse Formation in a Short-Pulse-Stimulated Raman Oscillator," *Appl. Phys. Lett.* **19**, 23-25 (1971).
5. G. G. Grigoryan and S. Sogomonyan, "Synchronously pumped picosecond Raman laser utilizing an LiIO₃ crystal," *Sov. J. Quant. Electron.* **19**, 1402 (1989).
6. D. Chunaev, T. Basiev, V. Konushkin, A. Papashvili, and A. Y. Karasik, "Synchronously pumped intracavity YLF–Nd–KGW picosecond Raman lasers and LiF:F₂-amplifiers," *Laser Phys. Lett.* **5**, 589 (2008).
7. M. Weitz, C. Theobald, R. Wallenstein, and J. A. L'huillier, "Passively mode-locked picosecond Nd: YVO₄ self-Raman laser," *Appl. Phys. Lett.* **92**, 1122 (2008).
8. E. Granados, H. M. Pask, and D. J. Spence, "Synchronously pumped continuous-wave mode-locked yellow Raman laser at 559 nm," *Opt. Expr.* **17**, 569-574 (2009).
9. E. Granados, D. J. Spence, and R. P. Mildren, "Deep ultraviolet diamond Raman laser," *Opt. Expr.* **19**, 10857-10863 (2011).
10. M. Murtagh, J. Lin, R. P. Mildren, and D. J. Spence, "Ti:sapphire-pumped diamond Raman laser with sub-100-fs pulse duration," *Opt. Lett.* **39**, 2975-2978 (2014).
11. M. G. Pullen, J. J. Chapman, and D. Kielpinski, "Efficient generation of > 2 W of green light by single-pass frequency doubling in PPMgLN," *Appl. Optics* **47**, 1397-1400 (2008).
12. H. Furuya, A. Morikawa, K. Mizuuchi, and K. Yamamoto, "High-beam-quality continuous wave 3 W green-light generation in bulk periodically poled MgO:LiNbO₃," *Jpn. J. Appl. Phys.* **45**, 6704 (2006).
13. M. Ebrahimzadeh, P. Phillips, and S. Das, "Low-threshold mid-infrared optical parametric oscillation in periodically poled LiNbO₃ synchronously pumped by a Ti:sapphire laser," *Appl. Phys. B* **72**, 793-801 (2001).
14. H. Puthoff, R. Pantell, B. Huth, and M. Chacon, "Near-Forward Raman Scattering in LiNbO₃," *Appl. Phys.* **39**, 2144-2146 (1968).
15. J. Yarborough, S. Sussman, H. Purhoff, R. Pantell, and B. Johnson, "Efficient, tunable optical emission from LiNbO₃ without a resonator," *Appl. Phys. Lett.* **15**, 102-105 (1969).
16. K. Kawase, M. Sato, T. Taniuchi, and H. Ito, "Coherent tunable THz-wave generation from LiNbO₃ with monolithic grating coupler," *Appl. Phys. Lett.* **68**, 2483-2485 (1996).
17. A. S. Barker and R. Loudon, "Dielectric Properties and Optical Phonons in LiNbO₃," *Phys. Rev.* **158**, 433-445 (1967).
18. D. J. Spence, E. Granados, and R. P. Mildren, "Mode-locked picosecond diamond Raman laser," *Opt. Lett.* **35**, 556-558 (2010).
19. Y. N. Polivanov, "Raman scattering of light by polaritons," *Sov. Phys. Uspekhi* **21**, 805 (1978).
20. D. Preuss and J. Gole, "Three-stage birefringent filter tuning smoothly over the visible region: theoretical treatment and experimental design," *Appl. Optics* **19**, 702-710 (1980).

1. Introduction

Wavelength conversion of nanojoule-scale picosecond pulses from unamplified oscillators is often achieved using synchronous pumping of an external cavity, where the wavelength-shifted pulse is resonated with the same roundtrip-time as the pump oscillator, with repetitive amplification driven by each pulse in the pump train. Synchronous pumping is well established for both $\chi^{(2)}$ optical parametric oscillators [1-3] and $\chi^{(3)}$ Raman lasers [4-10].

Lithium niobate (LiNbO_3), a negative uniaxial crystal, is one of the most-studied materials for nonlinear frequency conversion due to its large $\chi^{(2)}$ and $\chi^{(3)}$ nonlinear coefficients and its transparency over a wide wavelength range (0.4-5.5 μm). Lithium niobate has been most widely used for frequency doubling and optical parametric oscillator applications in the visible and infrared [11-13] but has also been used as a Raman-active material [14-16] to generate wavelengths in the IR and THz regions.

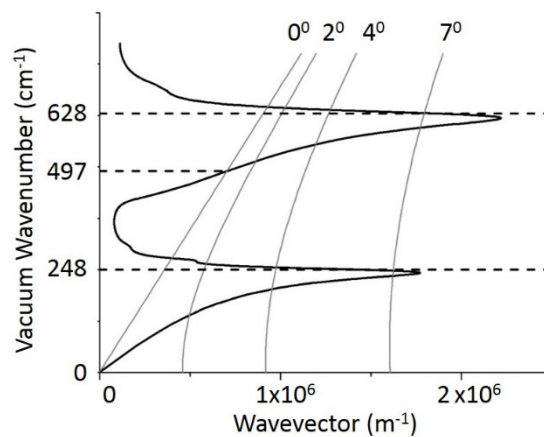


Fig. 1 Dispersion curve of lithium niobate calculated using data from [17] with phase matching curves for small angle scattering of a 1064 nm pump laser.

Lithium niobate has two strong vibrational modes with wavenumbers 248 cm^{-1} and 628 cm^{-1} [17]. These vibrations of polar bonds produce coupled electromagnetic-vibrational modes of mixed photon-phonon character called polaritons. Stimulated polariton scattering (SPS) is an inelastic process that involves both $\chi^{(2)}$ and $\chi^{(3)}$ interactions. Unlike stimulated Raman scattering (SRS), in SPS the frequency shift is a function of the angle between the pump and Stokes fields, determined by the intersection of the phase matching curves and the polariton dispersion curve shown in Fig. 1.

The polariton associated with the 248 cm^{-1} vibrational mode generates THz radiation for angles of a few degrees between the pump and Stokes fields; for angles $\geq 7^\circ$ the polariton is predominantly vibrational in nature and tends to a resonant frequency of 248 cm^{-1} . The polariton associated with the 628 cm^{-1} vibrational mode has a resonant frequency of 497 cm^{-1} for co-propagating pump and Stokes; for angles $\geq 7^\circ$ the polariton is predominantly vibrational in nature and tends to a resonant frequency of 628 cm^{-1} .

In this paper we present a synchronously-pumped Raman laser that uses these different scattering frequencies to switchably or simultaneously convert the pump light to a set of new wavelengths.

2. Laser operation

The experimental setup comprised a synchronously-pumped ring resonator as shown in Fig. 2. We used a 20 mm x-cut 5-mol% MgO-doped LiNbO_3 crystal (HC Photonics Corp.) with antireflection-coated end faces ($R < 0.2\%$ from 1064 to 1085 nm and $R < 0.5\%$ from 1120 to 1180 nm).

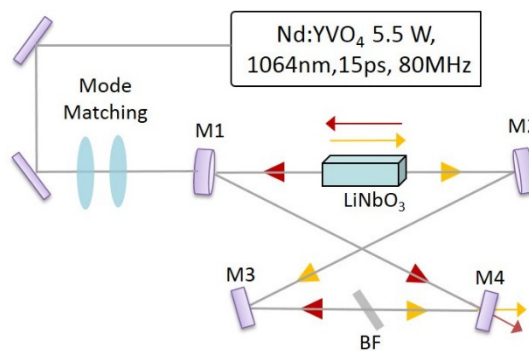


Fig. 2. Experimental schematic showing the LiNbO₃ crystal positioned in the waist of a bow tie ring cavity. Yellow arrows represent clockwise propagating Stokes fields and red arrows represent counter-clockwise propagating Stokes fields.

Two concave mirrors (M1 and M2, ROC = 100 mm) and two flat mirrors (M3 and M4) made up the bow-tie cavity. A separation of approximately 110 mm between M1 and M2 produced a resonator mode at the center the crystal with a radius of 22 μm . The crystal was pumped by a CW mode-locked Nd:YVO₄ laser (Spectra Physics Vanguard 2000-HM532) that generated up to 5.5 W average power at 1064 nm with pulse duration of 15 ps, repetition rate of 80 MHz, and a beam quality factor M^2 of 1.1. A pair of plano-convex lenses ($f_1 = 500$ mm, $f_2 = 150$ mm) were used for mode matching the pump beam to the cavity mode. The input coupler M1 had high transmission at 1064 nm in order to admit the pump light, and a high reflectivity between 1110 nm and 1180 nm, while the output coupler M4 had significant transmission only above 1180 nm, with approximately 1% transmittance for the Stokes wavelengths observed.

The Raman cavity was synchronized with the pump laser such that the cavity round trip time was matched to the time between consecutive laser pulses, the cavity length being tuned by changing the position of M4 with a high-precision translation stage. Aspects of laser optimization by cavity detuning are explained in [18]. Even though change of position of M4 here in a bow-tie cavity causes a small change in cavity alignment, the change is negligible for the required micron-scale adjustments around synchronisation. The pump laser propagated along the x-axis of the crystal with pump polarization parallel to z-axis of the crystal to access the highest nonlinear coefficients [19].

Figure 3 is a pictorial representation of all the possible wavelengths that can be generated in our system, showing clockwise (yellow) and counterclockwise (red) fields, and forwards (solid arrows) and backwards (dashed arrows) scattering processes. The cavity was able to resonate wavelengths between 1110 nm and 1180 nm, as determined by the Q of the cavity. It could also support cavity fields propagating in either direction around the ring, and so we must consider both near-0° forward scattering and near-180° backwards scattering. Starting with the 1064 nm pump light, the THz (polariton) and 248 cm^{-1} shifts associated with forward- and backward-scattering on the 248 cm^{-1} mode are not large enough to reach a supported wavelength. However, both the forwards-497 cm^{-1} and backwards-628 cm^{-1} shifts associated with the 628 cm^{-1} mode generate wavelengths supported by the cavity.

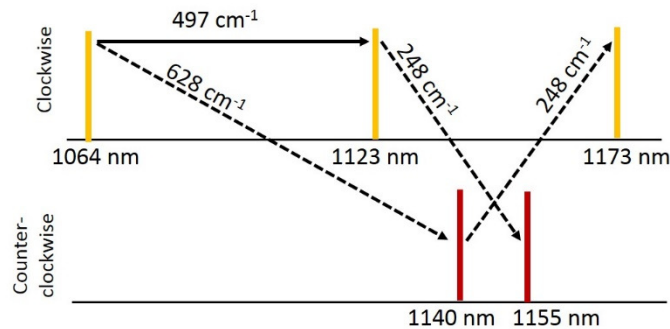


Fig. 3. Predicted Stokes and second Stokes in our system. Yellow lines represent clockwise fields, and red lines represent counter clockwise field. Solid arrow are forward scattering, and dashed lines are backward scattering.

The 1123 nm Stokes field generated by the forwards-497 cm⁻¹ shift propagates clockwise in the ring cavity while the 1140 nm Stokes field generated by the backwards-628 cm⁻¹ shift propagates counter-clockwise in the ring cavity. (These directions refer to the sense of rotation in the section of the bow-tie cavity containing the crystal.) These 1123 nm and 1140 nm intracavity fields can become sufficiently intense to themselves cascade to produce new wavelengths. The output coupler M4 begins to increase in transmission for wavelengths greater than 1180 nm, and so further cascading is only supported on the near-forwards-THz shift or the backwards-248 cm⁻¹ shift. The THz shift couples power into closely-spaced Stokes wavelengths co-propagating with the generating field, and we will discuss this effect later. The backwards-248 cm⁻¹ shift couples power from a field in one direction to a field in the counter-propagating direction. Here the clockwise 1123 nm field cascades to a counterclockwise 1155 nm field, and the counterclockwise 1140 nm field cascades to a clockwise 1174 nm field.

We studied the total output power of the laser system, as well as measuring the power and spectrum of both clockwise and counter-clockwise fields. Figure 4 (left) shows the output power in the clockwise direction (yellow) and counter-clockwise direction (red) at different pump powers along with the total power output (black). The system lased first at 1123 nm for pump powers over 1.5 W; for pump powers over 2.5 W, this field cascaded to generate 1155 nm. For pump powers greater than 3 W, we observed the 1140 nm field along with cascading to 1174 nm.

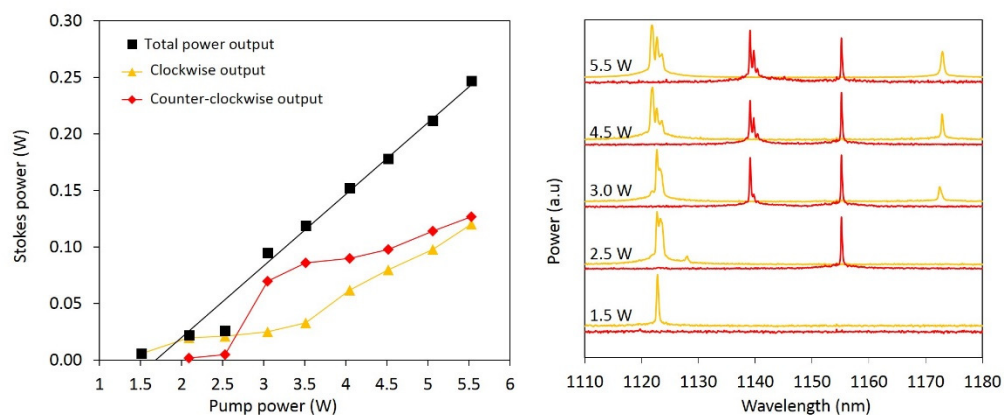


Fig. 4. Left: Power transfer measurement for the free-running laser. Right: Spectra of clockwise (yellow) and counter-clockwise (red) laser output at different pump powers, shown offset on an arbitrary scale.

At maximum pump power of 5.5 W, we thus observed the 1123 nm and 1174 nm clockwise fields and 1140 nm and 1155 nm counter-clockwise fields. The measured powers for the forwards and backwards propagating beams did not increase linearly with pump power due to competition effects, but the total output power was approximately linear with a slope efficiency of 6.3%.

3. Laser control

To selectively control the wavelengths oscillating in the laser, we introduced a 2-mm-thick magnesium fluoride birefringent filter (BF) into the cavity, as shown in Fig. 2. With the filter oriented at Brewster angle, we could vary the spectral transmission by rotating the angle of the optic axis within that Brewster plane [20], in order to favour a particular wavelength. Such a rotation varies both the location of the transmission peaks as well as the free spectral range. For this filter, the free spectral range varied from 68 nm to 49 nm in this wavelength region as the angle of the optic axis with respect to the laser polarization was varied between 25° and 72° .

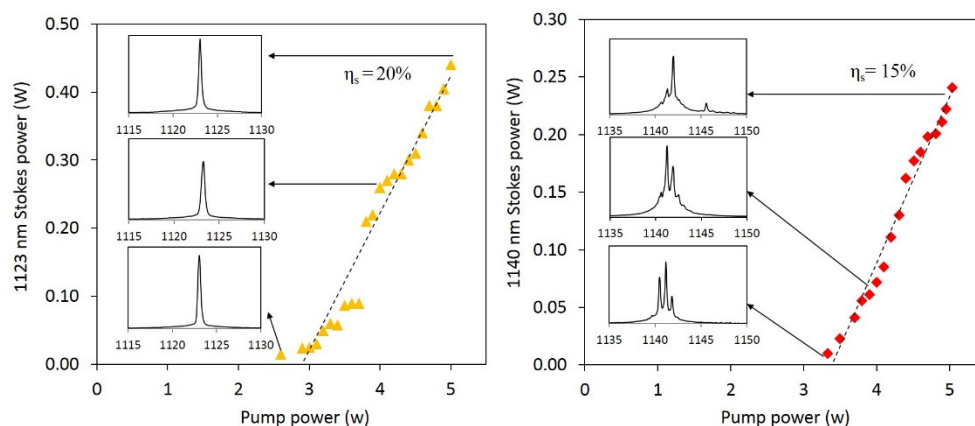


Fig. 5. Power transfer measurements for the spectrally-controlled laser, with spectra at threshold, 4 W and maximum pump power. Left: 1123 nm operation, Right: 1140 nm operation.

We found that setting the birefringent filter to a rotation angle of 25° , gave pure clockwise output at 1123 nm with a threshold of 2.6 W and a slope efficiency of 20%, as shown in Fig. 5. The pulse duration of the pure clockwise output was measured with an autocorrelator to be approximately 22 ps at the maximum output power. Despite the additional losses induced by the birefringent filter, the maximum output power was substantially higher than the total power for uncontrolled multispectral output, indicating the increased depletion of the pump pulses that could be achieved by constraining the cavity power to a single Stokes wavelength.

With the birefringent filter set at an angle of 42.5° , we achieved pure counter-clockwise output at 1140 nm with a threshold of 3.3 W and a slope efficiency of 15% as shown in Fig. 5. The pulse duration measurement for counter-clockwise output was approximately 50 ps.

For the pure-1123 nm and pure-1140 nm cases, not only was the competing shift for 1064 nm suppressed, but also the cascading of the intracavity field on the 250 cm^{-1} shift was suppressed. With alternative orientations of the birefringent filter we could allow that cascading. A 72° rotation of birefringent filter generated 1123 nm and 1155 nm fields only; a 65° rotation generated 1140 nm and 1174 nm fields only. Thus by introduction of the birefringent filter in the cavity, we can selectably generate any of the four key wavelengths in the system.

We note that in Fig. 4, there is evidence of a number of small shifts occurring on the 1123 nm and 1140 nm spectral lines, and this is also seen in the 1140 nm spectrum in Fig. 5. We attribute these shifts to stimulated polariton scattering at near- 0° on the 248 cm^{-1} shift, corresponding to few-nm shifts. The corresponding idler wavelengths are in the THz range (e.g. 0.2 THz for a 1 nm shift) presenting us with an excellent opportunity for

terahertz wave generation. The Stokes fields in this case must be generated at a slight angle since the SPS-gain and wavelength shift go to zero for 0° scattering. We did indeed observe that the small-shifted fields generated were slightly skewed in the cavity; these misaligned cavity fields are evidently still supported by the bow tie cavity that was operated relatively near its 'confocal' stability limit. The absence of THz shifts for pure-1123 nm operation we ascribe to the exact location of the filter transmission maxima in this configuration. This method of THz cascading the cavity-enhanced Stokes fields could be a simple and effective way to generate THz output from picosecond lasers with nanojoule scale energies, avoiding the need for resonant enhancement cavities [3].

4. Conclusion

In summary we have presented a multiwavelength ultrafast Raman laser based on lithium niobate. We demonstrated controllable generation of four different output wavelength using forward and backwards SRS as well as SPS. We highlight the possibility of terahertz generation, by using the LiNbO_3 to first couple power into a cavity-enhanced Stokes field, and then generating THz output by SPS.

Acknowledgments

This work was funded by Australian Research Council Linkage Project LP140100724 in association with M Squared Lasers Ltd. Aravindan M. Warriar is supported by a Macquarie University iMQRES scholarship

List of Figures

Figure #	Figure name	Page
1.1	Review of data of optically pumped semiconductor lasers.	04
1.2	Stokes and anti-Stokes generation.	06
1.3	Spontaneous and Stimulated Raman scattering.	07
1.4	Cascaded SRS process.	08
1.5	Versatility of Raman lasers with multiple frequency generation.	09
1.6	Transparency range of some of the typical Raman crystals.	15
1.7	General Raman laser cavity designs.	17
1.8	Laser characteristics of KGW Raman.	21
2.1	Diamond crystalline structure.	31
2.2	Transparency of diamond along with other known crystals.	32
2.3	Gain of different Raman materials	33
2.4	Optical schematic of synchronously pumped diamond Raman laser.	35
2.5	Power transfer measurements of 1240 nm laser.	37
2.6	Diamond laser characteristics with cavity detuning.	38
2.7	Stokes beam characterization using beamscope.	39
2.8	Comparison of laser characterization between two diamonds.	40
2.9	Modelled pulse shaped for longer cavities.	41
2.10	Modelled pulse shapes for shorter cavities.	44
2.11	Optical schematic of laser for cascading.	46
2.12	Laser characterization of second- Stokes laser.	48
2.13	Power transfer characteristics of cascading laser.	50
2.14	Four wave mixing happening in the laser.	51

2.15	Dispersion of different Raman crystals.	54
2.16	Backward Stokes and pump pulse collisions.	58
2.17	Pulse compression in backward Stokes pulses.	59
2.18	Components of an optical isolator.	60
2.19	Schematic of laser with optical isolator.	61
2.20	Orientations of HWP.	62
2.21	Polarization manipulation in optical isolator.	63
2.22	Characterizations (power and pulse width) of unidirectional lasers.	64
2.23	Cavity length detuning characterizations of unidirectional lasers.	65
2.24	Comparison of laser performances with and without using isolator	66
2.25	Efficiency of pure backward laser.	67
3.1	Transparency of lithium niobate crystal.	74
3.2	Structure of lithium niobate crystal with polar bonds.	74
3.3	A typical lithium niobate Raman spectrum.	75
3.4	Backward Raman spectra of lithium niobate.	76
3.5	Dispersion curve of polar materials.	78
3.6	Dispersion curve of lithium niobate.	79
3.7	Artistic representation of possible Stokes generation.	81
3.8	Optical schematic of the lithium niobate Raman laser.	82
3.9	Transmittance curves of cavity mirrors.	83
3.10	Predicted Stokes and second Stokes in our system.	84
3.11	Power transfer measurements.	85
3.12	Spectra of lithium niobate Raman laser.	86

3.13	Spectrum of lithium niobate Raman laser with different orientation.	88
3.14	Orientations of birefringent filter to alter the FSR.	89
3.15	Transmittance variation of birefringent filter.	92
3.16	Transmission spectra of birefringent filters used in experiment.	93
3.17	Power transfer measurements for the spectrally controlled laser.	94
3.18	Spectra of spectrally controlled laser.	95
3.19	Controlled cascaded Stokes generation.	96
3.20	Transmission curves of birefringent filter for controlled cascading.	97
4.1	THz radiation in the electromagnetic spectrum.	103
4.2	THz emission power as a function of frequencies.	104
4.3	Modified dispersion curve of Raman and IR active materials.	107
4.4	Pump, signal and idler generation diagram.	108
4.5	Gain coefficient of terahertz generation in lithium niobate on cooling.	110
4.6	A typical terahertz parametric oscillator configuration.	111
4.7	Schematic of an intracavity terahertz parametric oscillator.	112
4.8	Injection seeded terahertz parametric generator.	113
4.9	Spectral narrowing in an injection seeded TPGs.	113
4.10	Terahertz generation by optical rectification.	114
4.11	Collinear terahertz generation in quasi-phase-matched crystals.	116
4.12	Resonant enhancement cavity design.	117
4.13	Resonant enhancement oscillators with different output coupling.	118
4.14	Spectrum showing multiple peaks in Stokes spectrum.	120
4.15	Conventional terahertz generation setups and our present system.	120
4.16	Confocal geometry with the perfect mode and skewed modes.	121
4.17	Vertical scanning of the first and second Stokes generated.	122

4.18	Crystal orientation and silicon prisms.	123
4.19	Experimental setup for terahertz generation.	124
4.20	Angled second Stokes generation with terahertz generation.	124
4.21	Pictures of experimental setup.	125
4.22	Power transfer measurement of the terahertz waves generated.	126
4.23	Pure clockwise spectrum at different pump powers in Watts.	127
4.24	Pure clockwise Stokes spectra at maximum pump power.	128
4.25	Variance of transmittance of an etalon.	130
4.26	Transmittance curve of etalon superimposed over the Stokes spectra.	131